Haoming Wu

Improving freeze-thaw resistance of alkali-activated slag by admixtures

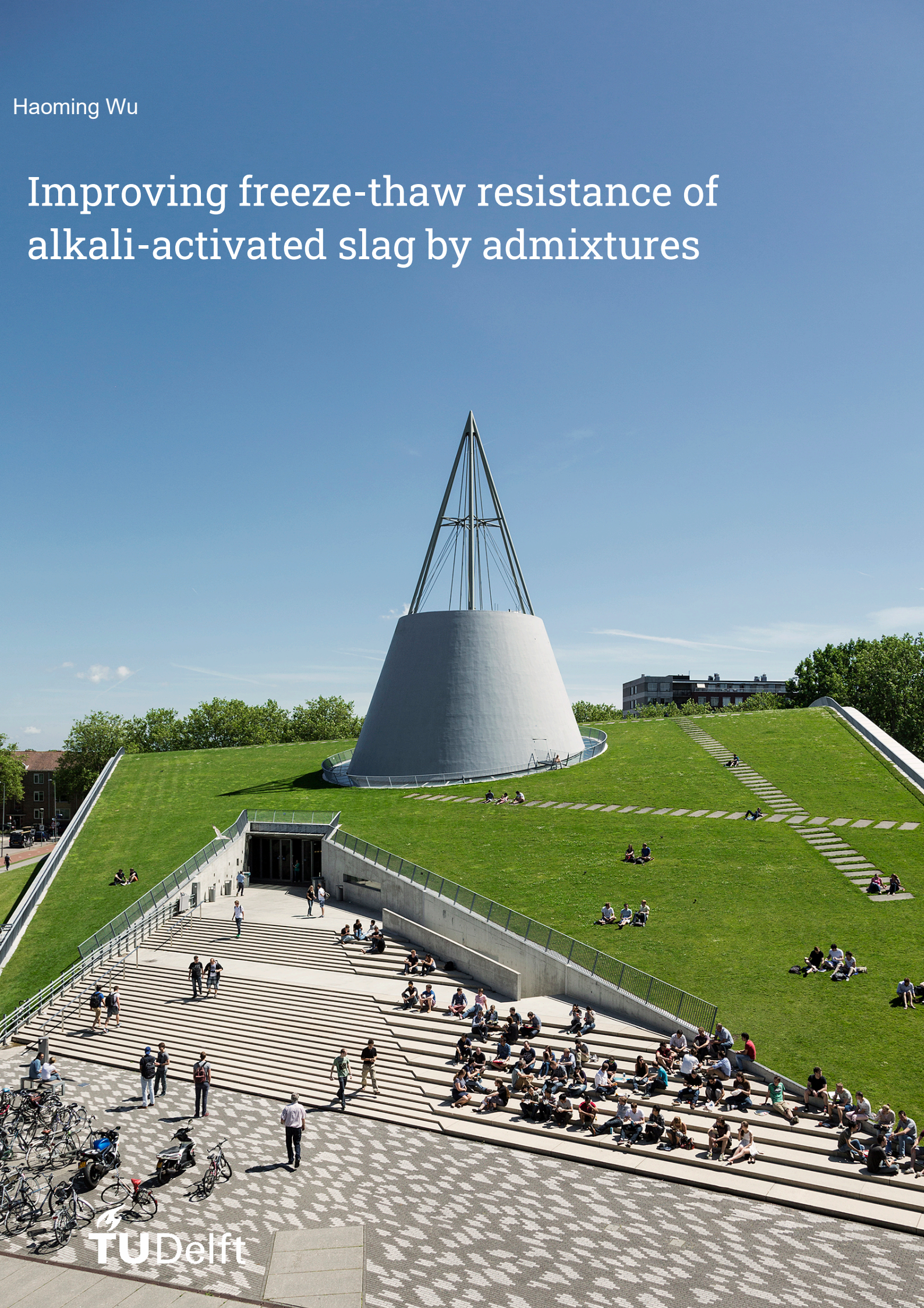

TU Delft

Improving freeze-thaw resistance of alkali-activated slag by admixtures

By

Haoming Wu

in partial fulfillment of the requirements for the degree of

Master of science

in Civil Engineering and Geoscience

at the Delft University of Technology,

Committee chair:	Dr. Guang Ye	TU Delft
Committee member:	Dr. Hua Dong	TU Delft
	Dr. Zhenming Li	TU Delft
	Dr. Sandra Barbosa Nunes	TU Delft

Contents

Contents

Preface

This thesis was completed as part of my Master's degree in Civil Engineering at TU Delft. Working on such interesting and meaningful research was a great opportunity and an enjoyable experience.

I would like to use this opportunity to express my gratitude to my committee members, Dr. Guang Ye, Dr. Hua Dong, Dr. Zhenming Li, and Dr. Sandra Barbosa Nunes, for their guidance, feedback, advice, and support throughout the study. Their mentorship has not only enabled me to finalize the thesis successfully, but also taught me valuable skills in logical, critical, and creative thinking, and showed me the qualities of a successful researcher.

I would also like to give sincere gratitude to all the researchers working together in the micro lab. Working with such a friendly and inspiring team has been a great and joyful experience. Thank you for your help, support, and inspiration during this journey. Special thanks go to Mr. Patrick Holthuizen, who helped me obtain beautiful and valuable microscopy images. In addition, massive appreciation goes to all the lab technicians for their technical assistance.

Lastly, I cannot express enough gratitude to my family and friends for their continuous support during my life. I could not have achieved this without them.

Haoming Wu

Delft, Feb 2023

Summary

Alkali-activated material (AAM) is one of the most attractive alternatives to ordinary Portland cement (OPC) due to its low-carbon emission characteristic. With the increasing understanding of AAMs' chemical reactions, mechanical properties, and microstructure, more and more research interests are now devoted to durability performance. In cold areas, including the Netherlands, freeze-thaw resistance is a crucial durability factor for concrete. However, the understanding of the freeze-thaw resistance of AAMs is minimal. Therefore, the freeze-thaw resistance of AAMs and possible solutions urge to be investigated on AAMs. Otherwise, the application of AAMs in cold areas might be obstructed.

Accordingly, the subject of this thesis is drawn forth. The main aim of this study was to investigate the effects and mechanisms of using admixtures (SAP and AEA) to improve the freeze-thaw resistance of alkali-activated slag (AAS). The research can be divided into two aspects: one is the influence of SAP and AEA on the macro-level properties such as workability, mechanical properties, and freeze-thaw resistance. And the other is the effect on the micro-level properties such as the air-void system, surface porosity, and surface microcracking. The former part aims to provide valuable information for the industrial application of AAS, while the latter part aims to provide valuable information for future research and explains the mechanisms behind the observation in the former part.

A literature review (chapter 2) was first conducted on the mechanisms, influencing factors, and solutions of freeze-thaw damage, as well as the performance of AAS. It was found that though this topic has been relatively thoroughly studied in OPC, the related study in AAS is minimal. Limited existing studies indicated that AAMs are sometimes more vulnerable to freeze-thaw cycles than OPC concrete, especially in the form of surface scaling damage.

Then, chapter 3 mainly investigated the effect of SAP and AEA on alkali-activated slag mortar's (AASM) workability and mechanical properties. Depending on the mix design, adding SAP and AEA could have a minimal influence on the workability of AASM. Regarding the compressive strength, adding AEA led to a similar reduction to that observed in OPC, while the strength loss caused by adding SAP is much smaller due to internal curing. In general, the influence of adding SAP and AEA on the workability and mechanical properties was acceptable.

Afterwards, the air-void systems created by SAP and AEA were reconstructed and characterized in chapter 4 by the micro-CT scan. It was found that both SAP and AEA successfully entrained air voids into AASM, while the characteristics of the resultant air-void system were quite different. The air-void system parameters were then characterized from the perspective of air content, air voids spacing, and air voids size distribution.

In chapter 5, optical microscopy was used to evaluate the surface condition of AASM undergoing 28-day sealed curing or preconditioning procedures in the CDF test and the ASTM C672 test. It was found that AASM exhibited a high surface microcracking potential. Samples sealed for 28 days showed a considerable extent of microcracking due to autogenous shrinkage. Samples that underwent 14-day drying after 7/14 days' curing showed significant microcracking due to autogenous shrinkage and drying shrinkage. With the addition of SAP, the cracking caused by autogenous shrinkage was minimized, but the cracking caused by drying was only slightly reduced. With the addition of AEA, there was only a minor improvement in surface integrity.

The freeze-thaw resistance of AASM with or without the addition of SAP or AEA was investigated in the form of surface scaling damage by a modified CDF test in chapter 6. Plain AASM showed poor surface scaling resistance mainly attributed to the pre-existing surface microcracking. The addition of SAP and AEA successfully improved the surface scaling resistance of AASM. The improvement was

more significant by adding SAP due to the effect of improving surface integrity. Based on the SAP mixtures, a good correlation was found between the SAP air-void system and the resultant surface scaling resistance. The final cumulative surface scaling generally decreased with higher entrained air content, denser air voids distribution, and smaller air voids size. A preliminary logarithm model was developed for the relationship between the reduction in surface scaling and the equivalent water/binder ratio and the air-void system. Finally, upscaling tests on the concrete scale also found that the addition of SAP improved the surface scaling resistance of AASC.

Overall, in this study, the freeze-thaw resistance of AASM was successfully improved by the SAP and AEA. The effects of adding SAP/AEA and the related factors on the selected properties of AASM were revealed. The mechanisms behind these observations were also understood and generated a series of further research possibilities. It is hoped that these findings and observations can give some guidance to the industrial applications of AAS and some inspiration to the scientific community.

1 Introduction

1.1 Background

Concrete is one of the most widely used construction materials worldwide because of its low price, sound performance, and readily accessibility of raw materials. Concrete is an artificial composite material consisting of binder matrix and aggregates. Since the nineteenth century, ordinary Portland cement (OPC) has been widely used as a raw material to produce the binder matrix in concrete. Meanwhile, with the development of research on cementitious materials, alternatives to OPC continuously emerged for various purposes, such as waste utilization, secondary pozzolanic reaction, etc. Among these alternatives, alkali-activated material (AAM) is one of the most attractive alternatives. Similar to OPC binder, which is created by the reaction between solid (OPC) and liquid (water), AAM is a binder system derived by the reaction of solid aluminosilicate powers (referred to as precursor) and liquid alkali metal sources (referred to as activator) [1, 2]. The construction process with AAMs is also almost identical to the OPC, and AAMs showed comparable or better performance than OPC at many properties.

With the increasing attention on environmental impact and sustainability, AAMs are getting more and more interest because of the low-carbon emission characteristic. By the Paris agreement, all 197 UNFCCC members have a joint global commitment to deliver net zero carbon emissions in the second half of the century. Afterwards, the European climate law stated the target to achieve carbon neutrality by 2050. From the perspective of concrete construction, OPC is an industrial product and its production accounts for 5 - 8% of the total global carbon dioxide emission due to intensive energy consumption and CO_2 emission [3-5]. In contrast, many raw materials used in AAMs are industrial by-products or waste, such as blast-furnace slag, fly ash, municipal solid waste incineration ash, etc. Depending on the precursor selection, the CO_2 emission during the production of raw materials can be reduced by up to 90% by substituting the OPC with AAMs. When the blast-furnace slag is used as the precursor to produce AAM concrete, the reduction in carbon emission is about 70-80% [6]. Therefore, AAM technology shows good potential in delivering low-carbon emission concrete.

Thus, AAMs are attracting more and more research interests. In the last few decades, considerable research has been done on its chemical reaction, mechanical properties, and microstructure. In terms of concrete construction, three aspects are crucial: mechanical properties, workability, and durability. It is found that AAMs have good mechanical properties compared to ordinary Portland concrete, which is a great advantage when considering the structural design. Regarding workability, AAMs is generally more sticky than OPC binder, but it is generally acceptable. On the other hand, with the increasing awareness of the structure life cycle, the durability of the construction materials is also extremely important. In this perspective, the understanding of the long-term behavior and durability of AAMs is not as mature as OPC, which might obstruct the application of AAMs.

In cold areas, freeze-thaw resistance is a crucial durability factor for concrete. Due to their porous characteristic, cementitious materials can absorb and retain moisture and are generally vulnerable to freeze-thaw cycles [7, 8]. The freeze-thaw attack has been studied for many decades on porous materials. However, there are still debates on the mechanisms behind the freeze-thaw damage. A recapitulation can be formulated as during the temperature change, the phase transformation of the pore liquid to ice exerts force(s) on the matrix. Damage occurs when the force(s) exceeds the matrix tensile capacity. In terms of OPC concrete, this issue has been systematically studied for many decades, and solutions have been well delivered [9]. On the other hand, the freeze-thaw behavior of the AAMs has not been thoroughly studied [10, 11]. The freeze-thaw behavior is generally

physically dependent instead of cement chemistry dependent, and the previous theories and solutions on OPC concrete might be used as references or guidelines. However, in the AAMs system, it was reported that some helpful conventional solutions, such as air-entraining, are less effective or no longer work [11]. And the limited existing studies [12, 13] showed that alkali-activated materials are sometimes more vulnerable to freeze-thaw cycles than OPC concrete, especially in the form of surface scaling damage. Therefore, the freeze-thaw behavior and solution still urge to be investigated in the AAMs system. Otherwise, the application of AAMs in cold areas might be obstructed. Therefore, the subject of this thesis is drawn forth. If solutions for improving the AAMs surface scaling performance can be proposed, investigated, and verified, it might clear the obstacle of AAMs application in cold areas.

To improve the freeze-thaw performance of cementitious materials, a well-known solution is to entrain empty air voids in the binder matrix by admixtures to release or limit the generated pressure during the freeze-thaw cycles. This starting point will be applied, examined, and investigated for this study.

1.2 Research objectives and questions

This MSc project aims to provide a solution for the industry to improve the freeze-thaw resistance of AAS with admixtures (SAP and AEA), fill the related knowledge gap, and reveal the potential scientific research in the future.

Accordingly, the MSc thesis's objective is to investigate the effect and mechanism of using admixtures (SAP and AEA) to improve the freeze-thaw resistance of alkali-activated slag (AAS) by experimental study. Meanwhile, a minor research objective is also defined as investigating the causes of AAS's poor surface scaling performance.

The research objective is broken down into the following research questions and sub-questions:

- What are the effects of adding SAP/AEA?
  - How does the SAP/AEA influence workability?
  - How does the SAP/AEA influence the mechanical properties?
  - How does the SAP/AEA influence the freeze-thaw resistance of AAS?
  - What is the influence of relative factors on these properties when adding SAP/AEA?
- What are the underlying mechanisms?
  - What is the difference in the water/binder ratio?
  - What is the difference in the air-void system after adding SAP/AEA?
  - What is the difference in the surface microstructure after adding SAP/AEA?
  - How do the air-void system and surface microstructure correlate to the observed effect of adding SAP/AEA?
- Among the observations, is there any characteristic in AAS that might lead to poor surface scaling resistance?

The ultimate goal of this study is not to develop a mix design of AAS that has a high freeze-thaw resistance. Instead, it focuses on providing strategies for improving the freeze-thaw resistance and directions for future research by understanding the underlying mechanisms.

1.3 Research scope

It is well known that there are many types of AAMs. Dozens of precursors and activators can be chosen and combined to produce very inherently different AAMs. Because it is impossible to cover all kinds of AAMs, and the focus of the study is on the solution, only one mixture will be used as the reference, and the factor study will be focused on the admixture application aspect. The type of precursor is chosen to be blast-furnace slag (referred to as slag), one of the most used raw materials in construction in the Netherlands; while the activator is chosen to be sodium silicate solution, which is the most commonly used choice.

In this study, two admixtures will be used to improve the frost resistance of AAMs. One is the air-entraining agent (AEA), and the other is the superabsorbent polymer (SAP). There are several types of AEA and SAP, and they might lead to different results. However, due to the time limits, the scope will be limited to only one of each.

Considering the limited time and workforce, major of the work will be conducted on the mortar scale, i.e., alkali-activated slag mortar (AASM). In addition to the freeze-thaw performance, AEA and SAP might also considerably affect many other properties, which are of great importance. For this reason, their effect on some selected general designing properties (e.g., mechanical properties, workability) and microstructure properties will also be investigated. Meanwhile, these investigations also provide information for understanding the mechanisms behind the improved freeze-thaw resistance. Afterwards, upscaling to alkali-activated slag concrete (AASC) will be conducted.

1.4 Lay-out of the thesis

The thesis consists of seven chapters. The main structure can be divided into three aspects: the literature review, the effect of SAP/AEA on the resultant properties, and the underlying mechanisms.

The first chapter is for a brief introduction and background information.

The second chapter is for the literature review. Some general information regarding freeze-thaw resistance will be discussed first. Then, the literature regarding the freeze-thaw resistance of AAS will be addressed. Later, the main existing mechanisms for explaining the freeze-thaw attack will be addressed, together with the factors that influence the freeze-thaw performance. Afterwards, the entraining air voids method for improving the freeze-thaw damage will be discussed in detail.

In the third chapter, the effect of SAP/AEA on some crucial general properties, such as strength development, will be studied. A factor study on the mix design parameters of AEA/SAP is conducted to investigate how SAP/AEA influences some fundamental properties.

Chapter four is reserved for characterizing the air-void system of the AASM with or without adding AEA/SAP. The resultant air-void system parameters, such as air content and air voids spacing, will be quantified. The influence of selected factors on the entrained air voids system will also be studied.

Chapter five is reserved for investigating the surface microstructure of AASM after preparation and preconditioning in accordance with the existing surface scaling test protocols.

In chapter six, the effect of SAP/AEA on the surface scaling resistance of AASM will be studied. The correlation between the freeze-thaw performance and the findings in previous chapters is bridged. Based on the findings in AASM, selected mix proportions will be used in AASC for verification.

Chapter seven is reserved for conclusions and suggestions for industrial application and future research.

2 Literature review

2.1 Background

Freeze-thaw resistance is a crucial durability factor for ensuring the service life of concrete in cold areas. Freeze-thaw damages occur on concrete elements when they undergo temperature cycles above and below 0℃. The freeze-thaw damage can manifest in several forms, while the most common damage forms are internal cracking and surface scaling [8, 11, 14]. Concrete deterioration under the freeze-thaw cycles has been studied since the 1940s, but internal cracking and surface scaling were not clearly distinguished until decades later [14].

Internal cracking is the damage form that mainly accounts for the deterioration of concrete mechanical properties. During the freeze-thaw cycles, the initiation and development of internal cracks in the concrete body cause reduction in concrete mechanical properties. As a result, the degradation of structural performance might lead to exceeded structural deformation and questionable structural safety. The internal damage is often evaluated by the variation of strength or stiffness during the freeze-thaw cycles. A typical result is shown in Figure 2.1.1. Standards and test protocols for determining the internal cracking resistance to freeze-thaw cycles are CEN/TR 15177 [15], ASTM C666, CIF test [16], etc.

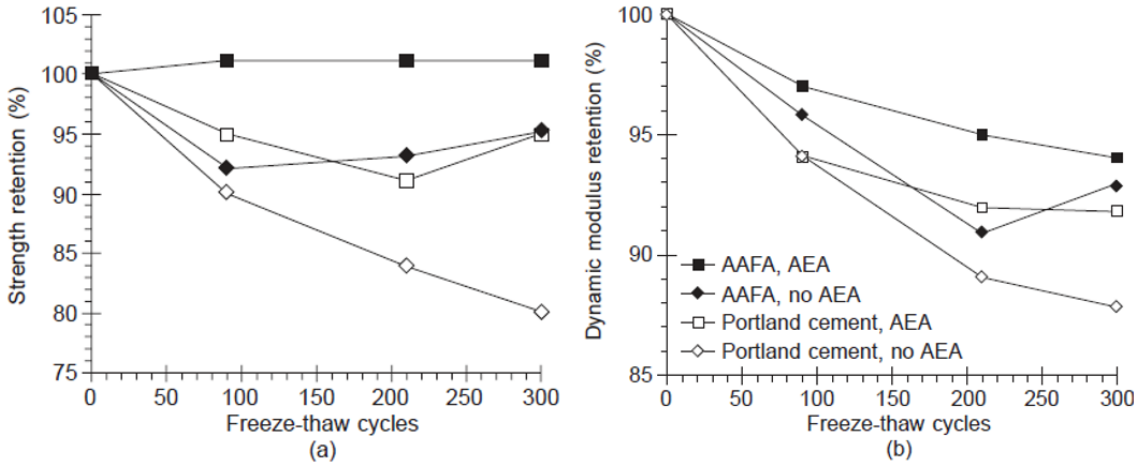

Figure 2.1.1 (a) Compressive strength retention (%) and (b) dynamic modulus retention (%) over freeze-thaw cycles of mixtures based on OPC and alkali-activated fly ash (AAFA), with and without AEA [11]. Data from [17, 18].

Surface scaling is the damage form that addresses the surface condition of concrete. During the freeze-thaw cycles, the materials of the concrete surface layer become loosened and scale off in the form of flakes or chips. The deterioration gradually advances from the surface of the concrete and exposes coarse aggregates. The surface scaling damage during freeze-thaw cycles is usually combined with the use of deicing salts. A typical surface scaling damaged concrete surface is shown in Figure 2.1.2. The surface scaling not only reduces the aesthetic value of the construction but also triggers other durability issues, such as lower abrasion resistance and reinforcement corrosion. The surface scaling is often evaluated by the mass loss of the concrete test surface over freeze-thaw cycles. Experiment protocols for determining the surface scaling resistance under freeze-thaw cycles are described in ASTM C672, CEN/TS 12390-9 [19], the CDF test [20], etc.

Figure 2.1.2 Surface condition evolution of an AASC with severe surface scaling damage due to freeze-thaw cycles.

2.2 Freeze-thaw resistance of AAS

Literature investigating the freeze-thaw performance of AAS is limited. Many studies did not specifically focus on freeze-thaw performance; as a result, the information, discussion, and understandinng on this topic are not extensive, systematic, and thorough. Most of the available information is regarding the internal cracking resistance of AAS, while information about the surface scaling resistance is scarce. Based on the limited information, it seems that: compared to OPC, AAS likely has an equal or better resistance on internal cracking resistance but a poorer surface scaling resistance.

2.2.1 Internal cracking resistance

The internal cracking resistance is closely connected to the characteristic of the capillary pore system of the binder. The OPC and AAS have quite similar microstructure, while two significant differences exist and probably result in different freezing behavior of the pore water.

First is the difference in pore size distribution. The freezing point of the pore water is considerably depressed by the capillary action. From a thermodynamic point of view, the relation between the required overcooling for freezing and the pore radius can be expressed by [21]:

$$\frac{T_0 - T}{T_0} = \frac{2\nu_f \sigma_f}{rq}$$

where:

T_0 = normal freezing point,

T = freezing point in capillary pore system,

ν_f = molar volume of the fluid,

σ_f = the surface tension,

r = radius of curvature of fluid surface,

q = latent heat of fusion of fluid.

The relationship is schematically shown in Figure 2.2.1. Compared to the OPC binder, AAS has a finer pore structure, with more gel pores and fewer capillary pores. Due to the smaller pore radius, the pore water in the capillaries of AAS has a lower freezing point, and the gel water might never freeze in the standard test and reality [2].

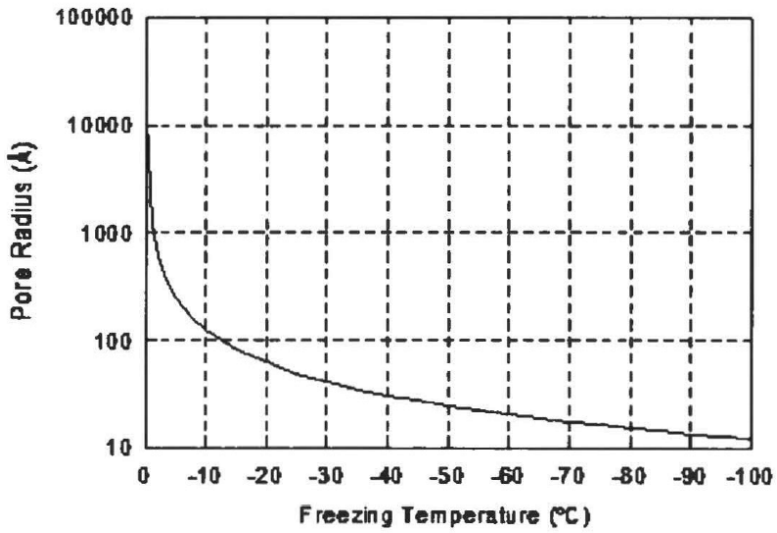

Figure 2.2.1 Relationship between the pore radius and freezing temperature, adapted from [2].

On the other hand, the pore water's freezing point is also considerably influenced by the ionic strength in the pore solution. In this perspective, AAS has a higher pore solution ions concentration than OPC [10, 22, 23]. This higher ionic strength could also lead to a lower freezing point of the pore water in the AAS capillaries. Therefore, from the perspective of freezing of the pore water, the AAS seems more resilient than the OPC binder.

Douglas et al. [24] investigate five air-entraining AAS concretes with different alkali contents. The modulus of silicate and water/binder ratio was set to be 1.22 and 0.48, respectively. The test was conducted according to ASTM C666, which focuses on the internal cracking resistance. All the mixtures showed only a minor loss of relative dynamic elastic modulus after 500 cycles, except for mix 5, which had the lowest alkali content and highest air voids spacing. The flexural strength after 500 cycles was also tested. In contrast to the good performance in stiffness, a reduction of around 40% was observed in the flexural strength of mix 1-4, while 68% was for mix 5. This observation might be due to the higher sensitivity of flexural strength to micro-scale damage such as microcracking.

Gifford and Gillott [25] investigated and compared the freeze-thaw performance of an AAS concrete and a reference OPC concrete. The AASC had a modulus of silicate Ms = 1 and alkali content = 6.1%. The concretes had three air entrainment levels. An AEA solution of various surface-active agents was used. The water/binder ratio of OPC and AAS was identical to 0.44. The freeze-thaw test was conducted with ASTM C666. The results showed that the internal cracking resistance of AASC was as good as OPC concrete, given the proper air-void parameters. However, it is noticed that the 28-day compressive strength of the medium air content mixture is not very comparable: 29.4 MPa for OPC concrete and 36.6 MPa for AAS concrete.

Fu et al. [26] investigated the internal cracking resistance of five high-strength (~ 90 MPa) AAS concrete. The rapid freeze-thaw test was conducted in accordance with ASTM C666 and GB/T 50082-2009. All the mixtures showed excellent internal cracking resistance with F300 frost-resisting grade. The relative dynamic elastic modulus of the mixtures was around 90% after 300 freeze-thaw cycles, and the surface materials loss was minor. The good resistance was attributed to the dense microstructure and high strength. The same research group [27] further investigated the internal cracking resistance of AAS concrete that has a similar mix proportion with the response surface methodology. The authors did not mention whether the mixtures were air entrained or not. Again, all 17 mixtures showed good internal cracking resistance with F300 resistance grade.

Matalkah and Soroushian [12] conducted the ASTM C666 test on an alkali aluminosilicate concrete (AAC) and an OPC concrete reference. Both mixtures were non-air-entrained. The precursor of the AAC is a trinary system consisting of coal fly ash, slag, and albite, and the activator is prepared by sodium hydroxide, sodium silicate, and calcium oxide. ASTM C1585 sorptivity test showed that the AAC has a much lower permeability than the OPC reference. With the ASTM C666 test, AAC showed better internal damage resistance by a lower loss in dynamic elastic modulus, resonant frequency, and mass.

Accordingly, the literature generally gives the impression that AAS have equal or better internal cracking resistance during freeze-thaw cycles than OPC. And this was commonly attributed to the lower permeability, finer pore structure, and higher ions concentration in the pore solution. However, the available information is still limiting and unsystematic. Comprehensive studies still needs to be conducted to see the internal cracking resistance of AAS without air-entraining.

2.2.2 Surface scaling resistance

The literature explicitly dedicated to the surface scaling of AAS is scarce [11]. Some studies [24-26] measured the mass evolution during the internal cracking resistance test (e.g., ASTM C666, etc.) and found the mass loss is minor. However, the test liquid is without de-icing salts, which is a crucial factor in surface scaling behavior. Most of the literature agrees that the scaling behavior between subjecting to 3% brine solution and subjecting to pure water significantly differs [8, 12, 13, 28]. The test results with pure water do not represent the surface scaling resistance.

In addition to internal cracking resistance by ASTM C666, Matalkah and Soroushian [12] also conducted the ASTM C672 test to investigate the surface scaling resistance of AAC and reference OPC. As mentioned above, AAC showed better internal cracking resistance than OPC in the ASTM C666 test. However, in the ASTM C672 test, the AAC had much more sever surface scaling than the OPC. After eight freeze-thaw cycles, the cumulative scaling of AAC without air-entraining is above 1 kg/m^2, which is around ten times higher than the scaling of OPC concrete.

Aiken et al. [13] investigated the surface scaling resistance of an OPC concrete, and alkali-activated fly ash concretes with different content of slag substitution (0% - 70%). The test was conducted with a test procedure similar to EN12390-9. Two test solutions were used and compared: distilled water and 3% NaCl solution. It is noticed that the results were not normalized by the test area but by the total mass, which conflicted with the standard. Fortunately, as shown in Figure 2.2.2, the difference between the results is significant to point out two conclusions. One is that the scaling in the 3% NaCl solution environment is significantly more severe than that in distilled water. In addition, it can be observed that alkali-activated slag/fly ash showed lower surface scaling resistance than the OPC reference, and the performance could be improved by higher slag content in the precursor.

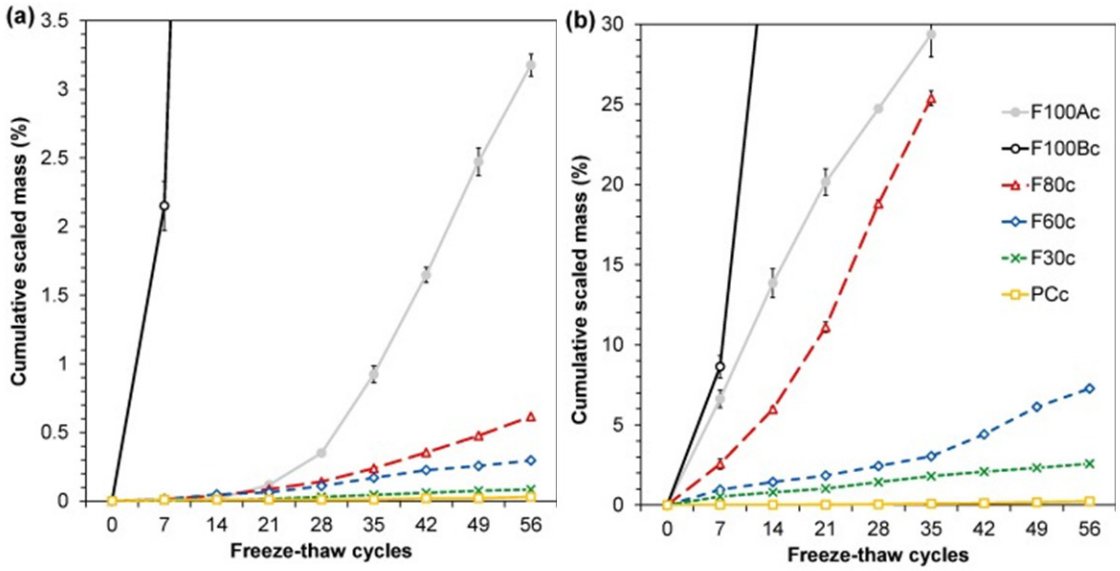

Figure 2.2.2 Cumulative scaled mass (%) of mixes during freeze-thaw cycles in the presence of a) water and b) 3% NaCl solution, where the number stands for the content of fly ash (%) in the precursor [13].

However, there are also reports stating that alkali-activated slag/fly ash concrete has a better surface scaling resistance than OPC. With 3% NaCl solution as the test medium, Setzer and Hartmann (cited by [10]) found the alkali-activated concrete (fly ash dominated) had a poorer surface resistance than OPC concrete reference. On the other hand, the alkali-activated concrete (slag dominated) showed a much better surface scaling, with 1.4 kg/m^2 scaling materials after 28 freeze-thaw cycles, much less than the OPC reference which gave 3.4 kg/m^2 scaling. A surface scaling test with water as the medium was also conducted, and the resultant scaling was considerably lower than that with de-icing salt. However, a thing that needs to be pointed out is that the alkali-activated concrete (slag-dominated) mixture had higher compressive strength than the OPC reference (~ 60 MPa vs. ~50 MPa).

As mentioned above, AAS's better internal cracking resistance was generally attributed to its finer pore structure and higher ion content in the pore solution. However, when it comes to surface scaling, the situation changes. The AAS is much more sensitive to environmental conditions [10]. Processes such as drying and carbonation can lead to higher porosity, larger pore radius, and microcracking on the surface layer of the AAS [29]. Such changes in surface microstructure are unquestionably changing the surface scaling resistance. From the perspective of ions strength, for the surface scaling, the salt concentration in the external liquid is more critical than the salt concentration in the pore solution [8, 30]. And therefore, AAS loses the advantage of higher ions concentration in pore solution. Consequently, it might be the case that the surface scaling resistance of AAS is not as good as OPC.

Overall, the literature regarding this aspect is scarce; therefore, it is difficult to conclude the general surface scaling performance of AAMs or AAS.

2.3 Mechanisms of freeze-thaw damage

To improve the freeze-thaw resistance of AAS, the mechanisms responsible for freeze-thaw damages must first be understood. In this perspective, the mechanisms responsible for the AASC are generally believed to be identical to those behind OPC concrete. To the author's knowledge, there is no new proposed hypothesis exclusively explaining freeze-thaw damage of AASC. Instead, all the literature investigating the freeze-thaw resistance of AAMs used theories that were previously developed in the

OPC. This is because the proposed mechanisms are mainly based on the physical phenomenon instead of chemical reaction. In this perspective, OPC concrete and AAMs concrete are very similar: porous composite materials containing water. Therefore, all theories discussed in this study were developed on OPC concrete. And it is assumed that AAMs concrete followed identical fundamental deterioration mechanisms.

The mechanisms behind the freeze-thaw damage of concrete have been investigated since this problem was identified. Several hypotheses have been proposed to explain the behavior of concrete and water during the freeze-thaw cycles. However, up to now, there are still no definite answers to this question. And the fundamental similarities and differences between the internal cracking and surface scaling remain to be clearly revealed. Nevertheless, it seems that the freeze-thaw deteriorations are not caused by a single driving force but by the coupling of several driving forces. And some mechanisms behind the internal cracking also contribute to surface scaling to an extent.

Accordingly, this section summarizes the main mechanisms behind internal cracking and surface scaling proposed in previous literature.

2.3.1 Mechanisms of internal cracking damage

As mentioned above, some mechanisms behind the internal cracking deterioration might also be responsible for the surface scaling damage. Therefore, some of the main proposed mechanisms for internal cracking are discussed first.

The starting point for explaining the freeze-thaw damage is generally the 9% volume expansion during the water freezing. A highly simplified model treats the concrete as a vessel with water. The water in the vessel expands when it freezes, and damage is generated if there is no enough room to accommodate this expansion. Therefore, the concept of critical degree of saturation was proposed, and theoretical value was preliminary calculated as 91.7%. Undoubtedly, this explanation is over simplified. And further study showed the critical degree of saturation is well below this value [31-36].

Hydraulic pressure theory was proposed by Powers to explain the freeze-thaw damage [37-39]. As shown in Figure 2.3.1, water freezing starts in the capillary pores with a high amount of water filled. During freezing, the ice causes volume expansion and pushes the unfrozen capillary water away though the concrete matrix. This circumstance is a classic case of Darcy's Law, which describes the flow of fluid through a porous medium. The generated hydraulic pressure in the concrete depends on the permeability, distance to flow, and flux. When the generated hydraulic pressure exceeds the matrix tensile capacity, cracking occurs. In this circumstance, the water flows from where ice is initially developed. Sun and Scherer [40] calculated the hydraulic pressure with the consideration of overcooling and ice volume fraction. It was found that the generated pressure from a rapid ice formation could be destructive if nucleation occurs well below the melting points, i.e., overcooling. However, some test results also suggested that the water movement might be in the opposite direction [41].

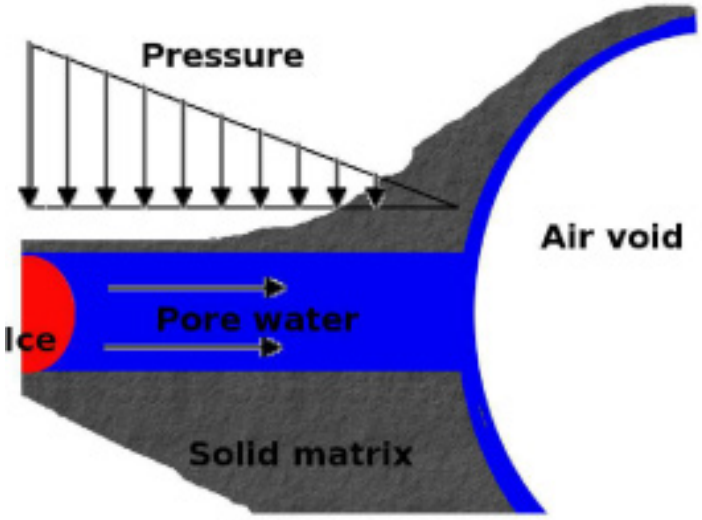

Figure 2.3.1 Schematic of hydraulic pressure theory proposed by Powers, adapted from [42].

Later, osmotic pressure was suggested to be one of the driving forces to evaluate the effect of solutes in the pore water and explain the direction of water movement [39]. Hydrolic pressure theory simplified the pore water as pure water. However, pore water in the concrete contains solutes. The water in the capillary pore freezes prior to the water in the gel pore, which cannot freeze at a temperature higher than -78°C due to the tiny pore size. Water freezing in the capillary pore results in an increased concentration in the pore solution. A concentration gradient is hereby created, driving the water flow from the gel pore to the capillary pore to equalize the concentration difference. As a result, the pressure is generated by osmosis. However, considering the relatively low concentration in the pore solution and the compensation from the fluid flow, later literature suggested that the pressure is not enough to damage the matrix [28, 41].

In addition to the hydraulic and osmotic pressure, Powers and Helmuth [43] further discussed the effect of water migration during the freeze-thaw cycles from thermodynamic perspective. The idea was connected to the macroscopic ice lenses phenomenon that had been discussed intensively in soil mechanics. Following this idea, Setzer formulated the micro-ice lens theory [43, 44]. The main idea is that, during cooling, water in the gel has a higher free energy than the ice in the capillaries. The higher free energy drives the water to flow from the gel to the capillaries. During heating, the micro ice lenses are still frozen, and the gel absorbs available external water and increases the total degree of saturation. During the cycles, the micro ice lenses trap moisture from the gel during cooling, hinder water flow back during heating, and keep growing up, which could pressure the capillary wall and ultimately cause damage. With this hypothesis, osmosis might also have a contribution. The author monitored the water uptake during the CDF test and found the freeze-thaw cycles led to a doubled additional saturation. It is stated that the results confirm the micro-lens theory. However, it seems that the author ignored the new-developed flaws at the test surface of the specimen during freeze-thaw cycles, which might also result in considerable additional water uptake.

Crystallization pressure was also proposed to be a driving force behind the freeze-thaw damage. Figure 2.3.2 shows a schematic of the crystallization theory. During freezing, the crystal attempts to grow in the direction of the pore wall because of the curvature difference between the crystal's side and the end [28]. When the contact angle between the crystal and the wall exceeds 90°, the pore wall is subjected to hoop tension to suppress the growth of the crystal in the radial direction. When the hoop pressure exceeds the local tensile stress with the continuous development of the crystal, the damage is induced.

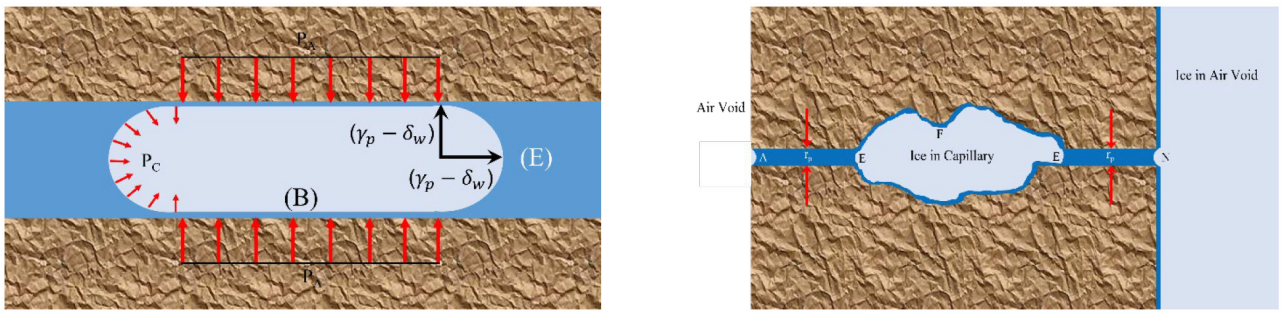

(a) (b)

Figure 2.3.2 Schematic of ice forming in (a) cylinder capillary pore; (b) capillary cavity and an air void [28]

Bijen [7] suggested that the damage might mainly occur at thawing instead of freezing. A schematic is presented in Figure 2.3.3. When the water in the large capillaries freezes, it attracts moisture from the surrounding and continuously grows, as suggested by the micro-lens theory. When the temperature rises, the ice will expand with a coefficient of thermal expansion (CTE) five times larger than concrete's CTE. And this difference in CTE subsequently exerts pressure on the concrete and causes damage.

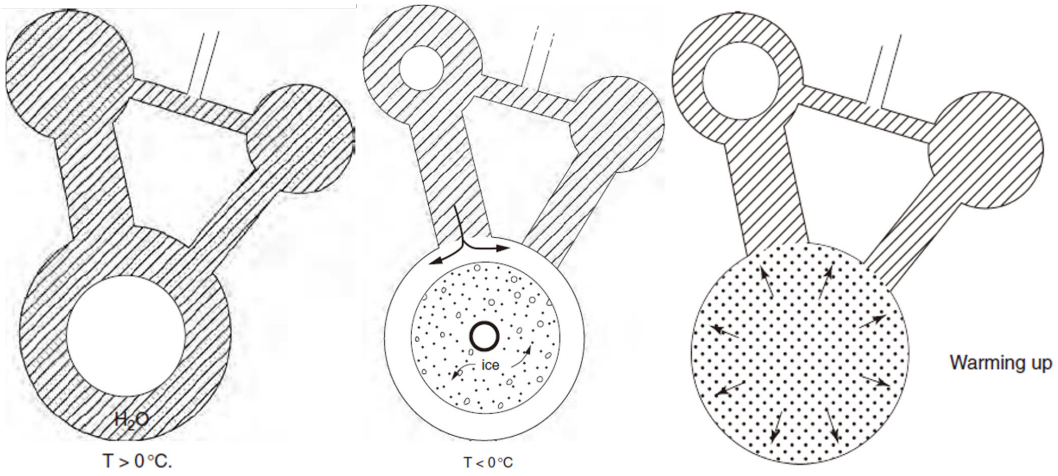

Figure 2.3.3 Schematic of Bijen's model for explaining the freeze-thaw damage process [7].

2.3.2 Mechanisms of surface scaling damage

The resistance to surface scaling is not strongly correlated with the resistance to internal cracking [8, 45]. Compared to internal cracking, surface scaling has two main differences. One is the involvement of de-icing salts, which aggravates the deterioration. And the other main difference is the deterioration position: the surface scaling happened at the surface of the concrete, which is the interface between brine, ice, and concrete, instead of the relatively homogenous bulk body. The role of these two differences has been widely discussed in the literature, and some additional mechanisms were proposed to explain the surface scaling damage.

The gradient of salt concentration along the thickness is suggested to be one of the driving forces behind surface scaling [7, 46]. A schematic of the damage process is shown in Figure 2.3.4 [7]. The migration of salt solute from the external brine to the inner bulk of concrete is not finished immediately. Therefore a salt concentration gradient is built up in the direction of thickness. With higher salt concentrations, the pore water in the concrete has a lower freezing temperature. Thus, the freezing temperature of pore water increase towards the surface. Besides, the temperature gradient during freezing also exists during the temperature change. The coupling of the salt concentration gradient and temperature gradient creates a situation that: two frozen layers sandwich one unfrozen

layer. As time goes on or the further decrease in external temperature, the unfrozen layer freezes. However, at this point, there is no space to accommodate the water movement during freezing; therefore, the damage is created.

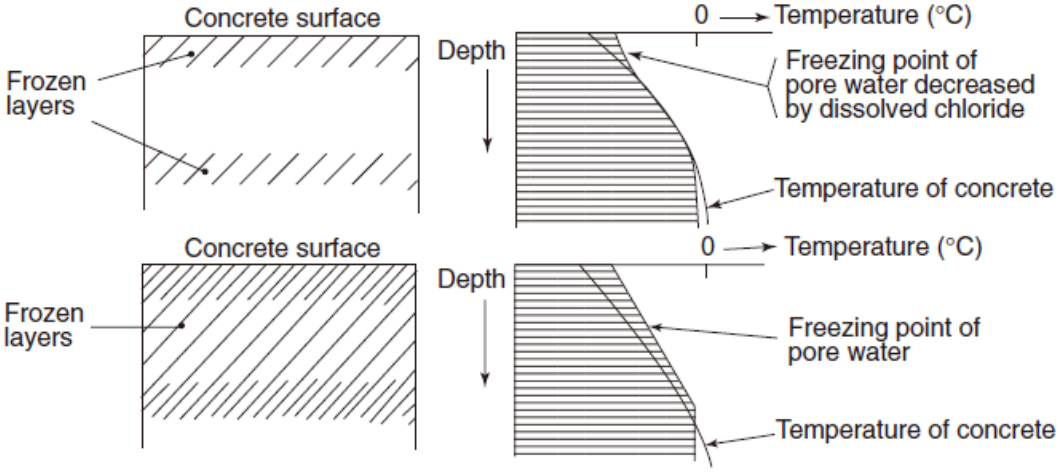

Figure 2.3.4 Frozen layer with intermediate unfrozen layer leading to blistering [7].

Thermal shock was also suggested as one of the driving forces behind surface scaling [47, 48]. When the dry de-icing salt is applied to the concrete surface, the ice and snow start to melt due to the lowered freezing temperature. The heat required during the melting is mainly taken from the concrete and causes a considerable temperature reduction in the several millimeter-thick surface layer. It was suggested that the resultant temperature gradient causes internal tensile stress at the surface layer and damages the concrete. However, thermal shock should not be regarded as the primary driving force behind surface scaling. This is because, in most freeze-thaw test protocols, the de-icing salts are applied in the form of solution instead of dry solids. Therefore, there is no such thermal shock during the freeze-thaw tests. In addtion, the hypothesis was based on calculation and lacked of supporting evidence from experiments or reality.

Another critical proposed theory for surface scaling is the glue-spall theory [8, 28, 49]. Glue-spalling was originally a technique for glass surface decoration [50]. A schematic of the process is shown in Figure 2.3.5. The epoxy is first spread on the sandblasted glass surface and waited until it hardens. When the temperature is lowered, the mismatch in CTE and the restraint from glass cause the epoxy cracks into islands. When the temperature further decrease, the mismatch in CTE develops pressure in the epoxy and glass. The generated cracks propagate into the glass and create a scalloped surface. The circumstance is very close to the concrete surface condition during freeze-thaw cycles, where the ice layer plays the role of the epoxy, and the concrete surface layer plays the role of decorated glass. The CTE of ice is about five times higher than that of cement paste, and the glue-spall stress is calculated to be 2.6 MPa for a temperature decrease of 20°C, which is capable of damaging the concrete surface layer [28, 49].

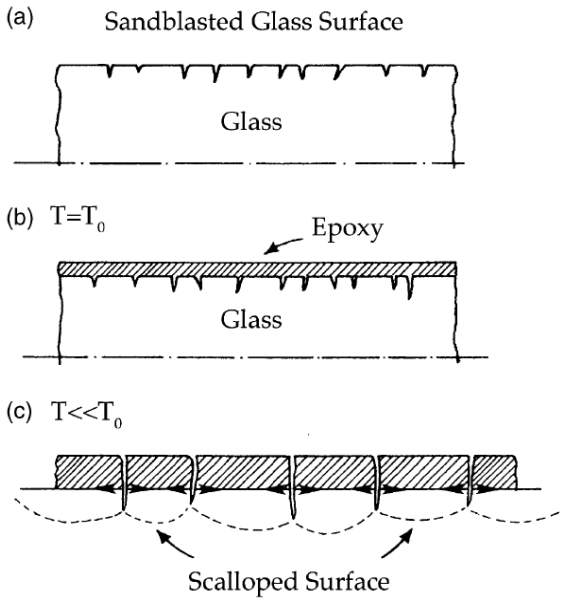

Figure 2.3.5 Schematic of the glue-spalling technique: (a) original sandblasted glass surface; (b) epoxy/glass composite at initial temperature; (c) interface of the composite when the temperature goes down, where the epoxy breaks into islands and creates scalloped surface by spalling [28].

Çopuroğlu and Schlangen [51] conducted numerical modeling of surface scaling deterioration with the Delft Lattice Model based on the glue-spall theory. The results showed a quite realistic fracture pattern, as shown in Figure 2.3.6. The outcomes in the paper indicated that the glue-spall theory could explain the surface scaling damage.

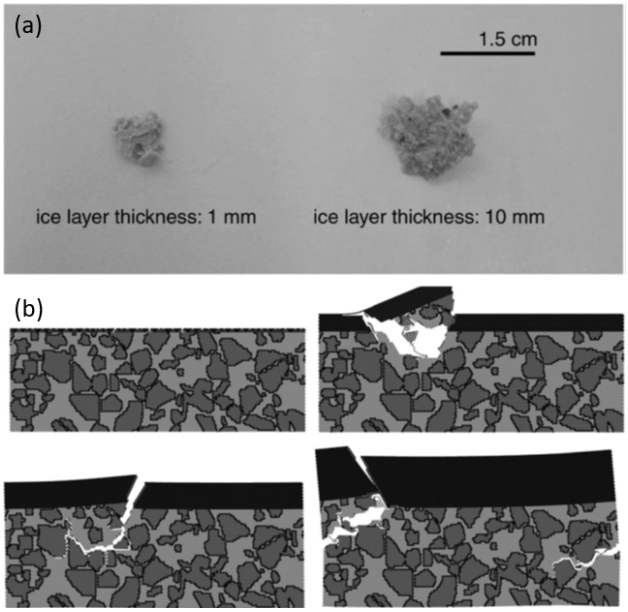

Figure 2.3.6 Scaling flakes from the (a) experiment - mortar specimens having 1 mm and 10 mm thick ice layer on top; (b) modeling – specimen with different ice layer thicknesses (1, 3, 5, 10 mm) on top [51].

2.4 Influence factors of freeze-thaw performance

Although there are still debates on the underlying mechanism, most theories agree on similar factors that are significant to freeze-thaw performance. This fact allows scientists and engineers to estimate and improve the freeze-thaw performance of concrete. On OPC concrete, the influencing factors are

relatively well studied. However, this is not the case for the AAMs concrete. To the knowledge of the author, systematical study on the AAS freeze-thaw performance is very limited, as discussed in section 2.2.

Nevertheless, based on the available information, it seems that the significant parameters of OPC concrete, such as pore structure, humidity, and entrained air voids, are still largely physicomechanical dependent instead of relating to the chemical nature. And it might be able to deduce the performance of AAMs concrete from these characteristics. Therefore, this section also includes the literature based on OPC concrete.

2.4.1 Raw materials

From the perspective of freeze-thaw resistance, research in OPC concrete showed that certain differences can be expected in concrete made from different cements [52-54]. Regarding the raw materials, the raw materials used in producing AAMs are generally industrial by-products. And as a result, the consistency of the raw materials' chemical composition is relatively poor. High variation might be expected between different suppliers and even different batches. On the other hand, it is well known that the microstructure of AAS can be significantly influenced by raw materials. Therefore, it could be deduced that raw materials will likely have a certain influence on the resultant AAS concrete freeze-thaw behavior.

Glukhovsky et al. [55] (cited by Shi et al. [2]) found that the nature of slag did not influence the freeze-thaw resistance of AAS concrete cured under steam. On the other hand, for the AAS concrete cured under room temperature, the basicity of the slag ($(CaO + MgO + Al_2O_3) / SiO_2$) has a significant effect on the resultant freeze-thaw resistance. The AAS concrete made with acidic slag exhibited the poorest freeze-thaw resistance.

Özdal et al. [56] investigated the internal cracking frost resistance of AAS concrete prepared by a combination of two different kinds of slag: ferrochrome slag (FS) and ground granulated blast furnace slag (GGBFS). It was found that the freeze-thaw resistance increased with increasing GGBFS content in the precursor. Mixtures with high FS content fell apart before reaching the end of the test, i.e., 300 freeze-thaw cycles.

In all, there is minimal available information regarding this aspect, and further research might be needed.

2.4.2 Mix proportions

The freeze-thaw resistance of the concrete is significantly dependent on the concrete microstructure. Most theories attribute the initiation of freeze-thaw damage to the freezing in capillary pores. And most theories treat permeability as a crucial factor. In this perspective, the pore structure of the concrete is highly dependent on the mix proportion, especially the mix design of the binder.

In OPC concrete, the pore structure is strongly dependent on the water/cement ratio. With a higher water/cement ratio, the resultant concrete has a more porous microstructure and a higher permeability. For a binder with a higher water/cement ratio, the matrix has more freezable water, which can subsequently cause damage during the freeze-thaw cycles. This results from the higher content of unreacted water as well as the higher external water ingression due to the higher permeability. However, for a binder with a lower water/cement ratio, the finer pore structure might also induce higher internal disruptive pressure during the freeze-thaw cycles, whether it is from the hydraulic pressure point of view or crystallization pressure point of view. Therefore, theoretically, the influence of the pore structure is a competition between the lower freezable water content and the

increasing internal disruptive pressure. In practice, most of the research on OPC concrete found the resistance to freeze-thaw cycles increases with decreasing water/cement ratio [8, 41, 57-62].

From the perspective of AAMs, the microstructure depends on many aspects, such as the type of precursor, type of activator, water/binder ratio, alkaline content, modulus, etc. [1, 2, 63, 64]. There are many factors, but the study on the freeze-thaw performance of AAMs is still in its infancy. Only minimal literature is available, and many are not systematically conducted. In general, the trend is similar to that observed in the variation of water/cement ratio: the denser the microstructure, the better freeze-thaw performance.

One of the crucial factors is the type of alkali in the activator. Many types of alkaline solutions can be used for producing AAS, including sodium silicate, sodium hydroxide, sodium carbonate, etc. Among these options, sodium silicate-activated slag has a much denser microstructure than sodium carbonate-activated slag and sodium hydroxide-activated slag [64]. Timokovich [65] (cited by Shi [2]) compared the freeze-thaw performance of sodium silicate-activated slag and sodium carbonate-activated slag. It was found that the sodium silicate-activated slag has better freeze-thaw resistance, regardless of the basicity of the slag. The sodium silicate-activated slag concrete deteriorated slowly from the surface while the sodium carbonate-activated slag concrete destructed over the whole specimen. Gifford and Gillott also found the same conclusion in their study [25]. Wu [66] compared the surface scaling resistance of sodium silicate-activated slag mortar and sodium hydroxide-activated slag mortar with the same alkali content and water/binder ratio. It was found that sodium silicate-activated slag mortar has a considerably better surface scaling resistance with more than 75% scaling reduction in most mixtures. The much better performance was attributed to the denser microstructure. Talling and Krivenko [67] also noted a similar trend when comparing the internal cracking resistance of sodium silicate-activated slag concrete and sodium hydroxide-activated slag concrete. The silicate-activated slag in their test could withstand 1000 freeze-thaw cycles, while the hydroxide-activated slag specimens failed between 200 and 700 cycles.

The most similar factor in AAMs to water/cement ratio in OPC might be the water/binder ratio. Byfors et al. [68] investigated the surface scaling resistance of F-concrete with water/binder ratios equal to 0.32, 0.40, 0.50, and different air content. The precursor is slag, and the activator is a combination of sodium hydroxide, sodium carbonate, lignosulphonate, sodium gluconate, and tributyl phosphate. The test was conducted following a preliminary Swedish standard in the environment of 3% NaCl solution. The results showed that surface scaling resistance is significantly reduced by increasing the water/binder ratio, while the influence of entrained air content is minor.

Cai et al. [27] investigated the influence of activator/slag ratio (A/S, in the range of 0.54-0.58), slag content, and sand ratio on the frost internal cracking resistance of AAS concrete by response surface methodology. The rank of the factors' significance was found to be A/S > slag content > sand ratio. The frost internal cracking resistance increased with increasing A/S and slag content, while the sand ratio only had a minor influence. Nevertheless, more than half of the samples exhibited good internal cracking frost resistance with a remained dynamic elastic modulus higher than 90%. However, from the author's perspective, their selected range of factors could be widened.

Coppola et al. [69] investigated the freeze-thaw resistance of three one-part alkali-activated slag mortars with varying alkali content between 3.5% to 7.5% (mixture AAS8, AAS12, and AAS16, where the value in the name is in proportional to alkali content). The activator alkaline powder is a blend of sodium silicate, potassium hydroxide, and sodium carbonate with a relative mass ratio of 7:3:1 and a constant silica modulus of 0.48. The freeze-thaw test is done following the Italian Standard UNI7087, which mainly addresses internal cracking damage. The results showed the AAS8, which has the lowest alkali content, has the poorest freeze-thaw resistance and suffered a compressive strength loss of 67% after 150 freeze-thaw cycles. On the other hand, the AAS with

higher alkali content (AAS12, AAS16) showed similar behavior with a strength loss of around 25%. A similar trend was also observed in the variation of elastic modulus. Overall, not much in-depth discussion was carried out in the paper, and the poor performance of the mixture AAS8 was attributed to the high porosity and micro-cracks observed with the optical microscope. In addition, although the stiffness trend was reasonable, using ultrasound on such small specimens (4×4×16 cm3) seems less reliable. The authors did not describe the detailed configuration of the ultrasonic test. However, the ultrasound wavelength used for testing cementitious materials is larger than 4 cm in most cases, i.e., wider than the specimens' cross-section.

Chen and Wang [70] investigated the performance of AAS concrete by conducting the freeze-thaw test following China standard GB/T 50082. The test environment was pure water, and the variation of mass, strength, and dynamic elastic modulus was monitored. The performance of mixtures with different slag content and water/binder ratio was compared. The author commented the mass loss is significantly reduced with increasing slag content. However, the overall mass loss of the poorest mixture is only around 1.5%, and the difference between the mixtures is far from significant. Nevertheless, based on the results from the evolution of strength and stiffness, it could be found that the freeze-thaw resistance slightly improved with the increasing slag content, which is in line with the Cai et al. study [27]. The minor extent of mass loss again conformed to the phenomenon that surface scaling damage is minor when concrete is subjected to pure water without de-icing salt [8]. The authors also investigated the effect of the water/binder ratio, but their concrete quality was very questionable. The compressive strength of the medium water/binder ratio mixture was higher than that of the lowest water/binder ratio, whose strength was equal to the mixture with the highest water/binder ratio. Nevertheless, though the quality control seems to be questionable, the results showed that the freeze-thaw resistance positively correlates to compressive strength.

2.4.3 Degree of saturation

Fluid ingress is a primary factor that causes freeze-thaw damage in the concrete. The degree of saturation is closely related to the deterioration of concrete during the freeze-thaw cycles [31-36]. Damage can occur after one single freeze-thaw cycle if the concrete is fully saturated, regardless of the entrained air system [33, 35]. The concept of critical degree of saturation refers to the fact that if the degree of saturation of the concrete is beyond the critical status, the damage during the freeze-thaw cycles is inevitable[31-36]; while if the saturation status is under this crucial status, the damage is unlikely to happen even a large number of freeze-thaw cycles is conducted. An illustration is shown in Figure 2.4.1.

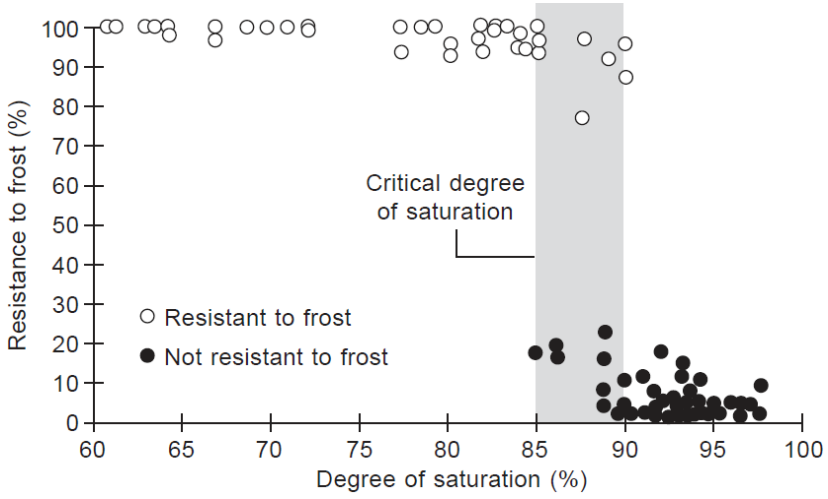

Figure 2.4.1 Effect of degree of saturation on the freeze-thaw performance of concrete. Figure adapted from [11] and data is from [71].

Li et al. [35] investigated the freeze-thaw behavior of specimens with different degrees of saturation by acoustic emission. The precise degree of saturation of the specimen was acquired by meticulous and reasonable preconditioning. Figure 2.4.2 shows that the freeze-thaw damage occurred on samples with a degree of saturation higher than 86% as soon as the first freeze-thaw cycle. On the other hand, no damage was observed on the specimens with a lower degree of saturation, regardless of the number of freeze-thaw cycles. Though there might still be some doubt about the exactness of the degree of saturation, the trend clearly showed that there is a threshold for the critical degree of saturation. In addition, it was also found that the air entrainment significantly increased the time needed for the samples to reach the critical degree of saturation. The required time is prolonged to a few years for samples that are fully immersed underwater. In addition, the author found that the critical degree of saturation seems independent of the entrained air content.

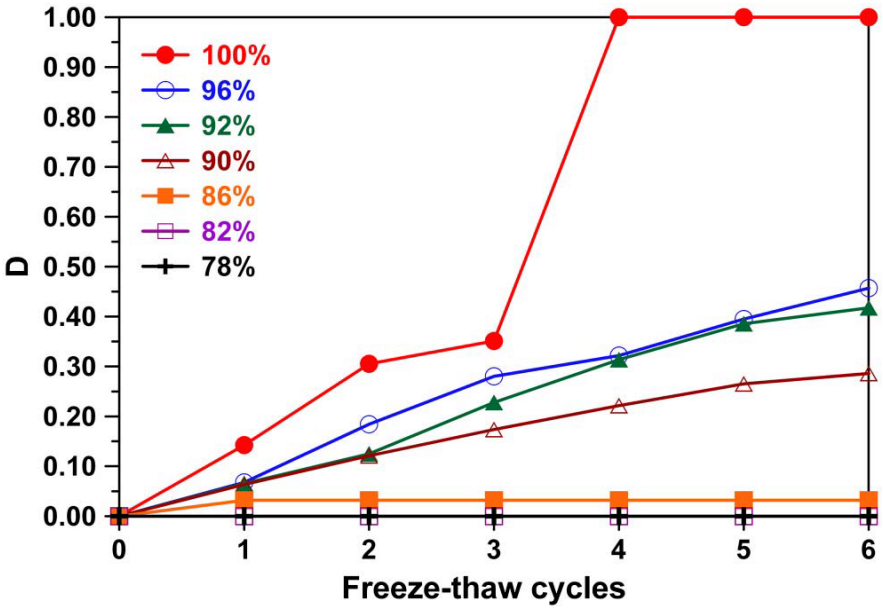

Figure 2.4.2 Decrease of the relative dynamic elastic modulus with freeze-thaw cycles of the specimen with 13% air content by volume of paste [35].

2.4.4 Curing and preconditioning

The curing regime has a significant influence on the properties of the resultant AAMs binder. Exposed to the external environment, the few millimeters below the surface can have a microstructure quite different from the bulk of the concrete and considerably influenced by the curing condition [29, 66, 68, 72-75]. Considering that this layer deteriorates and scales off during the surface scaling frost test, the curing might have a considerable influence on the surface scaling resistance of concrete [54, 57, 76]. In addition, the preconditioning procedure in the test might also have a similar effect [10].

Collins and Sanjayan [29] investigated the effect of curing regimes on the surface cracking, water sorptivity, and pore structure of AAS concrete and paste. Following the demolding on day 1, the samples were subjected to bath curing (immersed in saturated lime water), sealed curing (sealed in two polythene bags and a sealed container), and exposed curing (exposed to ambient air at 50% RH). The exposed curing resulted in lower compressive strength and strength loss between 28 days and 365 days. Microcracking was initiated in the first three days after exposure, and widths of cracking developed to as high as 0.3mm. Tested by MIP, the total porosity and pore size distribution of the exposed curing sample was also considerably higher than the bath curing sample and sealed sample. In addition, a clear difference between the microstructure of the outer part and the internal part was

found. As a result of microcracking and porous microstructure, higher water uptake was also found in the exposed sample. Therefore, poorer durability can be expected on the exposed curing sample.

Çopuroğlu et al. [76] investigated the surface scaling resistance of slag cement mortars cured under eleven curing regimes. It was found that, among the samples without carbonation, curing in deionized water gave the poorest surface scaling resistance, while curing under limewater gave the best scaling resistance.

Wu [66] investigated the mechanical properties and durability of AAS mortar cured under five different curing regimes: ambient curing (exposed to ambient air), sealed curing, fog curing, water curing, and limewater curing. Surface cracking was also noticed on the surface of the exposed curing sample. The resistance to surface scaling was tested by a procedure modified from the CDF test. As shown in Figure 2.4.3, the exposed curing results in a significantly poor surface scaling resistance, and the scaling is several times higher than other mixtures. Excluding the result of the exposed curing sample, an unneglectable influence was still observed, as shown in Figure 2.4.4. Sealed curing gave the best surface scaling resistance, whose scaling was half of the fog curing sample. And limewater seems to have a small benefit on the resultant surface scaling resistance compared to the result of tap water curing. The poorer performance of the specimens cured under humid conditions and the slight improvement by limewater were attributed to the leaching of Ca^{2+}, which can result in a lower degree of reaction [77].

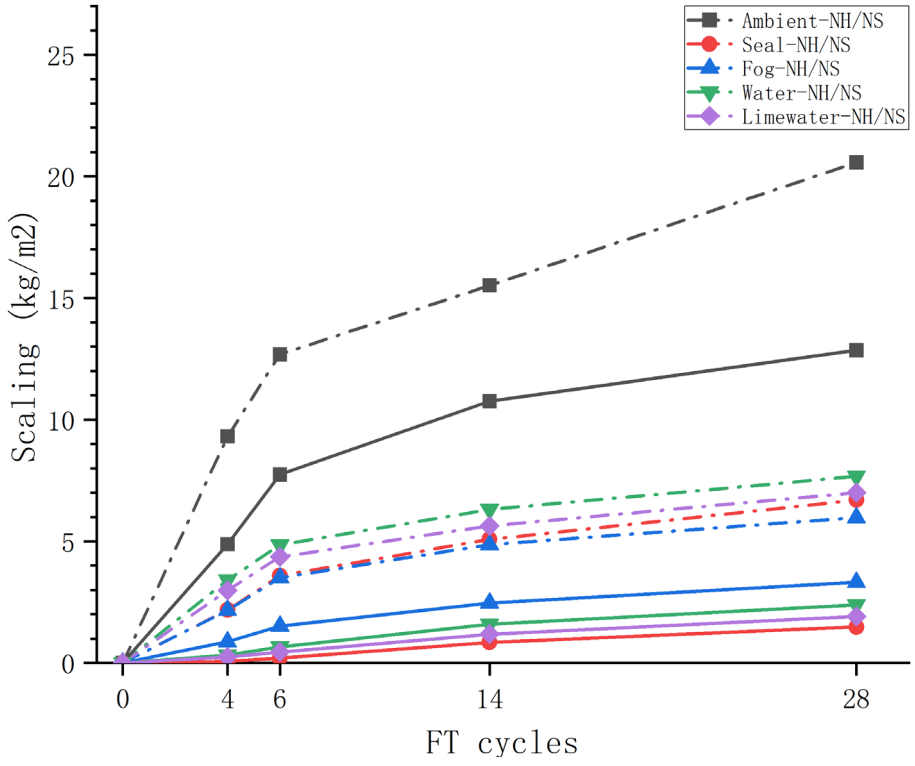

Figure 2.4.3 Surface scaling of mixtures underwent different curing regimes, where the dash lines stand for the sodium hydroxide-activated slag mortar and solid lines stand for the sodium silicate-activated slag mortar [66].

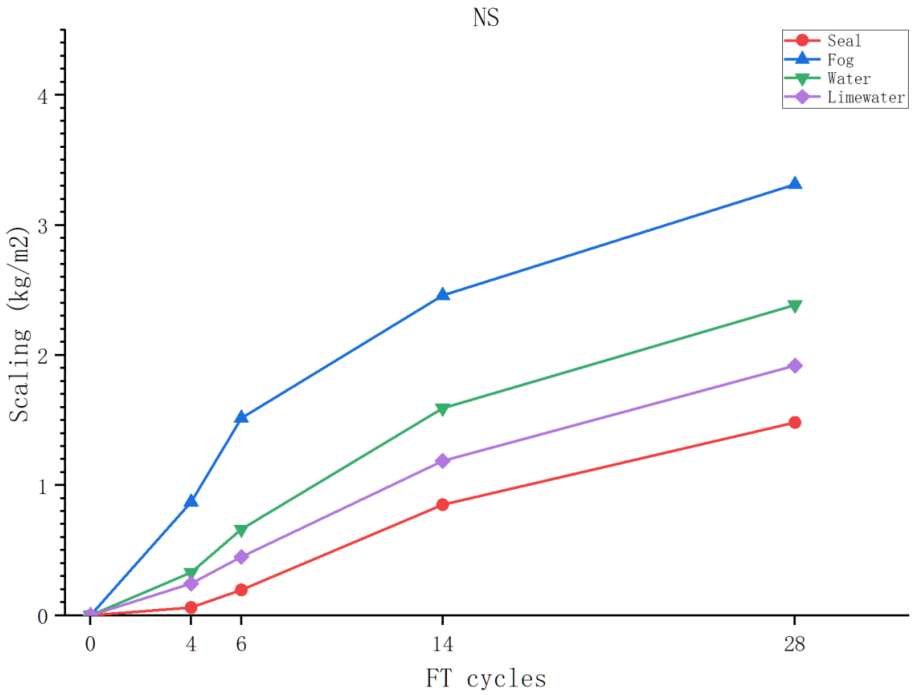

Figure 2.4.4 Surface scaling of sodium silicate-activated slag mortar cured under different curing regimes [66].

Therefore, the preconditioning procedure regulated in the test protocols might also have an unneglectable influence on the surface scaling resistance—the testing methods and protocols in force designed for OPC but not AAMs. Although the OPC and AAM are similar to an extent, they are different in nature and might show a different response when subjected to the same condition. Some of the procedures addressed in the current standard and regulation are proper to the OPC, but they might induce unnecessary defects on the AAM and further underestimate the performance of AAMs. For instance, the curing and surface drying procedure is regulated in both the CDF test and the ASTM C672 test. For the CDF test, the curing procedure is held as 7-day underwater curing, and the drying procedure starts right after 7 days and lasts for 21 days; for the ASTM C672, the curing procedure is described as moist curing for 14 days, and the drying procedure starts right after and lasts for 14 days. From the perspective of curing, underwater curing is beneficial to OPC; but it might lead to leaching and coarsens the microstructure of AAS. In terms of surface drying, starting the drying at day 7 might have a minor influence on OPC; but it might lead to surface microcracking on AAMs because of the higher cracking potential. Therefore, the feasibility of the current standard procedure for AAMs is unclear and demands a more comprehensive study [10].

Carbonation might also play a significant role in freeze-thaw damage, especially in the form of surface scaling. AAS binder is much more susceptible to carbonation than OPC binder [10, 78-80]. For the OPC binder, carbonation occurs in both portlandite and the C-S-H gel. The carbonation of portlandite results in calcium carbonate sedimentation, which densifies the binder's microstructure and slows down the following carbonation ingression [71]. In contrast, the AAS binder does not contain portlandite. The carbonation directly occurs on the C-(A)-S-H gel. The decalcification of C-(A)-S-H gel results in a loss in cohesion of matrix, higher porosity, and lower mechanical properties, which significantly lower the durability [10, 78-80]. Carbonation can also be found in young AAS concrete if it is exposed to ambient air at an early age, i.e., improper curing and preconditioning [66]. As discussed above, the higher porosity and weaker matrix are not favorable for the freeze-thaw resistance, especially from the perspective of surface scaling [9, 54]. Therefore, it can be easily deduced that carbonation will significantly reduce the surface scaling resistance.

Çopuroğlu et al. [76] investigated the effect of carbonation on the slag cement mortar. Exposure to ambient laboratory air and 3% CO_2 environment resulted in carbonation of the binder, which restructured the capillaries system and considerable increased the porosity. A significantly higher scaling over the freeze-thaw cycles was observed on the carbonated specimens.

2.4.5 Test solution concentration

The liquid environment that samples are subjected to during the freeze-thaw test has a significant influence, especially on the surface scaling behavior. This has been briefly discussed above. The test solution for testing internal cracking resistance is usually distilled water, while surface scaling resistance is usually de-icing salt solution. The concentration of test liquid has a considerable influence on the scaling behavior of concrete.

When the concrete is subjected to pure water, the extent of scaling is usually minor [12, 13, 24-26]. On the other hand, a pessimum solute concentration of around 3% was found in the literature. Verbeck and Klieger [81] investigated the influence of de-icing solution concentration on the surface scaling of OPC concrete. The test was conducted on calcium chloride, sodium chloride, urea, and ethyl alcohol solution with a concentration ranging from 0% to 16%. As shown in Figure 2.4.5, the maximum scaling was found when the de-icing solution concentration was around 3%, regardless of the type of de-icer. Marchand et al. [30] investigated the effect of NaCl test solution concentration on the surface scaling of OPC concrete with a water/cement ratio ranging from 0.25 – 0.45. The test was conducted in accordance with ASTM C672. The pessimum effect was also observed, and the highest scaling deterioration was found at a low NaCl concentration (1.5% or 3%).

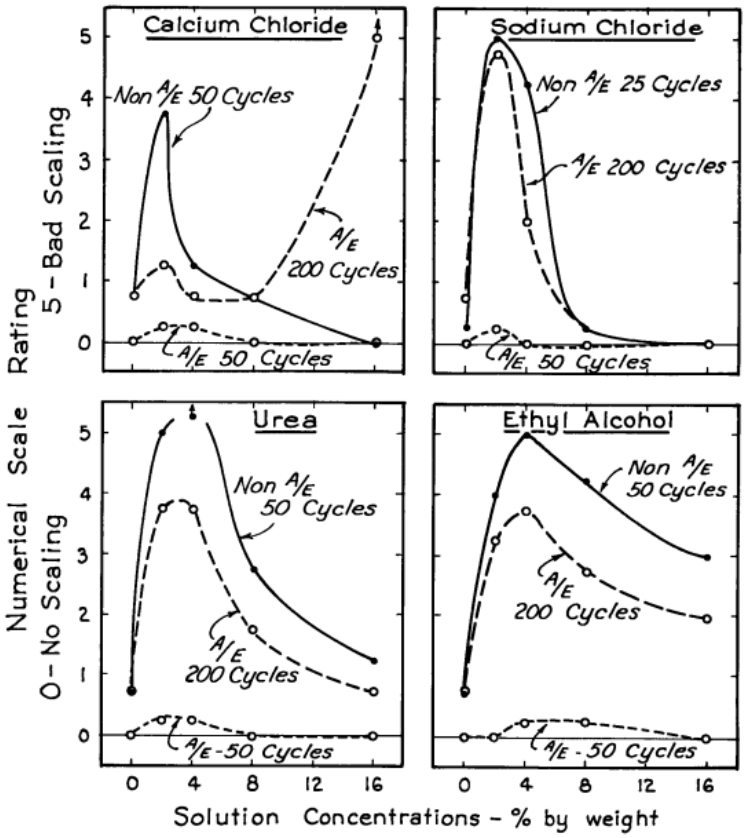

Figure 2.4.5 Results from the reference [81] showing the maximum scaling damage occurred at a de-icing solution concentration of around 3%, where calcium chloride, sodium chloride, urea, and ethyl alcohol were used as the test solution.

Valenza and Scherer [28, 49] proposed the glue-spall theory to explain the surface scaling deterioration. Theory gave a good explanation of the pessimum effect of the brine concentration. When the brine concentration is low, the creep limits the stress development in the ice layer and cannot break the ice into many islands. When the ice has a moderate concentration (around 3%), the stress development in the ice layer is higher than the strength, and the ice layer can crack, which subsequently causes damage. When the ice has a higher concentration, the ice layer is too weak to impose stress on the concrete [28, 49, 51]. Based on the glue-spall theory, Çopuroğlu and Schlangen [51] conducted numerical modeling of surface scaling deterioration with the Delft lattice model and reproduced the pessimum effect, as shown in Figure 2.4.6.

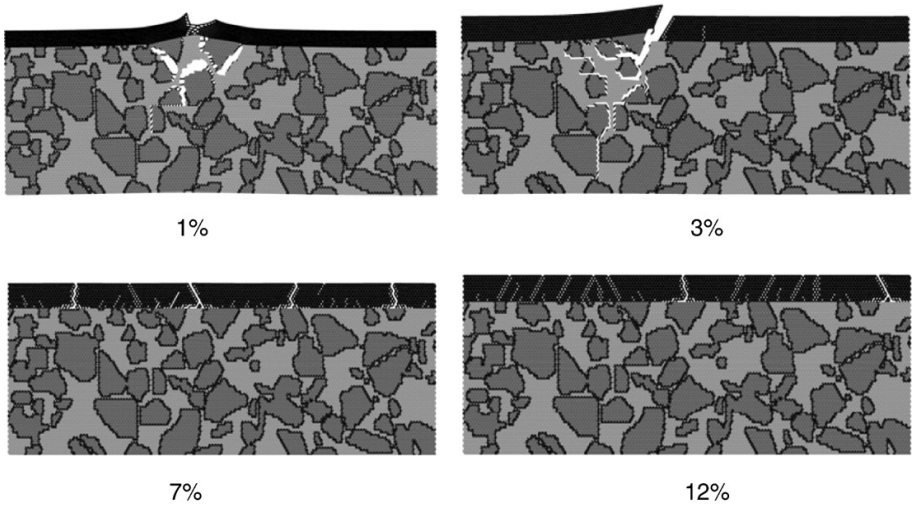

Figure 2.4.6 Numerical modeling of the pessimum effect of surface scaling based on glue-spall theory [51].

2.5 Improving freeze-thaw resistance by entraining air voids

As mentioned above, the mechanisms and driving forces behind the freeze-thaw damage is still under debate. Fortunately, most of the proposed theories are based on similar controlling factors. Therefore, the improving methods of freeze-thaw performance have been comprehensively studied and proven on OPC. Due to the similarity, the gained experience might be used as a reference for improving the freeze-thaw resistance of AAMs. In general, the starting points for improving freeze-thaw resistance can be summarized as follows:

Limiting the generated pressure during freeze-thaw cycles: this can be achieved by proving empty air voids in the concrete matrix, i.e., air-entraining, with the help of air-entraining agents (AEA) or superabsorbent polymers (SAP).

Limiting the amount of freezable water and degree of saturation: this can be achieved by adding supplementary cementitious materials (SCMs) and fine particles or adding hydrophobic agents.

Limiting the crack development: this can be achieved by applying fiber reinforcement.

Among these solutions, limiting the generated pressure during freeze-thaw cycles by entraining empty air voids is the most widely used one and will be discussed in detail in this section.

2.5.1 Mechanisms

Air-entraining is the most classic improving method for freeze-thaw deterioration. The role of the air voids during the freeze-thaw cycles is comprehensively studied by Sun and Scherer [40]. As observed in the literature [40, 82] and shown in Figure 2.5.1, during the freeze-thaw cycles, mortar without air-entraining expands and exhibits uncovered deformation after one single cycle. The expansion is attributed to the hydraulic pressure and crystallization pressure, owing to the rapid growth of ice. In contrast, mortar with air voids entrained contracts during the freeze-thaw cycles.

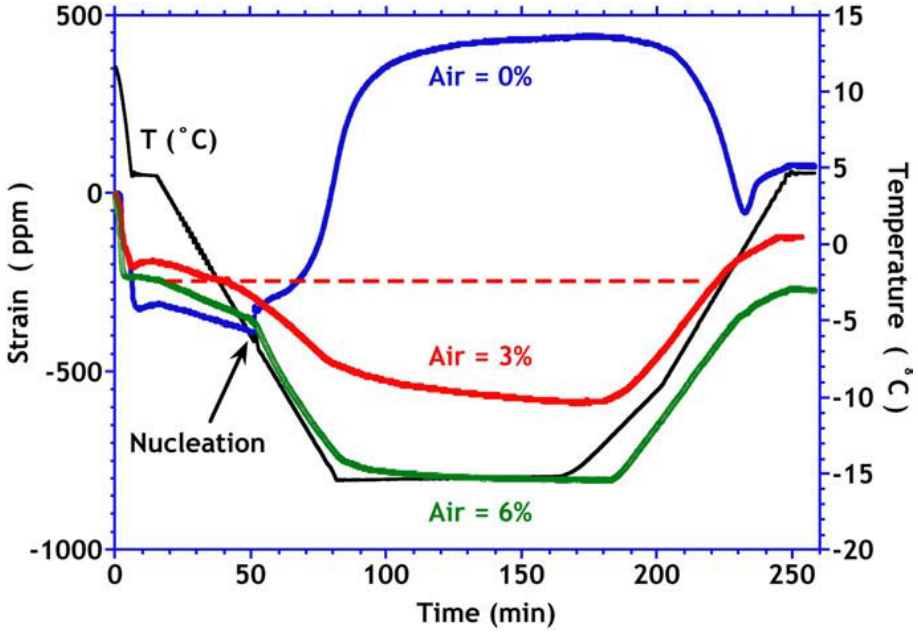

Figure 2.5.1 Strained measured during cooling of saturated mortar with the nucleating agent metaldehyde in the differential mechanical analyzer—the air-entrained samples contract immediately upon freezing while the non-air-entrained sample expands [40].

From the hydraulic pressure theory perspective, the entrained air voids can limit the damage. The freezing of water in the mesopores occurs at an undercooling due to the small pore radius and solutes. Sun and Scherer [40] calculated the volume fraction of ice that freezes at a given undercooling by differential scanning calorimeter and discussed the consequence. Considerably high volume fraction and ice growth rate were found, and the resultant hydraulic pressure is quite damaging in non-air entrained mortar. In the air-entrained mortar, the air voids allow the water to move in and limit pressure development.

Once the pore water flows into the air voids, it freezes into spherical crystal on the wall of the air voids [83, 84], as shown in Figure 2.5.2. The crystal sucks water from the pores and creates a negative pressure in the pore water, which causes the contraction observed on the air-entrained mortar. Poromechanical analysis and calculation were conducted by Coussy [85], Sun and Scherer [40]. For a temperature down to -25℃, theoretically calculated strain quantitively conformed to the experimental results. The resultant strain not only offsets the expansion created by the ice but also results in additional contraction on the body and protects the mortar from damage.

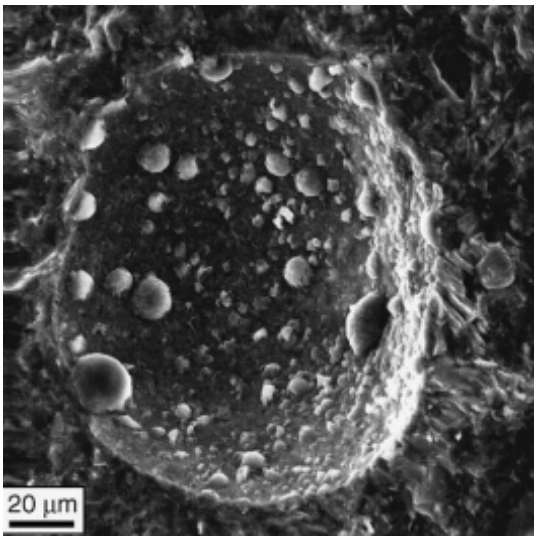

Figure 2.5.2 Growth of ice crystal in air voids, adapted from [83].

This beneficial contraction also accounts for the protection of surface scaling [40]. According to glue-spall theory, the stress that causes cracking is generated by the mismatch in CTE between concrete and ice [28, 49]. For the air-entrained mortar, the contraction caused by the nucleation in air voids compensates the extent of mismatch and reduces the damage.

From the perspective of the critical degree of saturation, air voids also have a considerable contribution. Li et al. [35] systematically investigated the effect of air-entraining on the water ingression behavior and the evolution of the degree of saturation when subjected to water immersion. OPC mortar sample with an air content of 6% (without air-entraining), 10%, and 14% (with air-entraining) was prepared. After curing for 28 days, the samples were placed in 50%, 65%, and 80% RH environments for more than one year to equilibrate. After that, the water absorption of the samples was tested with a procedure similar to ASTM C1585, where the sample was fully immersed for more than 256 days instead of one side immersed for 9 days. As shown in Figure 2.5.3, the calculated degree of saturation over time showed that specimens without air-entraining reached the critical degree of saturation after 4-6 days. In contrast, the specimens with air-entraining never reached the critical degree of saturation during the test, and the required time estimated by regression is more than three years.

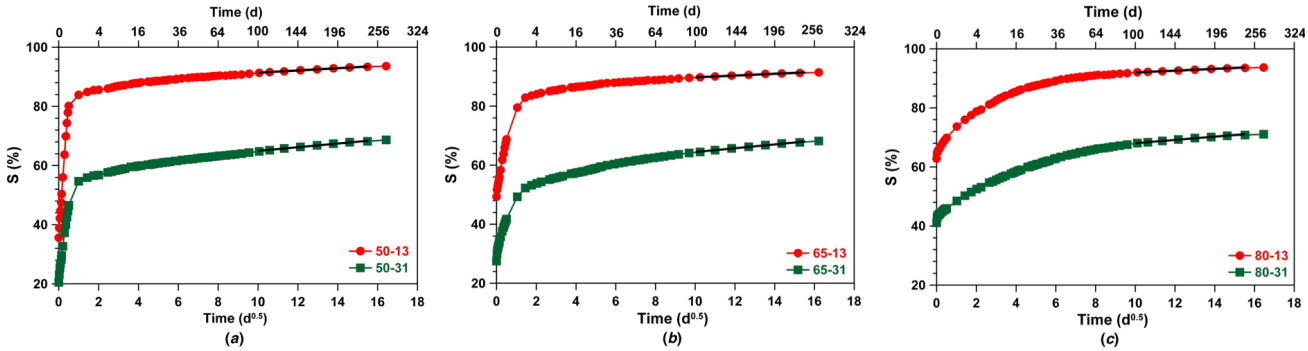

Figure 2.5.3 Results of the sorptivity test provided as an increase in the degree of saturation: (a) 50% RH; (b) 65% RH; (c) 80% RH. The red line stands for the non-air-entrained sample (6% mortar air content), and the green line stands for the air-entrained samples (14% mortar air content). Figures are adapted from [35].

However, it should be pointed out that the local pressure caused by crystallization might still inevitably create tensile stress on the pore wall and might lead to fatigue damage after several freeze-thaw cycles [40, 86].

In order to entrain air voids in the matrix, different types of AEA have been widely used in the concrete industry for many decades. Recently, SAP is also used for this purpose.

2.5.2 Air-entraining agent (AEA)

Air-entraining agents (AEAs) are surfactant-based admixtures that can stabilize the air voids in the paste of concrete [84]. Surfactants are amphiphilic molecules with a hydrophobic hydrocarbon chain and a hydrophilic head group, which adsorb at the interfaces between the paste and air voids [84, 87]. The type of AEA is characterized by its head group charge, for instance, anionic, cationic, amphoteric, and non-ionic. The most widely used AEA currently is the anionic type [84].

Douglas et al. [24] investigated the entrained air voids system and the performance of several air-entrained AASC specimens. Air entrainment was successful with the use of a sulfonated hydrocarbon-type AEA. The air void parameters tested from fresh concrete and hardened concrete indicated the air void system was relatively poor, and there was a loss of entrained air content during hardening. The authors did not state the method used to determine the air content. The freeze-thaw resistance was tested by ASTM C666, and the result was satisfactory. However, there was no reference concrete without air-entraining, so the contribution of air-entraining was unclear.

Gifford and Gillott [25] found not all the AEA can effectively entrain air voids in AAS concrete. An AEA consisting of an aqueous solution of modified salts of a sulfonated hydrocarbon was found to be ineffective in the AAS concrete. On the other hand, an AEA initially designed for low-slump concrete or high-alkali cement concrete was effective. However, the active ingredient is confidential. The internal cracking resistance of AAS concrete is reasonably good, but again, no reference without AEA was tested.

Matalkah and Soroushian [12] compared the surface scaling resistance of an alkali aluminosilicate concrete (AAC) with and without AEA following ASTM C672. The precursor of the AAC is a trinary system consisting of coal fly ash, slag, and albite, and the activator is prepared by sodium hydroxide, sodium silicate, and calcium oxide. The brand of AEA is MasterAir AE 90. However, no information regarding the active ingredient is available. Results showed that air-entraining improved the surface scaling resistance of AAC. The cumulative scaling at the end of the test (8 cycles) was reduced by around 40%, and a clear difference can be seen on the test surface.

Coppola et al. [69] investigated the internal cracking resistance of three one-part alkali-activated slag mortars with and without AEA. AEA based on cocamide diethanolamine was used. The activator

alkaline powder is a blend of sodium silicate, potassium hydroxide, and sodium carbonate with a relative mass ratio of 7:3:1 and a constant silica modulus of 0.48. The freeze-thaw test was conducted following the Italian Standard UNI7087. The result showed that AEA reduced stiffness and strength loss by approximately 30% - 50%.

Cai et al. [27] investigated the internal cracking resistance of 17 mixtures of air-entrained AAS concrete. A good correlation between the air voids system and the frost resistance was found, as shown in Figure 2.5.4. The frost resistance coefficient D_F was calculated based on the variation of dynamic elastic modulus and found to be improved with decreasing air bubbles spacing coefficient and increasing specific surface area. The author conducted linear regression between D_F and the air voids parameter. However, non-linear regression might be a better choice considering the boundary conditions.

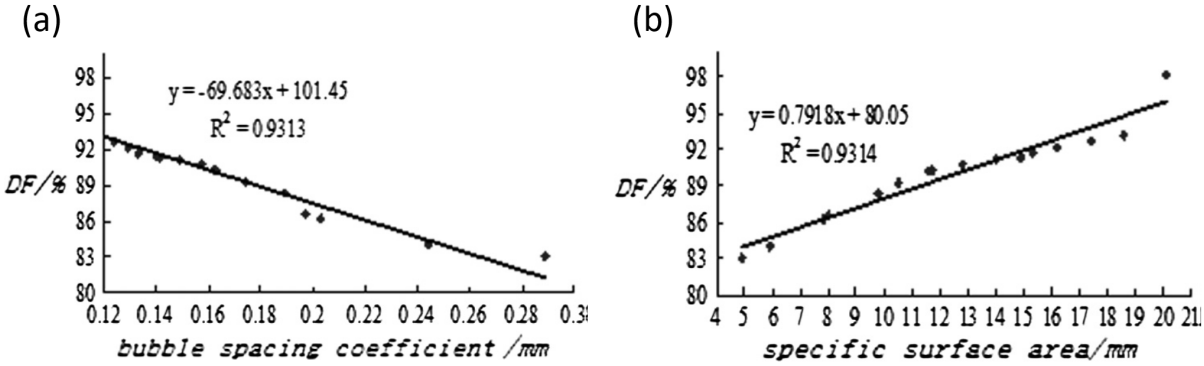

Figure 2.5.4 Relationship between the D_F and (a) air bubble spacing; (b) specific surface area, adapted from [27].

2.5.3 Superabsorbent polymer (SAP)

Superabsorbent polymer is a relatively new admixture for the concrete construction industry. The hydrophilic network consisting of cross-link polyelectrolytes allowed the SAP to absorb water or solution up to thousands of times its dry mass [88]. When the SAP is added to the concrete, it absorbs liquid and swells. During the hardening or desiccation, the SAP releases the absorbed liquid into the concrete [89-91]. With this characteristic, SAP can exhibit multiple functions as a concrete admixture, such as modifying the rheology [92], reducing shrinkage [91, 93], and promoting self-healing [94]. Empty cavities are left in the matrix after the SAP releases the absorbed liquid and dwells. The empty cavities are similar to the air voids created by the AEAs. Therefore, SAP is also used for air-entraining to improve freeze-thaw resistance [90, 95, 96]. And the working mechanism behind is thought to be more or less similar to the traditional AEA method [90, 97].

The effectiveness of using SAP to improve freeze-thaw resistance has been relatively widely studied in OPC concrete, and a related recommendation has been published by RILEM [90]. However, from the perspective of AAMs, the relative study is scarce.

Kusayama et al. [98] investigated the surface scaling resistance of OPC concrete with or without SAP, including a comparative mixture with AEA. The surface scaling test was similar to ASTM C672. Four types of SAPs were used in the study, and one of the SAPs has residual surfactant due to the manufacturing process. Results showed that SAPs improved the surface scaling resistance regardless of the presence of residual surfactant. Nevertheless, the residual surfactant indeed further improved the performance. By comparing with the reference AEA mixture, the effectiveness of SAP was found to be lower than AEA. However, it is noticed that the air content in AEA mixture is 5.8%, which is more than 1% higher than the calculated air content in SAP mixtures (with the assumption

that SAP releases all the absorption). Therefore, the mix design of the AEA reference mixture was not properly controlled, and the dosage of AEA should be reduced.

Laustsen et al. [99] investigated the air voids structure and the resultant surface scaling resistance of OPC concrete with the addition of SAP. The SAP was produced by suspension polymerization. Residual surfactants were found on the SAP, and 99.9% ethanol was used for rinsing SAP to get rid of the surfactants. Mixtures containing SAP with or without rinsing were investigated and comapred. The air voids system was investigated by the pressure gauge on the fresh concrete and scanning on hardened concrete (EN 480-11), respectively. The air content of the non-rinsed SAP mixture was higher than that of rinsed SAP mixtures in both fresh and hardened statuses. In addition, the air content in the fresh concrete of rinsed SAP mixtures was similar to that of the reference mixture without SAP, showing that SAP particles will not entrain additional air voids in concrete before they release the absorbed liquid. A linear relationship was found between the total air content in hardened concrete and SAP dosage. The scope of the linear regression indicated the absorption capacity, which was around 10 g/g and was found to be far from the result tested from CT-measurement (19 g/g). The author suggested this might be due to the inaccuracy of CT measurement. The surface scaling resistance was investigated by the slab test described in EN 12390-9. Results showed that SAP significantly reduced the scaling. A correlation was found between the surface scaling resistance, SAP dosage, and air voids spacing factor. As shown in Figure 2.5.5, the cumulative scaling at 56 cycles reduced with increasing SAP dosage and reducing spacing factor.

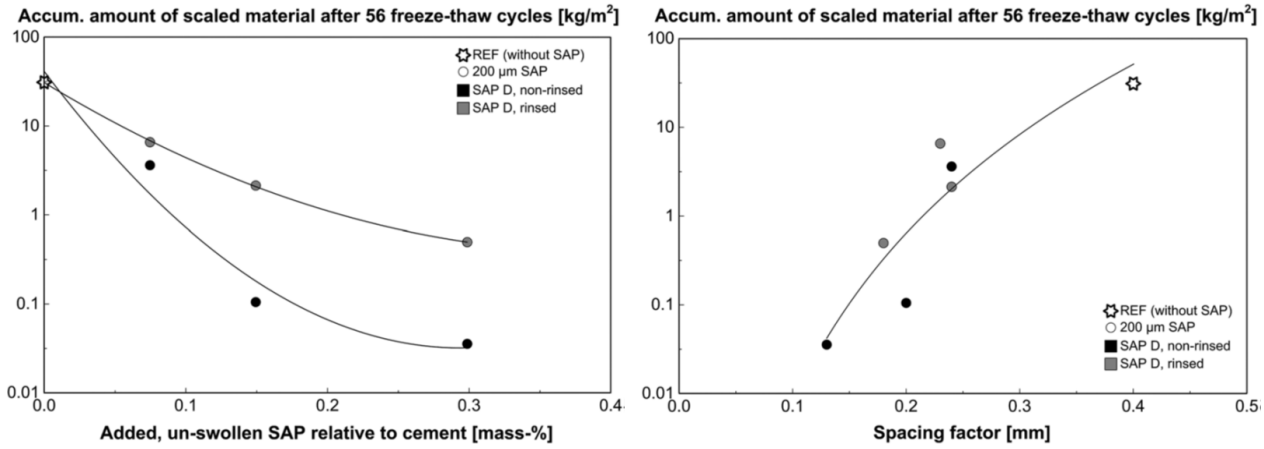

Figure 2.5.5 Accumulated amount of scaled materials after 56 freeze-thaw cycles compared to SAP dosage (left) and spacing factor (right), adapted from [99].

RILEM Technical Committee 225-SAP conducted an interlaboratory experimental study by 13 research groups [100]. The effect and robustness of SAP on the mechanical properties and freeze-thaw resistance were investigated by the same mix design OPC concrete produced with locally available materials. A reduction in mechanical properties was found when additional water was added. And the extent of reduction was similar to a corresponding increase in the water/cement ratio. From the perspective of mechanical properties, SAP has a much smaller influence than traditional AEA. Most research groups found that adding SAP with additional water varied from insignificant to pronouncedly positive effects on the freeze-thaw resistance, depending on the laboratory and test protocols. For the mixtures that SAP added without extra water, the improvement in freeze-thaw resistance was considerably higher. However, the reference samples with AEA showed much higher effectiveness in this aspect.

The study using SAP in AAMs binder to improve the freeze-thaw resistance is minimal. Yang et al. [101] investigated the effect of SAP on the freeze-thaw resistance of AAS mortar according to a Chinese standard JGK/T 70-2009 with water as the test liquid. The effect of SAP dosage (0.1% -

0.3% by weight of slag) was studied. Figure 2.5.6 shows that SAP successfully reduced the strength loss at 200 freeze-thaw cycles by approximately 25% - 65%. With higher dosage, the loss of strength and mass is lower.

Additionally, the authors also studied the effect of mixing methods of SAP. Two mixing procedure was studied: dry mixing stands for adding the dry SAP directly during mixing, while wet mixing included an additional preabsorption procedure. Results showed that the mortar with wet mixing has a smaller strength loss than dry mixing mixtures at the exact dosage. However, the author somehow mistakenly concluded that the dry-mixing mixtures performed better.

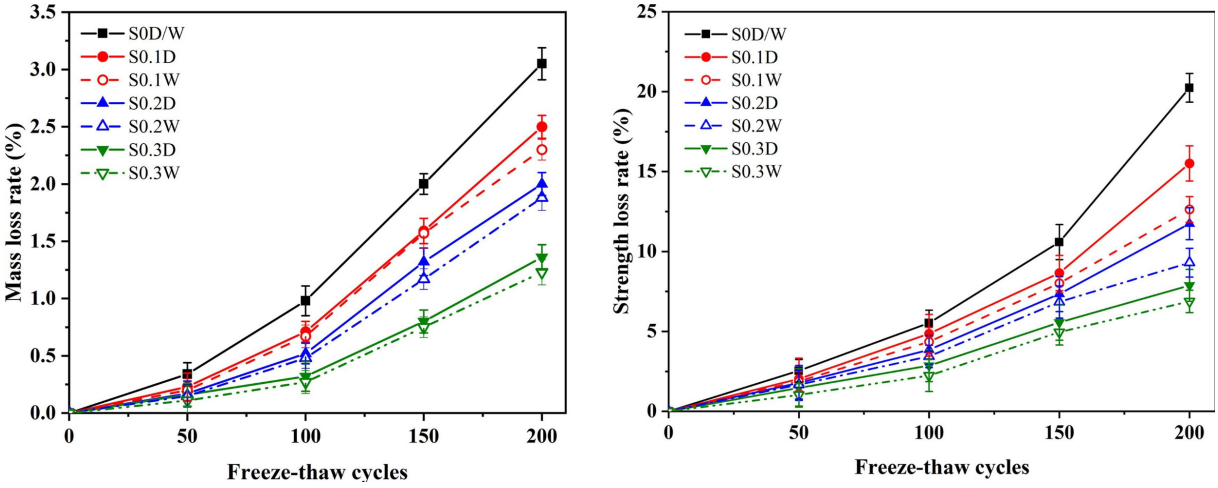

Figure 2.5.6 Freeze-thaw induced mass loss and strength loss of AAS mortar with SAP by dry mixing (D) and wet mixing (W), adapted from [101].

3 Effect of SAP / AEA on workability, air content, and mechanical properties of AASM

3.1 Introduction

Mechanical properties and workability are two of the most concerning and fundamental properties of cementitious materials. The air content in the product is also an essential parameter for air-entrained concrete or mortar. Since AEA and SAP have an influence on these properties, the extent of the impact will be investigated in the chapter. In addition, the raw materials used in the study will also be characterized in this chapter.

Using AEA and SAP will also influence workability. In terms of OPC concrete, it has been widely accepted that AEA can improve workability because of the ball-bearing effect of the tiny air bubbles. This improvement is more noticeable when AEA is added to concrete that initially has low workability, for instance, with coarse sand, low water/cement ratio, and high cement content [84, 102, 103]. When AEA is added to AASC, a similar effect was found in literature workability [69, 104, 105]. In terms of SAP addition, SAP particles absorb liquid from the fresh paste and create a lower water/binder ratio. Therefore, directly adding dry SAP will always lead to a considerable decrease in workability [90, 101, 106-108]. To have acceptable workability, compensation can be made by adding additional water/activator, adding additional superplasticizer, or pre-saturating SAP before mixing [90, 107].

Air content is one of the most fundamental parameters used to evaluate the effect of air voids entraining. The targeted entrained air content for applying AEA in OPC concrete is usually around 6%. In terms of mortar, this value is higher. For SAP, relative information is limited, and the knowledge gained from OPC is usually used. The dosage of SAP is generally around 0.3% by weight of cement in literature.

Mechanical properties are considerably influenced by air-entraining, particularly the compressive strength. For applying AEA in OPC concrete, a rough estimation of its reduction can be made according to the thumb rule: 5% reduction in compressive strength for each 1% increment in entrained air content [109]. For the addition of SAP, the reduction in mechanical properties is reported to be smaller in the literature [90, 95, 100].

Accordingly, the objective of this chapter is to investigate the influence of SAP/AEA on the workability, air content, and mechanical properties of AASM.

3.2 Materials and methods

3.2.1 Materials

3.2.1.1 Blast-furnace slag (slag)

Blast-furnace slag (referred to as slag) is the selected precursor for alkali-activated slag (AAS) binder. The slag used in the study is provided by Ecocem Benelux BV. Blast-furnace slag is an industrial by-product from the manufacturing of iron. The chemical composition of the slag is determined by X-ray fluorescence (XRF) and shown in Table 3.2.1.

Table 3.2.1 Chemical composition of blast-furnace slag

Oxide (wt%)								
SiO_2	Al_2O_3	CaO	MgO	Fe_2O_3	SO_3	K_2O	TiO_2	Other
31.8	13.3	40.5	9.3	0.5	1.5	0.3	1.0	1.9

The phase identification of the slag is conducted by the XRD, as shown in Figure 3.2.1. Diffractogram shows that the used slag is amorphous.

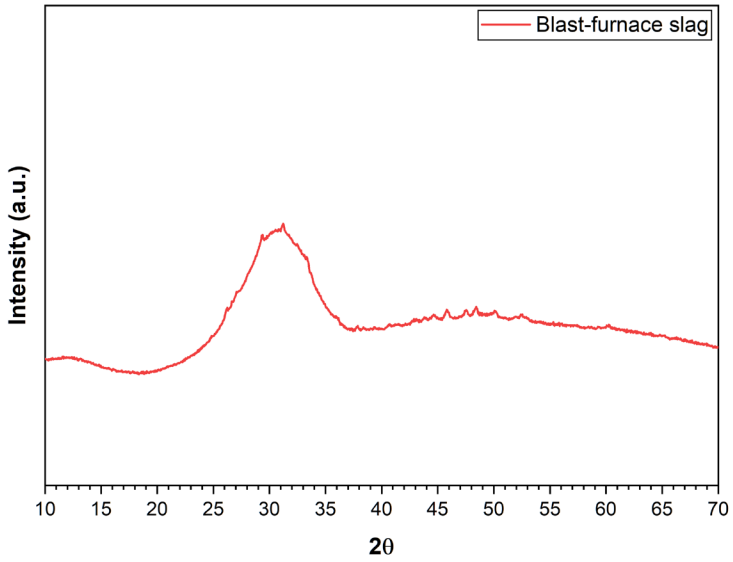

Figure 3.2.1 XRD pattern for blast furnace slag

In addition, the particle size distribution of slag is determined by laser diffraction analysis, as shown in Figure 3.2.2. The d_{10}, d_{50}, and d_{90} of slag are 5.54 um, 20.40 um, and 42.54 um, respectively.

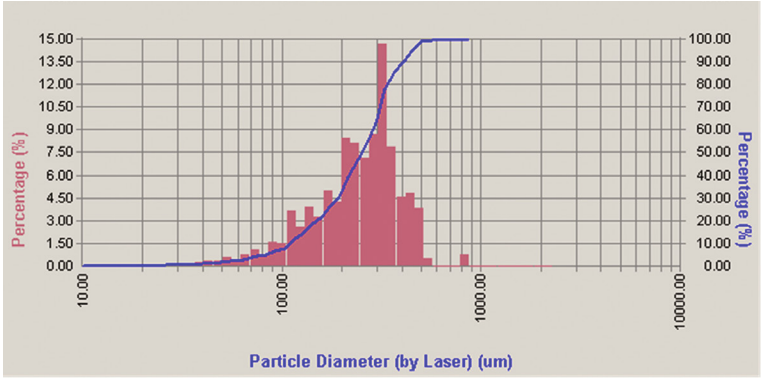

Figure 3.2.2 Particle size distribution of blast-furnace slag tested by laser diffraction

3.2.1.2 Superabsorbent polymer (SAP)

The SAP used in the study is a commercial SAP with the brand of Floset 27cc, supplied by SNF SAS (Andrezieux, France). The SAP is composed of cross-linked acrylamide and acrylate copolymer, manufactured by solution polymerization method. With this production process, the produced SAP particles are irregular, as shown in Figure 3.2.3 [91]. Even so, the particle size distribution of the SAP was measured in a previous study through laser diffraction with ethanol, as shown in Figure 3.2.4 [110]. It can be seen that size of SAP particles in the study is mainly within the range of 200 – 500 um.

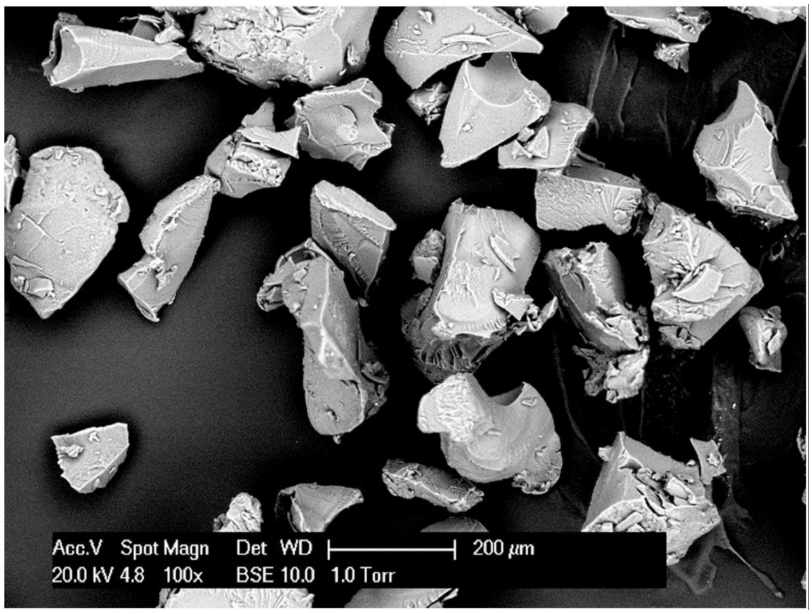

Figure 3.2.3 Scanning electron microscopy image of the dry SAP particles, adapted from [91] where the same SAP was used

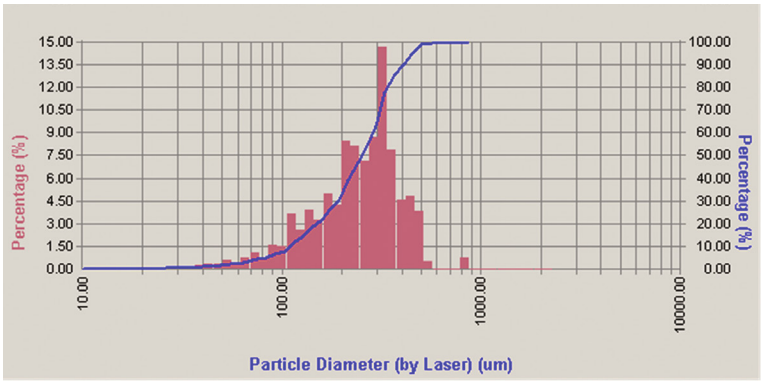

Figure 3.2.4 Particle size distribution of dry SAP, measured by laser diffraction in ethanol, adapted from [110]

SAP absorbs liquid from the surroundings, decreasing the water/binder ratio and workability when added to the fresh cementitious binder. Appropriate efforts are needed to compensate for this loss of workability, such as additional water, pre-wetting, and superplasticizer. In this study, the influence of the compensation method is investigated.

Therefore, before the mix design, the absorption capacity of SAP in the activator was measured by the teabag method described in [111]. Three duplicates were tested. Each teabag contained ~0.2 g SAP. The dry mass was measured before the teabags were fully immersed in the activator. After 10 min, 30 min, 60 min, 3 h, and 24 h, the teabag was removed from the liquid, and the excessive liquid on the teabag was wiped out. Afterwards, the total mass was measured at 0.001 g.

The result is shown in Figure 3.2.5. The absorption capacity of SAP at the end of the test was around 29 g/g. Most of the absorption was within the first hour: approximately 18 g/g at 10 min and around 23 g/g at 60 min. It is noticed that the absorption curve is quite similar to the result in a previous study, where the same SAP was used, but the composition of the activator is different [91]. This observation might indicate that the absorption capacity of SAP in sodium silicate activator is similar to an extent.

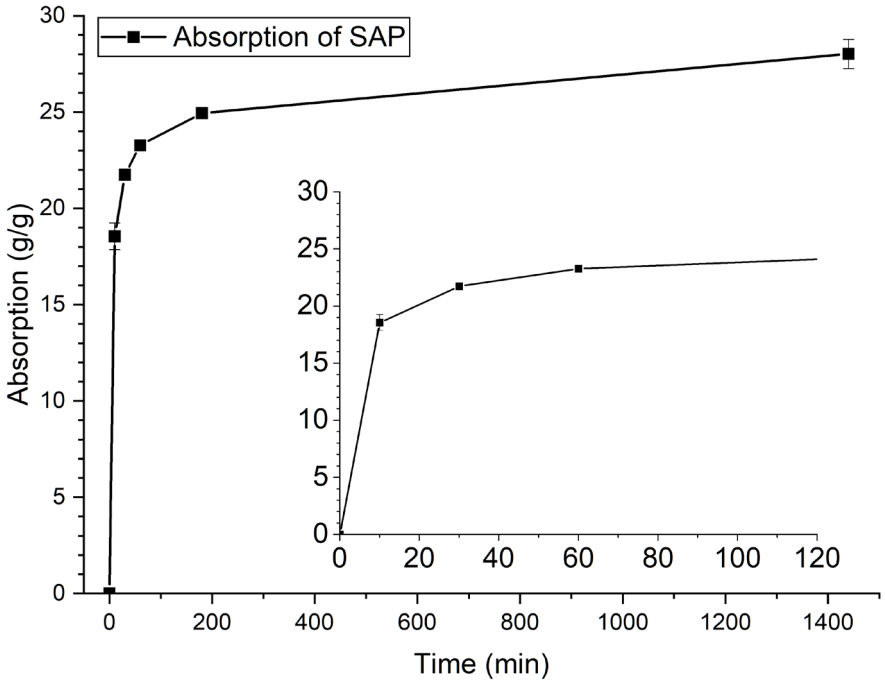

Figure 3.2.5 Absorption of SAP in the activator, measured with the teabag method

It should be pointed out that the absorption behavior of SAP in the just-mixed fresh cementitious binder is undoubtedly different from that observed from the free absorption in solution. It can be imagined that absorbing in the fresh binder is more difficult. Unfortunately, the actual absorption behavior in the fresh binder is too complicated to be simulated by experiment. In the author's perspective, all the absorption capacity tests conducted by immersing in solution are rough estimations, no matter whether the test liquid is the activator or simulated pore solution. When considering the low dosage of SAP (~ 0.3% by weight of slag), chasing for a very accurate absorption capacity for the mix design seems to be not very meaningful, especially when it comes to actual construction. For this study, an absorption capacity of 20 g/g is taken for the mix design.

3.2.1.3 Air-entraining agent (AEA)

The AEA used in this study is a commercial AEA with the brand of Hostapur OS, supplied by Clariant. The active ingredient is sodium α-olefine sulfonate (AOS), which is an anionic surfactant. According to the supplier, the AEA is designed for high pH and high Ca^{2+} environments with pronounced foam formation capability and stability.

3.2.1.4 Sodium silicate activator

The alkali activator solution is prepared by mixing the commercial sodium silicate solution, commercial sodium hydroxide solution and tap water according to designed mix proportions. The activator is prepared one day before the mixing to make sure its temperature drops back to ambient temperature.

3.2.1.5 Aggregates

The 0 – 4 mm fine aggregates used in the mixing are provided by Dekker Groep BV. The fine aggregates are dried in the oven at 105℃ for at least three days to eliminate the influence of the humidity on the mix design. Aggregates are removed from the oven and cooled to ambient temperature before mixing.

3.2.2 Mix proportions

The AASM mixtures in the study include a reference mixture without any admixture, several mixtures with the addition of SAP, and several mixtures with the addition of AEA.

3.2.2.1 Reference mixture

The reference AASM mixture is the origin of the mixtures with admixture. The reference mixture is named as **REF** and has an alkali content (Na_2O to binder ratio, N/B) of 4.29%, a modulus (SiO_2/Na_2O ratio, Ms) of 0.56, a water/binder ratio (w/b) of 0.39, and a sand ratio of 1.15. The density of the activator is tested to be 1.146 g/cm^3.

3.2.2.2 SAP mixtures

The SAP mixtures are designed based on the reference mixture. The performance of AASM with different SAP dosages, absorption compensation methods, and SAP size distributions is investigated. Mix design is based on the factor analysis, and the details are given below:

- SAP dosage:
  - 0.15% by weight of slag (BWOS)
  - 0.30% by weight of slag (BWOS)
  - 0.45% by weight of slag (BWOS)
- SAP absorption compensation:
  - Abbreviation **A**: dry SAP directly added during mixing, with the calculated additional amount of activator (20 g/g)
  - Abbreviation **P**: pre-wetting the SAP in the activator for 30 min, with the calculated additional amount of activator (20 g/g)
  - Abbreviation **N**: dry SAP directly added during mixing, no additional activator for compensating the absorption
- SAP size distribution:
  - Abbreviation **F**: sieved fine SAP particles (residue on 125 um – 250 um screen)
  - Abbreviation **C**: sieved coarse SAP particles (residue on 250 um – 500 um screen)
  - Without notes: SAP particles without sieving

The mixtures are named by their dosage, compensation method, and size distribution:

- SAP with different dosages:
  - SAP-15A, SAP-30A, SAP-45A
- SAP with different absorption compensations:
  - SAP-30A, SAP-30P, SAP-30N

- SAP with sieved size distribution:
  - SAP-30A-F, SAP-30A-C

Details are shown in Table 3.2.2 below.

Table 3.2.2 Details of mix proportions of REF and SAP mixtures

Parameters / Components	Mixtures							
	REF	SAP-15A	SAP-30A	SAP-45A	SAP-30P	SAP-30N	SAP-30A-F	SAP-45A-C
Slag (g)	1000							
Alkali content (%)	4.29							
Ms	0.56							
Fine aggregate (g)	1236							
SAP dosage (%bwos)	-	0.15	0.30	0.45	0.30	0.30	0.30	0.30
Additional activator (g)	-	30	60	90	30	0	30	30
w_{tot}/b	0.39	0.41	0.43	0.45	0.43	0.39	0.43	0.43
w_{eq}/b	0.39	0.39	0.39	0.39	0.39	0.35	0.39	0.39

3.2.2.3 AEA Mixtures

In terms of AASM with AEA, the mixtures are named in the form of **AEA-*x***, where the *x* stands for the dosage of the active ingredient AOS. For instance, AEA-010 stands for the mixture with an AOS dosage of 0.010 % by weight of slag (BWOS). An example of detailed mix designs is shown in Table 3.2.3 below.

Table 3.2.3 Details of mix proportions of REF and AEA mixtures

Parameters / Components	Mixtures			
	REF	AEA-010	AEA-020	AEA-030
Slag (g)	1000			
Alkali content	4.29%			
Ms	0.56			
Fine aggregate (g)	1236			
AEA active ingredient (% BWOS)	-	0.01	0.02	0.03
AEA active ingredient (% BWOS)	-	100	200	300
$w_{tot}/b = w_{eq}/b$	0.39			

3.2.3 Specimen preparation

The AASM specimens are prepared by mixing the slag powders, prepared activator, and dried fine aggregates for two minutes with a Hobart mortar mixer. Tests on fresh properties is then conducted. To prepare hardened specimens, the fresh mortar is cast into the mold by two layers. Compaction is done after casting each layer by a compaction table. After casting, the specimens were sealed by a plastic film and placed into a temperature control room at 20℃. After 24 hours, the specimens are demolded, sealed again, and placed back to the same room until the tests start.

3.2.4 Test methods

3.2.4.1 Workability

The workability of the fresh mortar is measured by the mini-slump test and the flow test according to EN 1015-3. A 60 mm high mini cone with a radius of 70 mm at the top and 100 mm at the bottom was used. After mixing, the fresh mortar is immediately poured into the cone in two layers. The mortar was uniformly tamped ten times after casting each layer. The excessive mortar above the cone is carefully skimmed off, and the upper surface is trowelled. Then the cone is lifted vertically, and the remaining height of the mortar is measured. Afterwards, the flow table is lifted and dropped at a frequency of 1 s^{-1} for 15 times and let the fresh mortar spread out on the disc. The diameter of the mortar is then measured in two directions at right angles to one another.

3.2.4.2 Air content

The air content in the fresh mortar of REF and AEA mixtures is determined by the pressure method following the EN 1015-7. After mixing, the fresh mortar is casted into the specific measuring vessel. Then, water is injected into the closed vessel, on the top of the mortar surface. By applying air pressure, the air in the fresh mortar is displaced by the injected water. The air content volume is then determined.

The air content in the fresh SAP mixtures is not measured because the SAP used in the study is manufactured by solution polymerization method and does not contain residue surfactant. In such case, no entrained air voids will be created before the SAP particles release the absorbed liquid, as observed in much literature [98-100]. On the other hand, the entrained air content by SAP is estimated with the measured absorption capacity. The calculation is based on the RILEM recommendation [90]. It is assumed that the volume created by the SAP is the volume of the absorption activator, and the volume of the SAP is neglected. The total air content $V_{air,\%}$ can be calculated as follows:

$$V_{air,\%} = V_{REF,\%} + V_{SAP,\%}$$
$$V_{SAP,\%} = V_{SAP} / V_{AASM} \cdot 100\%$$
$$V_{SAP} = m_{SAP} \cdot A_{SAP} / \rho_{activator}$$
$$V_{AASM} = m_{AASM} / \rho_{AASM}$$

where

$V_{air,\%}$ = estimated total air content in SAP mixture, in %

$V_{REF,\%}$ = air content of REF AASM in fresh status, measured by pressure method, in %

$V_{SAP,\%}$ = air content created by swelling and releasing of SAP, in %

V_{SAP} = air content created by swelling and releasing of SAP, in cm^3

V_{AASM} = volume of the AASM, in cm^3

m_{SAP} = mass of added SAP, in g

m_{AASM} = mass of the AASM, in cm^3

$\rho_{activator}$ = density of the activator, tested to be 1.15 g/cm^3

ρ_{AASM} = density of the REF AASM, tested to be in 2.07 g/cm^3

A_{SAP} = absorption of SAP, taken as 20 g/g

The air content in the hardened AASM is determined by micro-CT scan. A cylinder sample with a radius of approximately 1 cm is obtained from the hardened AASM by drilling. The micro-CT scan was conducted at a height of around 10 mm above the bottom. Detailed information on the post-process will be given at Chapter 4 where the entrained air system will be thoroughly investigated.

3.2.4.3 Mechanical properties

The flexural strength and compressive strength of the AASM are tested at the age of 7 days and 28 days in accordance with EN 196-1. The flexural strength is determined by three-point bending on a span of 100 mm with the 160×40×40 mm^3 specimens. Afterwards, the broke-into-half specimens from the flexural test are used to determine the compressive strength on an area of 40×40 mm^2. For each mixture, three duplicates are tested for the flexural strength while six duplicates are for compressive strength.

3.3 Results and discussions

3.3.1 Workability

The workability of the SAP mixtures is shown in Figure 3.3.1. Reference mixture REF showed good workability. All the SAP mixtures with additional activator compensation showed equal or slightly better workability than the reference mixture right after the mixing, no matter whether the SAP was directly added into the mixing in dry condition or prewetted. On the other hand, SAP-30N was the mixture without any additional activator. And it indeed showed a considerable reduction in workability due to the lower liquid/binder ratio during mixing caused by SAP absorption.

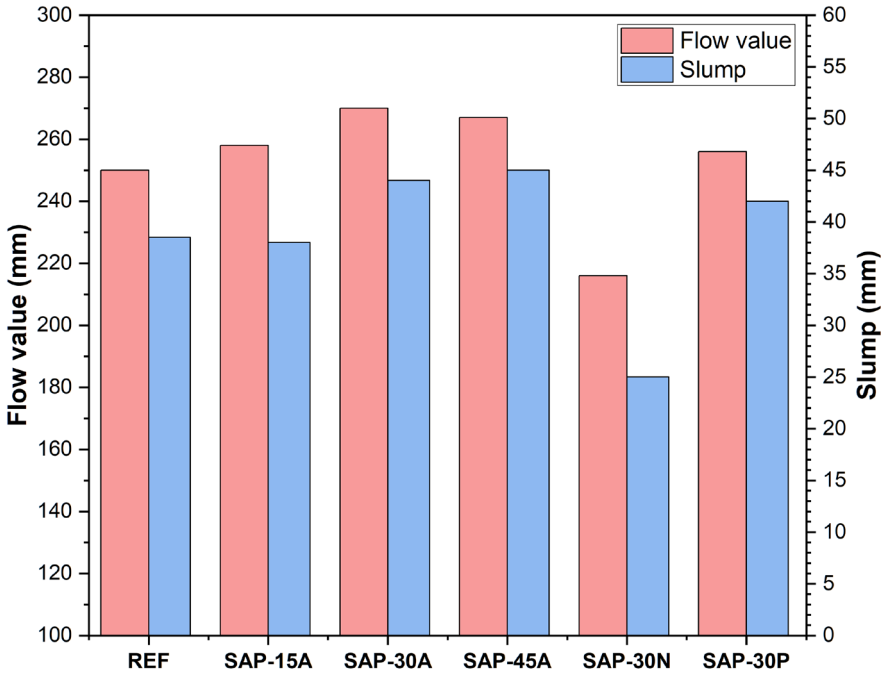

Figure 3.3.1 Slump and flow value of the REF and SAP mixtures, tested by mini-slump test and flow test

It should be emphasized that the workability was tested shortly after mixing, while the workability loss over time was not investigated. It can be imagined that the speed of losing workability will be higher when SAP is added due to continuous absorption. This faster workability loss could be a setback for SAP applications, but it also offers the potential to use SAP as an admixture to tailor the rheology properties for 3D printing. The fresh properties and rheology properties of AAS with SAP

are not the main research interest for this study, so the provided information is limited. But these are interesting and important, and further investigation is suggested.

The workability of AEA mixtures is shown in Figure 3.3.2. Because the dosage is the only variable among the AEA mixtures, the tested workability is plotted versus the dosage. It can be observed that the AEA mixtures showed similar workability with the REF, and no improvement was found. With increasing AEA dosage, the workability seems to decrease slightly. This is an interesting observation. For the investigation in OPC, it is widely agreed that AEA can improve the workability by the ball-bearing effect [84, 102, 103]. With respect to AAS, the information on the impact of AEA on workability is relatively limited. Available studies on air-entrained AASC found that AEA improves workability [69, 104, 105]. But interestingly, when it comes to mortar scale, Bílek Jr et al. [112] also found a decreased workability at high dosage AEA mixture.

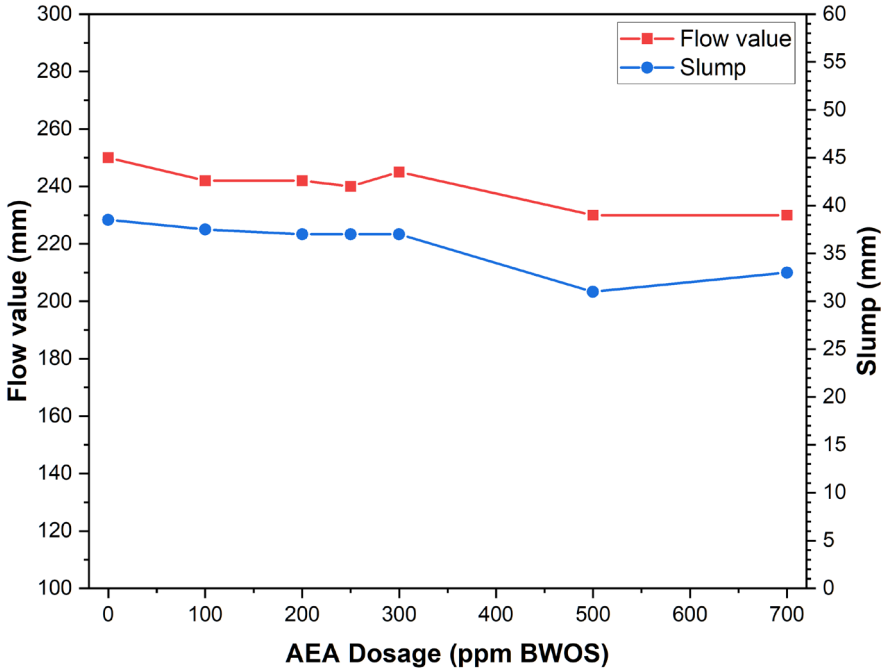

Figure 3.3.2 Slump and flow value of the REF and AEA mixtures, tested by mini-slump test and flow test

The workability results observed in this study may be due to the low sand content of the mixture. The ball-bearing effect of the entrained air bubbles mainly enhances the easiness of aggregates movement [102, 113]. In the case of a low sand ratio mortar, the extent of the ball-bearing effect might be less significant. In addition, the entrained air content in these AASMs was generally higher than that in concrete. With higher entrained air content, the liquid content in the unit volume might decrease and further reduce the flowability by increasing the yield and viscosity of the paste, as observed and explained in [113].

However, it should be pointed out that random errors can cause the unusual result. It can be seen that the difference between the results is relatively small. Because workability is not the main focus of the study, only one test was conducted. Therefore, a high random error can be expected and may be held responsible for the observed trend.

3.3.2 Air content

3.3.2.1 Air content in fresh AASM

Figure 3.3.3 shows the measured air content in the fresh mortar versus AEA dosage. The observed trend is quite typical. And it conforms to the information proved by the supplier as well as the observation from the literature [114-118]. A pretty low air content of 0.6% was measured from the reference mixture REF. With the addition of sodium α-olefine sulfonate, additional air was successfully entrained in the AASM. The air content in fresh mortar continuously increases with the increasing AEA dosage until it reaches a plateau of around 20%. This might be because surfactant concentration reaches the critical micelle concentration (CMC) [84, 115, 119]. When the surfactant is added to the fresh cementitious paste, monomers surfactants reduce the surface tension, form a layer at the interface between air and liquid, and stabilize air bubbles [84, 120]. When the dosage of AEA increases and reaches a certain point, the interface is saturated with monomers, and monomers start to self-aggregate and form micelles [85, 119]. This specific point is referred to as CMC.

In contrast to the monomer that reduces the surface tension of the liquid, further formation of micelles will not further reduce the surface tension. Therefore, when increasing the dosage, at a certain point, the surface tension reached the plateau, as well as the air content in the fresh mortar [84, 115]. The similar phenomenon can be observed in applying the superplasticizer, where the transition dosage is referred to as saturation dosage [121].

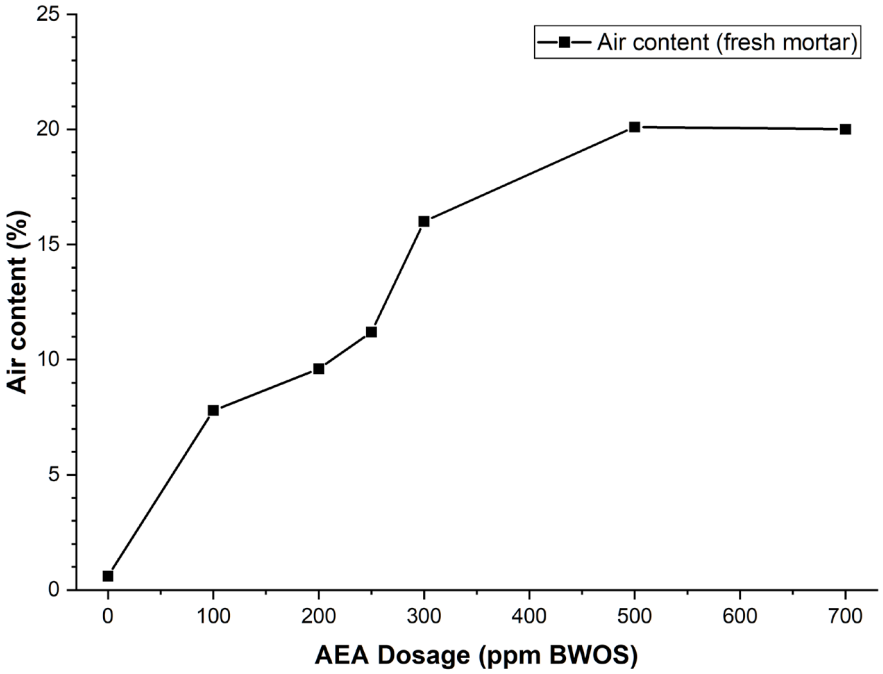

Figure 3.3.3 Air content in the fresh AASM versus AEA dosage, tested by pressure gauge method

3.3.2.2 Air content in hardened AASM

The air content in the hardened AASM is characterized by the micro-CT scan. The results are shown in Table 3.3.1. The air content in fresh AEA mixtures and the estimate air content in the SAP mixtures are also provided for comparison. Results showed that both SAP and AEA successfully entrained air voids into the AASM.

The air content difference between fresh and hardened status is relatively small for the AEA mixtures. For the SAP mixtures, it seems that the taken absorption capacity of 20 g/g is slightly

underestimated the actual absorption. For mix proportions investigated in this study, the entrained air content of AEA mixtures is generally higher than that of SAP mixtures. Nevertheless, similar air content was observed in the AEA-010 and SAP-45A, which makes it possible to compare the properties of AASM with similar air content but different admixtures. Regarding the different SAP absorption compensation methods, pre-wetting the SAP led to a higher air content of 6.6%, while drying mixing without the additional activator led to a slightly lower air content of 5.0%. The difference is attributed to the different SAP absorption behavior in different mediums. On the other hand, the particle size of SAP seems to have a minor influence on the air content, for the difference between SAP-30A-F and SAP-30A-C is only 0.2%.

The more in-depth investigation, analysis, and discussion of the entrained air system and its calculated parameters will be given in chapter 4.

Table 3.3.1 Air content in AASM tested by CT scanning

Air content (%)											
	REF	**AEA -010**	**AEA -020**	**AEA -030**	**SAP -15A**	**SAP -30A**	**SAP -45A**	**SAP -30P**	**SAP -30N**	**SAP -30A-F**	**SAP -30A-C**
Hardened	0.7	7.1	9.5	14.8	2.5	5.5	7.2	6.6	5.0	5.7	5.5
Fresh/Est.	0.6	7.8	9.5	16.0	2.6	4.5	6.6				

3.3.3 Compressive strength

3.3.3.1 Overview

To give a general idea of the extent of reduction, Figure 3.3.4 summrizes the compressive strength of all mixtures at 7 days and 28 days. The factor analysis will be conducted in the following sections. Among all the mixtures, the highest compressive strength was observed from the reference mixture REF, being 43.8 MPa at 7 days and 54.7 MPa at 28 days. In other words, the addition of SAP/AEA indeed gave a certain loss of compressive strength on the AASM. Such a loss in compressive strength is attributed to the higher porosity in the AASM due to the entrained air voids.

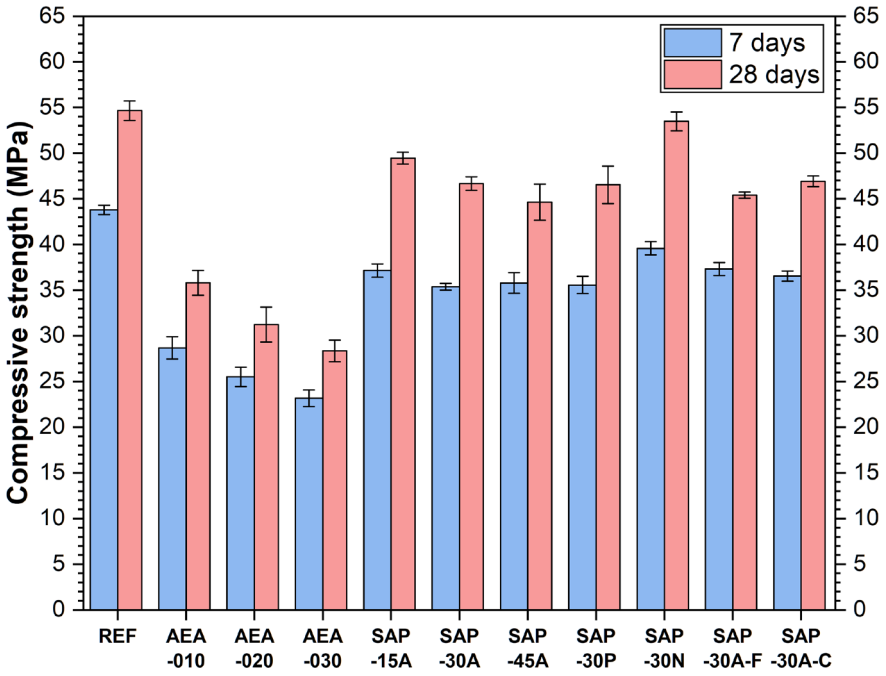

Figure 3.3.4 Compressive strength of all the mixtures at 7 days and 28 days

Comparing the AEA mixtures and SAP mixtures, it can be clearly observed that the compressive strength reduction in AEA mixtures is considerably higher than that of the SAP mixtures. This observation conforms to the literature [90, 100, 122]. The smaller reduction in SAP mixtures might be due to the benefit of the internal curing provided by SAP. After 7 days, the SAP still contains a certain amount of absorbed activator [91]. The remaining additional activator continuously releases and leads to a later reaction. With the internal curing, the degree of reaction is increased and the higher amount of reaction product densifies the matrix and compensates for the loss caused by the higher porosity. To have a more straightforward impression, the increment of compressive strength from 7 days to 28 days is calculated and shown in Table 3.3.2. For REF, the compressive strength increment from day 7 to day 28 was 24.8%. For the SAP mixtures, most of the mixtures exhibited a higher increment. On the contrary, AEA does not have such an effect. Therefore, as shown in Table 3.3.2, the strength increment of AEA mixtures was very similar to the one of REF. In addition, it is noticed that SAP-30A-F, which has the sieved fine SAP particles, had the lowest strength increment. This might be attributed to the higher surface area of the fine SAP particle, making it more difficult to retain absorbed liquid, and the internal curing ended earlier.

Table 3.3.2 Strength increment of the AASM mixtures, from 7 days to 28 days

Mixtures	REF	AEA -010	AEA -020	AEA -030	SAP -15A	SAP -30A	SAP -45A	SAP -30P	SAP -30N	SAP -30A-F	SAP -30A-C
Increment	24.8%	24.8%	22.4%	22.4%	33.1%	32.0%	24.8%	30.8%	35.1%	21.7%	28.4%

3.3.3.2 AEA mixtures

The 28 days compressive strength as well as the air content of the AEA mixtures are shown in Figure 3.3.5. The compressive strength loss (compared to REF) at 28 days versus the air content in fresh AASM is shown in Figure 3.3.6.

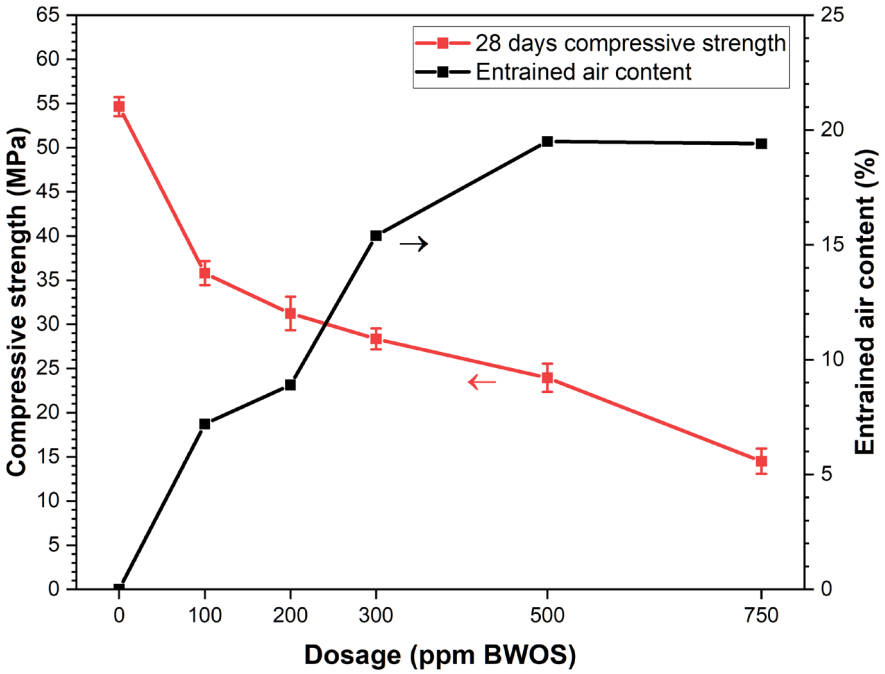

Figure 3.3.5 Compressive strength and entrained air content of the air-entraining AASM versus the AEA dosage at 28 days

The addition of AEA induced considerable loss in compressive strength. 34.5% strength reduction was observed at 28 days on the AEA-010, which has the lowest AEA dosage in this study. The compressive strength continuously decreases with increasing dosage, as shown in Figure 3.3.5. The remanent compressive strength of AEA-075 is only around 15 MPa.

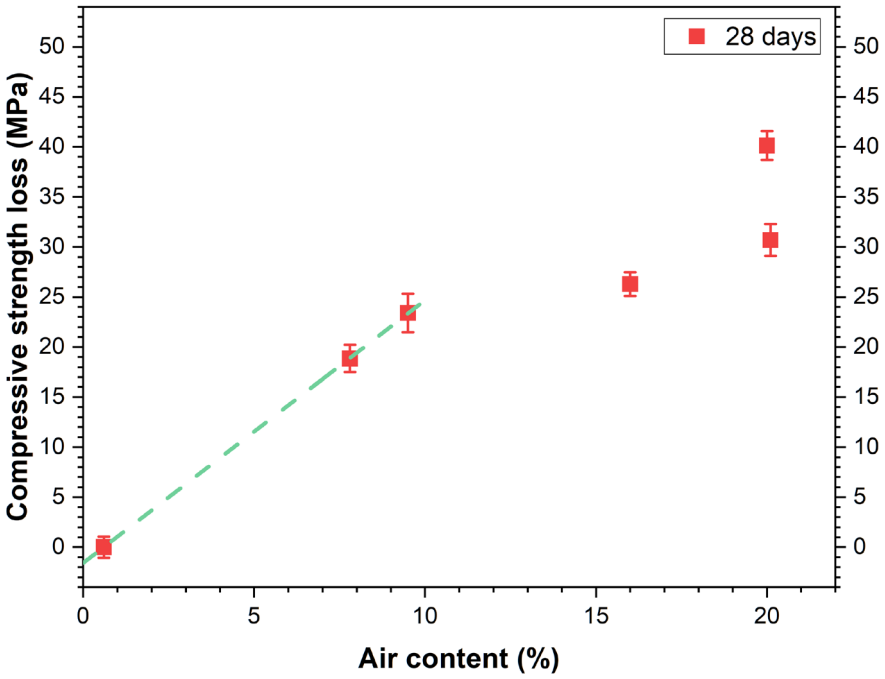

Figure 3.3.6 Compressive strength loss of the air entraining AASM at 28 days versus the air content tested by pressure method, where trend line was drawn for the mixtures with air content lower than 10%

The reduction in compressive strength increases with increasing air content, as shown in Figure 3.3.6. Interestingly, for the AEA-050 and AEA-075, no increment in the air content was found due to

the CMC, as mentioned above. However, the compressive strength continuously decreased. Relative information is minimal in the literature because the dosage of 750 ppm is quite above the usual dosage, and the compatibility of AEA in AAS binder is scarcely studied. The cause behind might be attributed to a circumstance that a considerable amount of surfactants adsorb on the surface of the binder particles and hinder the reaction, as suggested by [118]. The mechanism behind this phenomenon and how the different types of AEA influence the reaction of AAMs are interesting topics and worth further study. Unfortunately, these are beyond the scope of this study. Nevertheless, it can be concluded that an excessive amount of AEA is undesirable.

The common entrained air content of concrete is below 10%. Therefore, the compressive strength reduction versus the air content among mixtures REF, AEA-010, and AEA-020 is further studied. It can be observed that the trend is generally linear within this air content range, as indicated by the green line. For each 1% increment in entrained air content, around 4.8% strength reduction was found. Therefore, the thumb rule from OPC mentioned above [109] is still applicable to AAS when the air content is in the common range.

3.3.3.3 SAP mixtures

Figure 3.3.7 shows the 7 days and 28 days compressive strength of the SAP samples, grouped by the investigated variable.

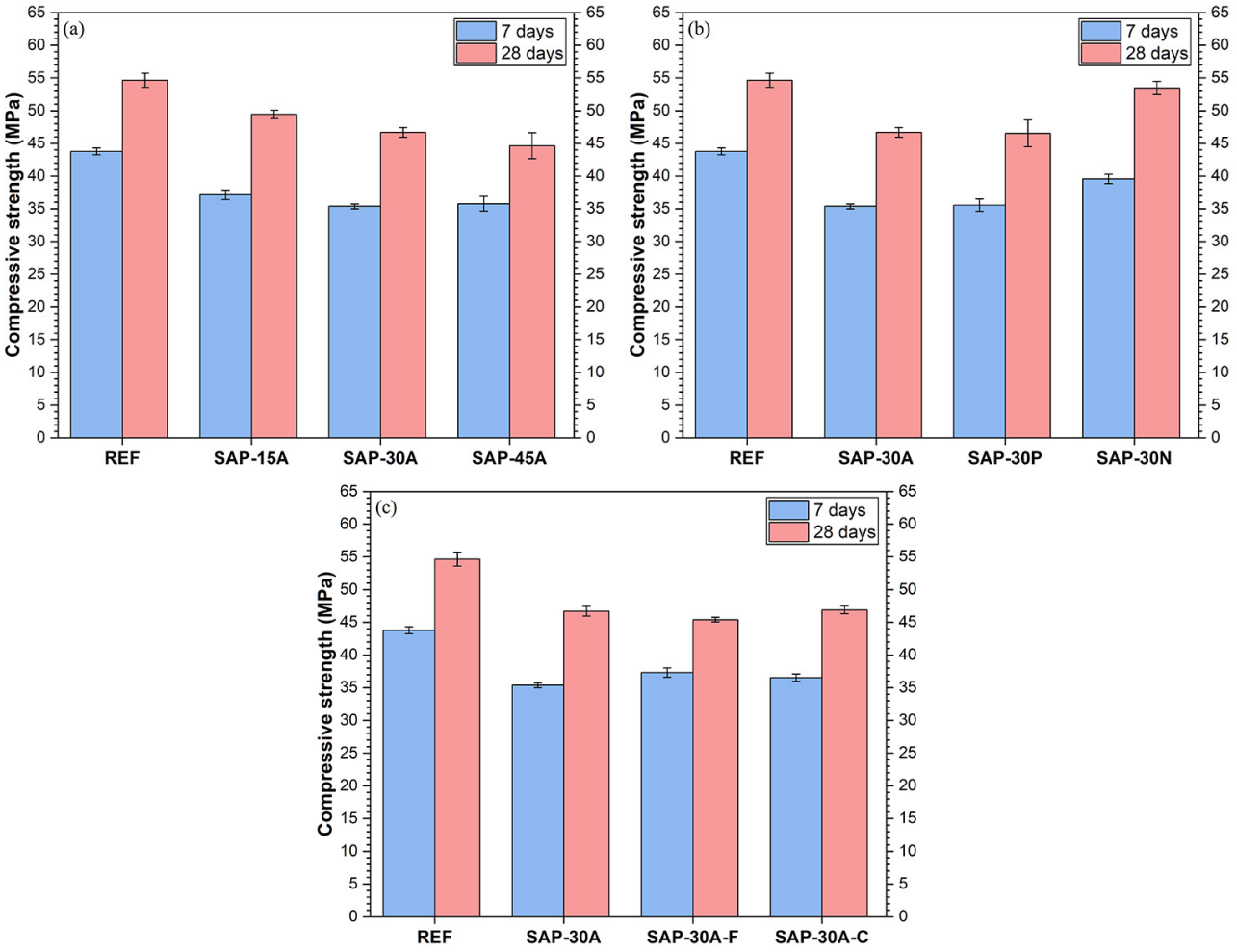

Figure 3.3.7 Compressive strength of REF as well as SAP mixtures with different (a) dosage; (b) absorption compensation method; (c) SAP particle size distribution at 7 days and 28 days

Figure 3.3.7 (a) shows the effect of SAP dosage on compressive strength. The compressive strength decreases linearly with the increasing dosage. 18% strength reduction was found in the SAP-45A. As mentioned in section 3.3.2, mixture AEA-010 has very close air content, but the compressive strength reduction is 35%. Therefore, it can be concluded that the strength reduction caused by SAP is considerably lower under similar entrained air content.

Figure 3.3.7 (b) shows the compressive strength of AASM with different SAP absorption compensation methods. SAP-30N has no additional activator and exhibited considerably higher compressive strength than the other two, as high as that of REF (54.65 MPa vs. 53.48 MPa at 28 days). Such a low reduction is attributed to a lower equivalent water/binder ratio caused by the absorption of SAP. SAP-30A and SAP-30P both have the extra activator to compensate for the absorption. The former is dry mixing SAP, while the latter is pre-wetting SAP. Their resultant 7-day and 28-day compressive strength were very similar. These observations indicate that the equivalent water/binder ratio is much more significant to the compressive strength than the saturation condition of SAP at mixing.

Figure 3.3.7 (c) shows the mixtures with SAP of different particle size distributions. Similar compressive strength was found among the mixtures. Therefore, it seems that the influence of SAP particle size on compressive strength is neglectable. However, a more significant difference might be observed if the SAP dosage differs.

An interesting detail is that higher relative error was found in the compressive strength of SAP-45A and SAP-30P, both on the 7 days compressive strength and 28 days compressive strength. The higher scatter implies that some other factors of high randomness might be introduced in the performance. This high randomness factor might be the aggregation of SAP particles in this case. As can be imagined, SAP particles aggregation is more likely to happen when the dosage is high, or the SAP is prewetting in solution.

3.3.4 Flexural strength

Figure 3.3.8 shows the flexural strength results of all the mixtures.

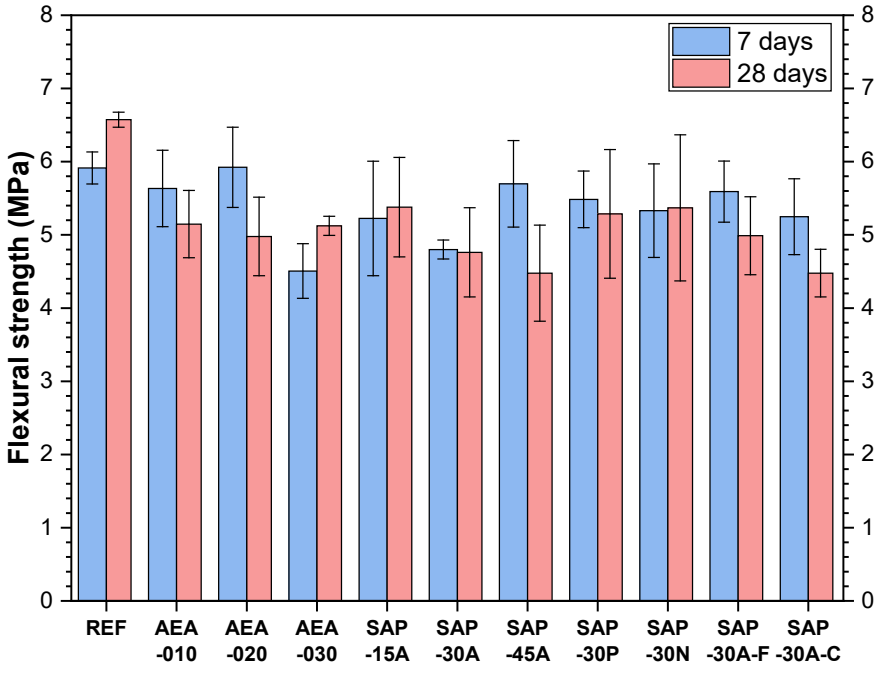

Figure 3.3.8 Flexural strength of all the mixtures at 7 days and 28 days

A lower flexural strength was found in the mixtures with AEA and SAP due to the higher porosity. All the mixtures with admixture showed similar performance, and the reduction is around 20% - 30%. In addition, the relative error was also considerably high compared to the compressive strength deviation. This is probably due to the flexural strength being more sensitive to many factors of high randomnesses, such as surface cracking, bleeding, segregation, etc. It is also noticed that mixtures showed minimal increment or even slight decrement in flexural strength from 7 days to 28 days. This could be due to the competition among the higher degree of reaction, surface cracking caused by autogenous shrinkage, and surface cracking caused by drying due to imperfect sealing, as shown in chapter 5 later.

The high relative error makes it difficult to predict the trends caused by variables. Nevertheless, based on the 28 days flexural strength, it seems that:

- AEA dosage seems to have a minor influence on flexural strength,
- With higher SAP dosage, the reduction is higher,
- SAP absorption compensation methods seem to have minimal influence,
- Finer SAP particles give higher flexural strength.

Still, it is difficult to draw a solid conclusion and explanation with the high relative error and limited data. Further investigation can be conducted in the future if necessary.

3.4 Observations and conclusions

In this chapter, the workability, air content, and mechanical properties of AASM with or without the addition of SAP and AEA are investigated by the mini-slump test, flow test, pressure method, CT scanning, compression test, and three-point bending test.

For workability, applying SAP with additional activator and applying AEA have a minor influence on the slump and flowability. Applying SAP without additional activator to compensate for its absorption leads to a considerable loss in workability. The workability reduction speed of AASM was not investigated, but further investigation on the fresh properties and rheology properties of AAS with SAP is suggested.

For the air content of the AASM, both SAP and AEA successfully entrained additional air. With increasing SAP/AEA dosage, the entrained air content increase. Pre-wetting the SAP is likely to create a higher air content, while the influence of SAP particle size on air content seems to be minimal.

For the compressive strength, both SAP and AEA led to a certain extent of strength reduction. The strength reduction caused by adding SAP was considerably smaller than by adding AEA, as a result of internal curing. With similar entrained air content of about 7 %, the strength reduction caused by AEA is twice of SAP. For the AEA mixtures, in the range of common air entrainment ($\leq$ 10%), the compressive strength linearly decreases with increasing air content, at a 4.8% reduction in compressive strength for each 1% increment in entrained air content. For the SAP mixture, minor strength loss (0 - 20%) was found. And the difference caused by different dosages, absorption compensation methods, and particle size distributions seems relatively small.

For the flexural strength, both AEA and SAP cause similar moderate strength loss at 20 - 30 %. The difference between different mixtures is small, and a high relative error was found in all mixtures. Thus, it is difficult to make a solid conclusion based on limited available data.

Generally speaking, based on the test results, it can be found that the performance of AASM with SAP is less sensitive to the variable (e.g., dosage, mixing method, etc.) than AASM with AEA. From the quality control perspective, it is well known that traditional air training concrete must be carefully produced and treated. The mechanical properties and the entrained air system are very sensitive to factors like dosage, environment, construction procedure, and labor quality. In contrast, when SAP is used, the sensitivity of the resultant properties to these variables and uncertainties is low. Compared to laboratory work, the construction in reality involves much more uncertainties. With SAP, the higher tolerance to varieties and uncertainties as well as the robustness of engineering performance is a valuable merit for the industrial application.

The general properties of AASM studied in this chapter are important for structural design and construction. Such crucial factors always need to be examined and guaranteed first; otherwise, the finding will never reach the actual applications.

4 The air-void system of AASM with or without SAP / AEA

4.1 Introduction

In concrete/mortar/paste, air voids with a radius larger than 0.01 mm are usually regarded as large air voids. These large air voids can be created by entrapped air or admixtures such as SAP and AEA. The combination of these air voids is referred to as the air-void system when it comes to freeze-thaw durability. In terms of freeze-thaw resistance, a desirable air-void system consists of plentiful, tiny, uniformly distributed air voids. During the freeze-thaw cycles, these air voids can limit the generated pressure due to the expansion of water freezing. Several parameters have been proposed to quantitively describe an air-void system, such as air content, spacing factor, air-void size distribution, etc.

The air-void system can be characterized with the ASTM C457, where the linear-traverse and modified point-count methods are described. These two methods are widely used because of their simplicity and low equipment requirements. However, a crucial premise of these methods is that the air voids are spherical. This premise is naturally satisfied when the AEA is used to generate air bubbles. However, when SAP is used to conduct air voids entraining, the shape of the air voids is identical to the shape of the original SAP. For mass-producing SAP, the solution polymerization method is usually used. The resultant SAP of solution polymerization is irregular, and so do its resultant air voids. In such a case, the linear-traverse method can only provide a very rough estimation.

The computed tomography scan (CT scan) is also capable to characterize the air-void system. It is an elaborate and precise method, but much more expensive for the need of costly equipment. CT scan was originally developed for medical application [123]. Later, it was used in many areas because of its versatility. The resolution of the traditional CT scan is at a millimeter level. This resolution is good enough to provide information for clinical use, but way too low for many scientific research, such as material science. Therefore, for the application in such areas, micro-CT was developed for scanning a small object with a much higher resolution [124-126]. Depending on the equipment and size of the sample, the resolution of a micro-CT scan can easily reach micron meter level or even higher [124, 126, 127]. The micro-CT scan has an identical objective and principle to the traditional CT-scanning, i.e., 3D non-destructive imaging based on the different X-ray attenuation of different materials. When X-ray passes through materials, there is a reduction in its intensity because some of the photons are absorbed by the materials. The extent of reduction is correlated to the linear attenuation coefficient (LAC), which is related to the characteristic of the material itself. Therefore, by studying the extent of attenuation, it is able to differentiate the different materials in the sample. A schematic of the mini-CT scan is shown in Figure 4.1.1. The characterized sample is placed in the middle on a rotation table, which rotates during the scanning. On one side, a micro-focus X-ray tube generates the X-ray. On the opposite side, there is an X-ray detector. During the scanning, the X-ray generated by the X-ray tube passes through the sample and attenuates. Then, the transmitted photons are detected by the detector in the opposite, and a 2D attenuation map is generated. By rotating the sample, a series of 2D attenuation maps are generated, and the 3D imagining can be generated by computational reconstruction.

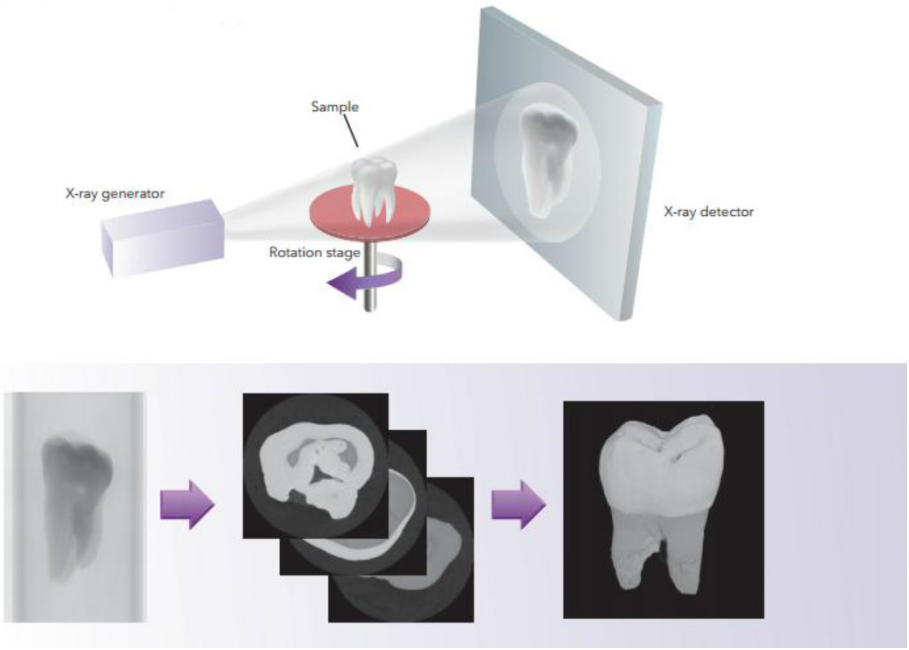

Figure 4.1.1 Schematic of micro-CT scan, setup, and principle. Adapted from [128]

When it comes to the characterization of the air-void system in cementitious materials, the micro-CT scan is applicable to reconstruct the whole air-void system in the sample. Because the air in air voids has a much lower LAC due to the low density, the pixels belonging to air voids can be easily differentiated from the solids such as paste and aggregates. More specifically, they have a quite different grey level on the attenuation maps. With the 3D imaging data, visualization and characterization of the air-void system can be done by image processing.

Micro-CT scan is not widely used in the characterization of the air-void system. One of the reasons is expensive. Another reason is scanning resolution decreases with the increase in the size of the sample. It is not feasible to conduct the micro-CT scan on a volume-representative concrete sample to characterize its micro-level air-void system. Fortunately, it is possible to conduct the micro-CT scan in this study because the samples are mortar scale. In this case, the resolution of the scanning is relatively acceptable. Accordingly, this chapter aims to characterize the air-void system of AASM with or without SAP/AEA by micro-CT scan.

4.2 Materials and methods

4.2.1 Materials and mix proportions

The raw materials characterized in Section 3.2.1 will be used in this section. The mix designs for the reference mixture and SAP mixtures in this chapter will be the same as those described in chapter two. In terms of the AEA mixtures, the dosage of 0.01%, 0.02%, and 0.03% BWOS will be used. To summarize, there are:

- Reference:
  - REF
- SAP with different dosages:
  - SAP-15A, SAP-30A, SAP-45A
- SAP with different absorption compensations:

  - SAP-30A, SAP-30P, SAP-30N
- SAP with different sieved size distributions:
  - SAP-30A-F, SAP-30A-C
- AEA with different dosages:
  - AEA-010, AEA-020, AEA-030

The curing regime of the samples is identical to the procedure of the freeze-thaw test. After mixing, the fresh mortar is cast into a 160×40×40 mm^3 prism mold. After demolding, the specimens follow the same sample preparation and preconditioning procedure in the freeze-thaw test: sealed and cured under 20°C until day 14 and bought to surface drying at 55 RH% for 14 days. Then, a cylinder sample of approximately 1 cm diameter is taken from the prism specimen by drilling. Water is used during the drilling to cool down the blade. The influence of absorbed water on air-void system characterization is neglectable because the difference in the X-ray attenuation between the water and solid phase is still significant. Afterwards, the samples are bought to micro-CT scan.

4.2.2 Air-void system characterization

The air-void system of AASM with or without SAP/AEA is characterized by the micro-CT scan with Phoenix Nanotom. Figure 4.2.1 shows the brief procedure. Cylinder samples with a diameter of approximately 10 mm and a height of 40 mm are fixed on the rotation table for scanning. The central portion of the sample is scanned, with a height of 13.80 mm. After the micro-CT scan, a series of 13.70×13.70 mm^2 horizontal slice images are generated, with a resolution of 6 um per pixel. The step between adjacent slices in the height direction is 6 um, and approximately 2300 micro-CT slices are generated for each mixture. After the micro-CT scan, the air-void system is reconstructed and characterized in MATLAB by previously developed scripts (private communication with Dr. Hua Dong).

A cubic of 7.80×7.80×7.80 mm^3 (1300×1300×1300 voxels) is taken from the sample and used for investigating the air-void system, as indicated in Figure 4.2.1. Only studying a portion of the scanned sample is with the consideration of 1) the limitation of computer computing power; 2) the brightness of the hundreds of slices at the edge is too dark or too bright to analysis; 3) the sample is not perfectly vertical, taking a larger portion might include some space outside the sample.

The slices from the micro-CT scan are greyscaled, as shown in Figure 4.2.1. Difference materials have different X-ray attenuation characteristics and therefore exhibit different grey levels. The air in the air voids and surrounding ambient environment have the lowest X-ray attenuation, and the grey level is closer to 0 (i.e., in black). The paste and aggregate have a quite close X-ray attenuation and cannot be reliably differentiated. Therefore, they are referred to as the solid phase. The X-ray attenuation of the solid phase is considerably higher than air, and its grey level is higher (i.e., brighter). The air voids are differentiated from the solids by image processing in MATLAB. First, the investigated portion of the sample is converted to a three-dimensional array consisting of 1300×1300×1300 voxels by assigning the grey level of every pixel to its corresponding voxel. Then, the materials in the investigated portion, in the form of voxels, are distinguished as air voids or solids. This is done by thresholding. The three-dimensional array is then binarized by setting a threshold. In such a way, the program identified the air voids and solid phases. The array is further optimized by post-processing, such as infilling and noise canceling. After these steps, the reconstruction of the air-void system is finished, as shown in the visualization in Figure 4.2.1.

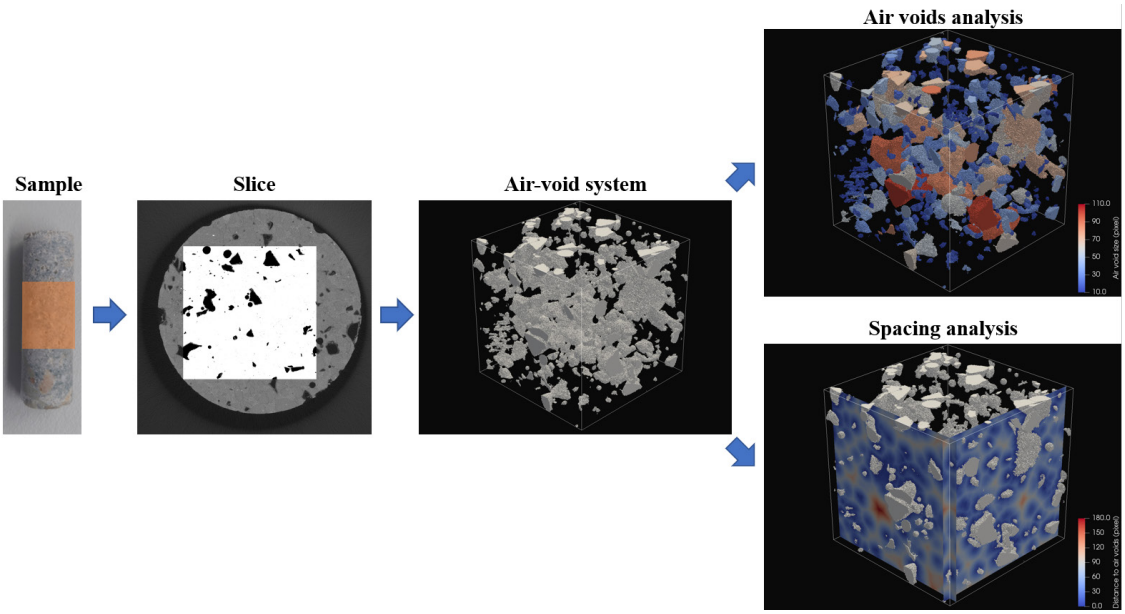

Figure 4.2.1 Procedure of characterization of the air-void system by micro-CT scan

Several algorithms are used to characterize the air-voids system, and the air-voids system parameters are calculated. First, the volume of every air void V_i is calculated by an algorithm counting all the connected voxels. The total air content of the sample in % is calculated by dividing the total volume of the air voids by the whole volume V_{total} (i.e., 1300×1300×1300 voxels or 7.80×7.80×7.80 mm^3):

$$air\ content = \sum V_i / V_{\text{total}}$$

The size of air voids is characterized by air void equivalent radius r_{eq}. It is calculated by calculating the radius of the equivalent sphere that has the identical volume:

$$r_{\text{eq},i} = \sqrt[3]{3 \cdot V_i / 4\pi}$$

Lastly, the spacing of the air voids is characterized by the parameter named flow distance, which is slightly different from the traditional method.

The traditional linear-traverse method uses the concept of spacing factor to evaluate the spacing of the air voids. The spacing factor stands for the maximum distance that water in the paste would have to travel to reach an air void [37, 82]. It is calculated based on a hypothetical system[37, 82]. The total volume of paste and air in the concrete is divided into hypothetical cubes by the number of air voids. The air in the concrete is divided into hypothetical spheres of equal size, and each sphere locates at the central of a hypothetical cube. The spacing factor is calculated by deducting the radius of the hypothetical sphere from the half-diagonal of the hypothetical cube.

In this study, the spacing of the air voids is evaluated by a similar starting point but more straightforward. Based on the reconstructed air-void system, the distance of every solid phase voxel to the closest air voids is calculated by an algorithm. To distinguish, this distance is referred to as flow distance. By this method, the spacing of the air voids can be evaluated by the value distribution and mapping of the flow distance, as shown in Figure 4.2.1. Unfortunately, the difference in grey level between the paste and aggregate is too small to differentiate. Therefore, the flow distance of the voxel that represents the aggregate is also included. The flow distance map is calculated on the 1000×1000×1000 voxels cube located at the center of the reconstructed sample to reduce the boundary's effect, which might lead to an overestimation of the flow distance of the voxels near the boundary.

4.3 Results and discussions

4.3.1 General observation

Figure 4.3.1 shows the typical slice of the AASM with or without SAP/AEA, achieved by the micro-CT scan. Figure 4.3.2 shows the 3D visualization of the air-void system of the mixture REF, SAP-15A, and AEA-010, with the mapping of the size of air voids. It can be seen that both SAP and AEA successfully entrained air voids into the hardened AASM. REF mixture showed dense microstructure and low porosity. Only some entrapped air bubbles can be found. SAP and AEA showed quite different air-voids systems, as seen in Figure 4.3.1 (b) (c) and 4.3.2 (b) (c). The air voids created by SAP were big and irregular voids, while the air voids entrained by AEA were tiny sphere bubbles.

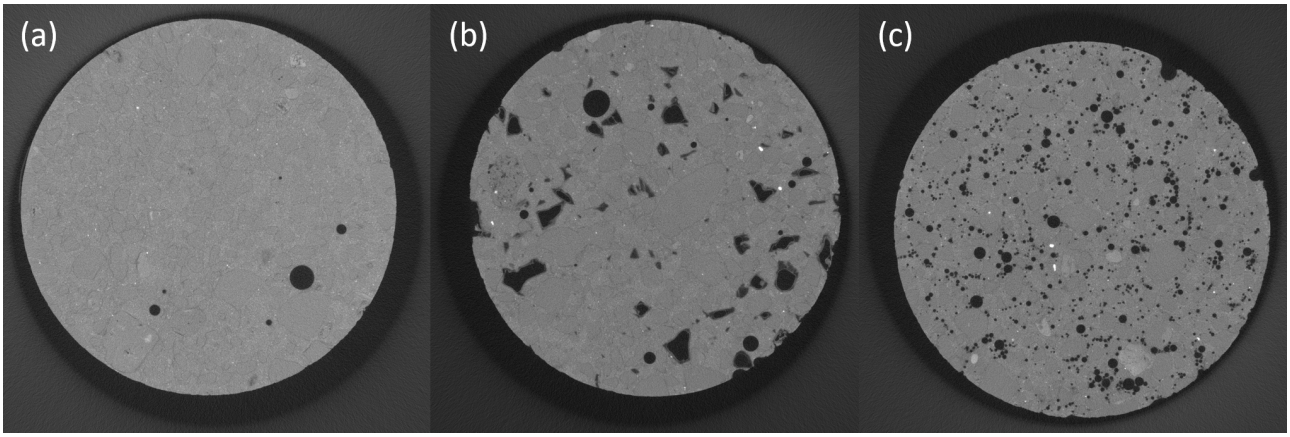

Figure 4.3.1 Typical micro-CT scan slice of (a) REF; (b) SAP mixture; (c) AEA mixture.

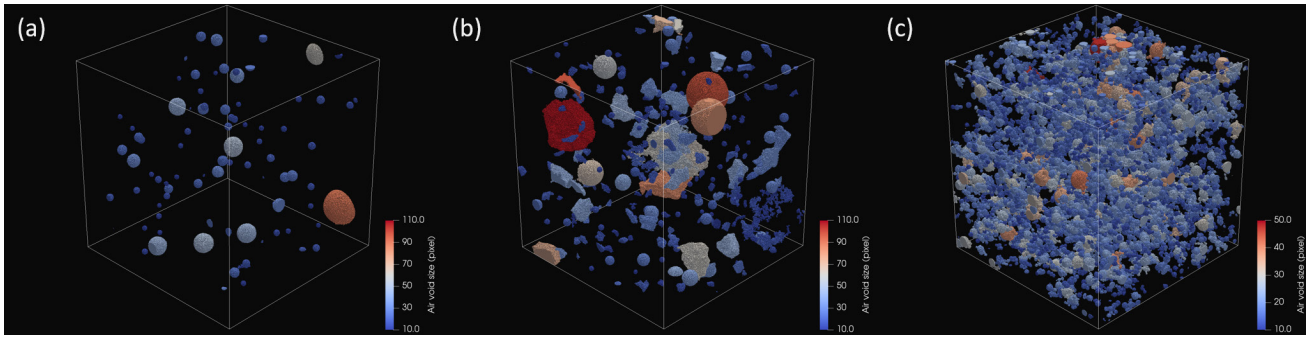

Figure 4.3.2 3D visualization of the air-void system in the samples (a) REF; (b) SAP-15A; (c) AEA-010, with mapping of the equivalent radius r_{eq} of air voids. Noticed that the scale range of the AEA- 010 is different from the other two

4.3.2 Air-void system and its parameters

4.3.2.1 AASM with different SAP dosages

Figure 4.3.3 shows the visualization of the air-void systems of AASM samples with different SAP dosages. Figure 4.3.4 shows the curve of cumulated air content in relation to the air void equivalent radius r_{eq}. The y-value at the end of the curve indicates the total air content in that AASM. It can be clearly observed from Figures 4.3.3 and 4.3.4 that with a higher SAP dosage, the air content in the AASM was higher due to the more entrained air voids in the AASM.

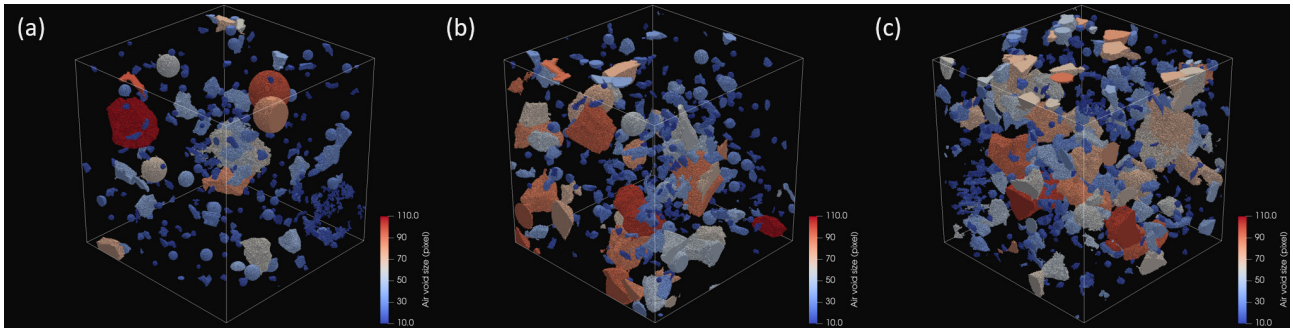

Figure 4.3.3 Visualization of the air-void systems of AASM samples with different SAP dosages: (a) SAP-15A; (b) SAP-30A; (c) SAP-45A. Plotted with mapping the air void equivalent radius with color, noticed that 1 pixel =6 um

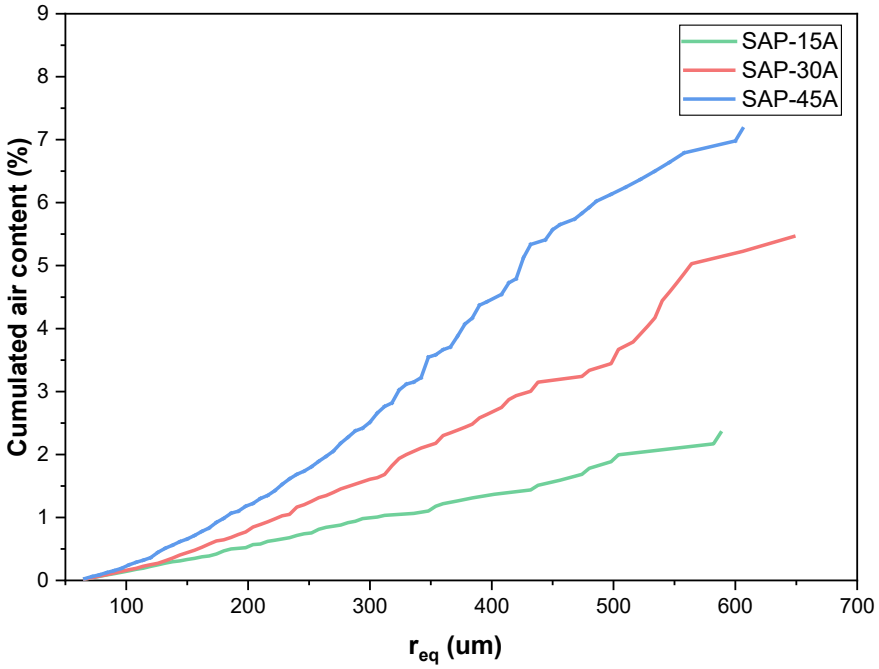

Figure 4.3.4 Relation between the cumulative air content and the air void equivalent radius of AASM samples with different SAP dosages

For all the mixtures, the range of the air void equivalent radius was up to around 600 um. Therefore, it seems that the SAP dosage has a minor influence on the air voids size distribution in general. The air voids size distribution is then further analyzed. The number of air voids in a certain size range was normalized by the total number of air voids, and the stacking chart was plotted in Figure 4.3.5. Results show that the size distribution of the air voids slightly became larger with higher dosage. Such a trend can also be observed in Figure 4.3.3. This can be attributed to two reasons. One is the higher tendency of SAP particle aggregation at higher SAP dosage. Second is the higher portion of irrelative noises (which are small) in lower SAP dosage: noises always exist in the result and are recognized as small SAP. With a higher amount of SAP, the portion of the noise is relatively smaller and leads to the air void size distribution becoming larger.

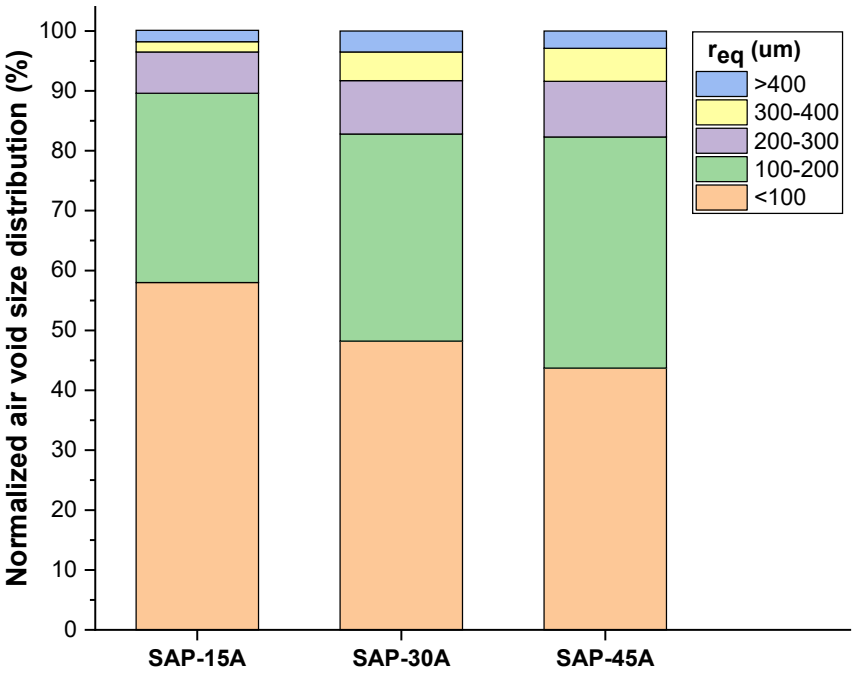

Figure 4.3.5 Air voids size distribution of AASM samples with different SAP dosages, normalized by the total amount of air voids

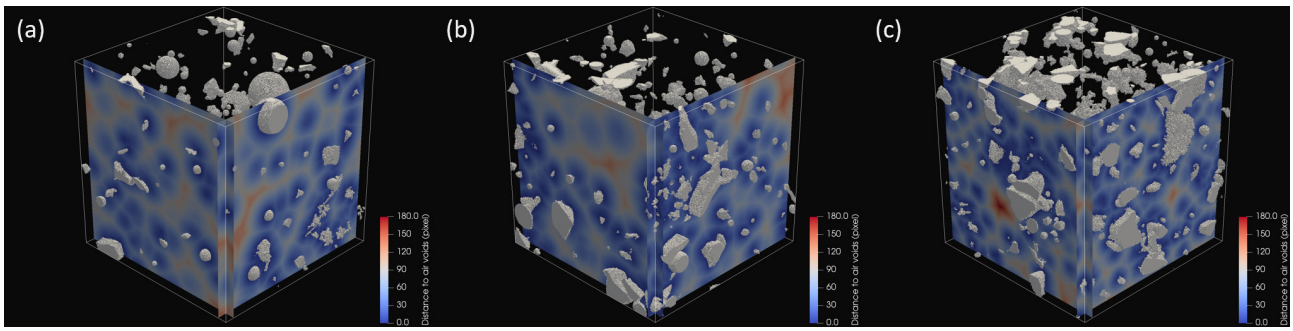

Figure 4.3.6 Visualization of the flow distance of AASM samples with different SAP dosages: (a) SAP-15A; (b) SAP-30A; (c) SAP-45A. Plotted with mapping the air void equivalent radius with color, noticed that 1 pixel =6 um

Figure 4.3.6 shows the visualization flow distance map. The air void spacing was evaluated by calculating the flow distance. Two slices were made for illustration, and the flow distance of each voxel on the matrix was calculated and mapped by color. With the higher flow distance, the color at the voxel gradually turned from blue to red.

Figures 4.3.7 (a) show the cumulated portion of the matrix that has a flow distance below a certain value; Figure 4.3.7 (b) shows the increment of the portion at a certain flow distance. Two horizontal lines are made in order to indicate the value of d_{50} and d_{90}, i.e., 50% or 90% of water in the solid phase has a flow distance below this value.

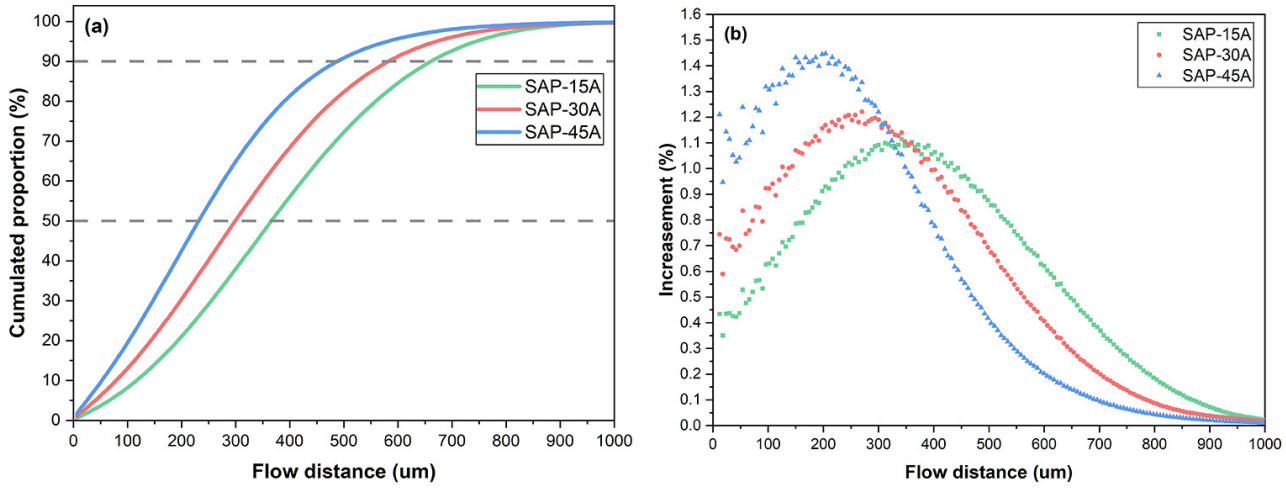

Figure 4.3.7 (a) Cumulated matrix portion and (b) portion increment of AASM samples with different SAP dosages versus the flow distance

It can be noticed that both the cumulated curve and increment curve shifted to the left with a higher SAP dosage, meaning that the air voids were closer distributed and the flow distance was smaller. Higher SAP dosage led to more entrained air voids in the AASM and a closer distribution of air voids. With closer air voids spacing, the water in the matrix has a shorter travel distance to the closest air voids, i.e., a smaller flow distance. The d_{50} and d_{90} of AASM reduced from 366 and 660 um to 234 and 486 um when increasing the SAP dosage from 0.15% to 0.45% BWOS, respectively.

4.3.2.2 AASM with different SAP absorption compensation methods

The visualization of air-void systems of SAP-30A, SAP-30P, and SAP-30N is shown in Figure 4.3.8. The varying factor among these samples is the SAP absorption compensation method, which has been detailly discussed in Section 3.2. Figure 4.3.9 shows the cumulated air content in AASM in relation to the air void equivalent radius. These three mixtures generally showed relatively similar entrained air content and air void size distribution. The air content in the SAP pre-wetting mixture SAP-30P is 6.5%, which is slightly higher than the air content of the other two mixtures. This is because the absorption of SAP particles was more freely in solution than in fresh cementitious materials paste.

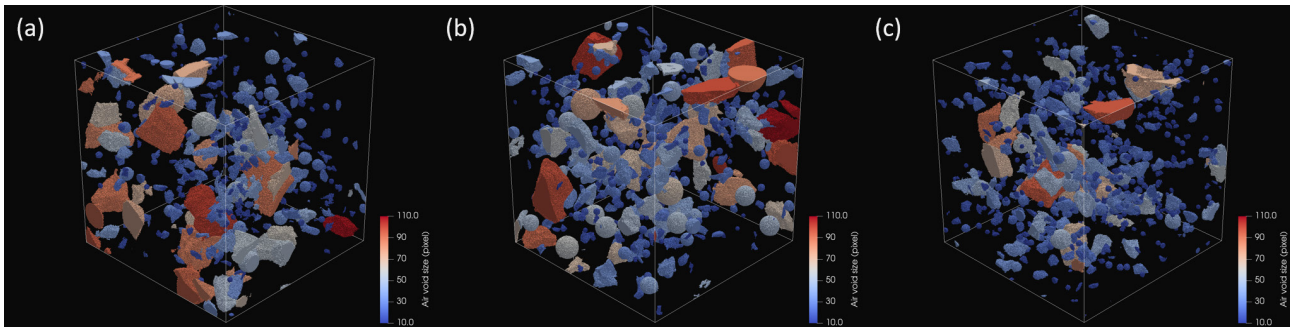

Figure 4.3.8 Visualization of the air-void systems of AASM samples with different SAP absorption compensation methods: (a) SAP-30A; (b) SAP-30P; (c) SAP-30N. Plotted with mapping the air void equivalent radius with color, noticed that 1 pixel =6 um

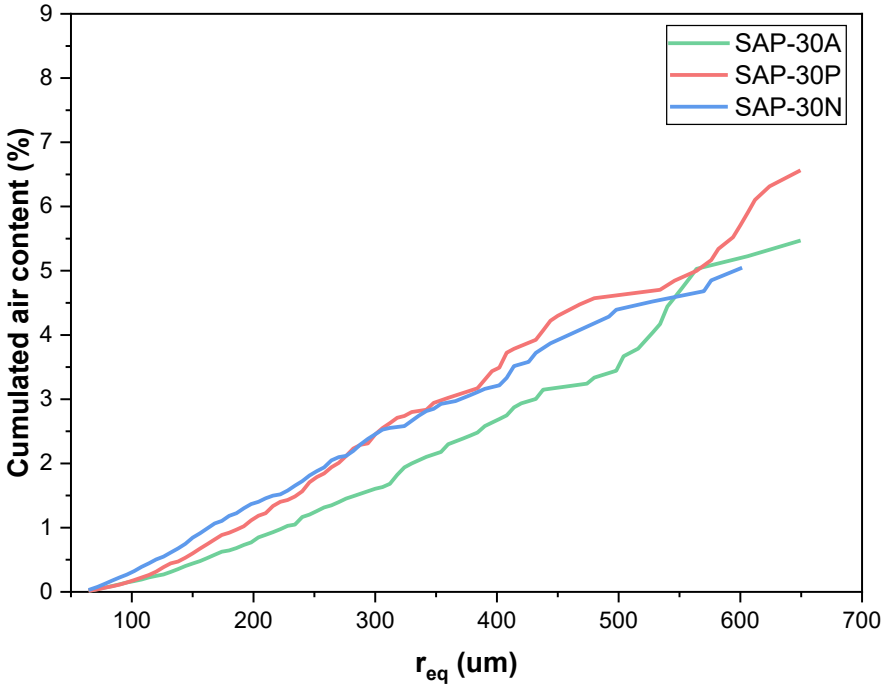

Figure 4.3.9 Relation between the cumulative air content and the air void equivalent radius of AASM samples with different SAP absorption compensation methods

Air voids size distributions normalized by the total number of air voids of mixture SAP-30A, SAP-30P, and SAP-30N are shown in Figure 4.3.10. Compared to the air voids distribution of SAP-30A, it seems that the air voids size in SAP-30P was slightly larger while that in SAP-30N was slightly smaller. The observation that SAP-30P gave larger air voids distribution is still attributed to the different absorption behavior of SAP particles or the aggregation. The SAP particles in SAP-30P were added to the solution first and had a more free absorption environment. Therefore, the SAP particles could swell more, and their resultant air voids in SAP-30P were slightly larger. On the other hand, the higher tendency of SAP particle aggregation in SAP-30P might also account for this observation, as discussed above. The observation that SAP-30N gave relatively finer air voids could also be attributed to the different absorption environments. SAP-30N is the mixture without the additional activator, i.e., a lower equivalent water/binder ratio. The SAP absorption in the paste with a lower water/binder ratio paste is undoubtedly more difficult than in that with a higher water/binder ratio. Another possibility is the influence of the higher viscosity on the compaction. As mentioned in chapter 3, the workability of the SAP-30N is considerably lower. Therefore, the compaction was less effective than the other mixtures, leading to more remaining air voids in the SAP-30N. Lastly, noises were treated as tiny air voids and might also be accounted for the observation.

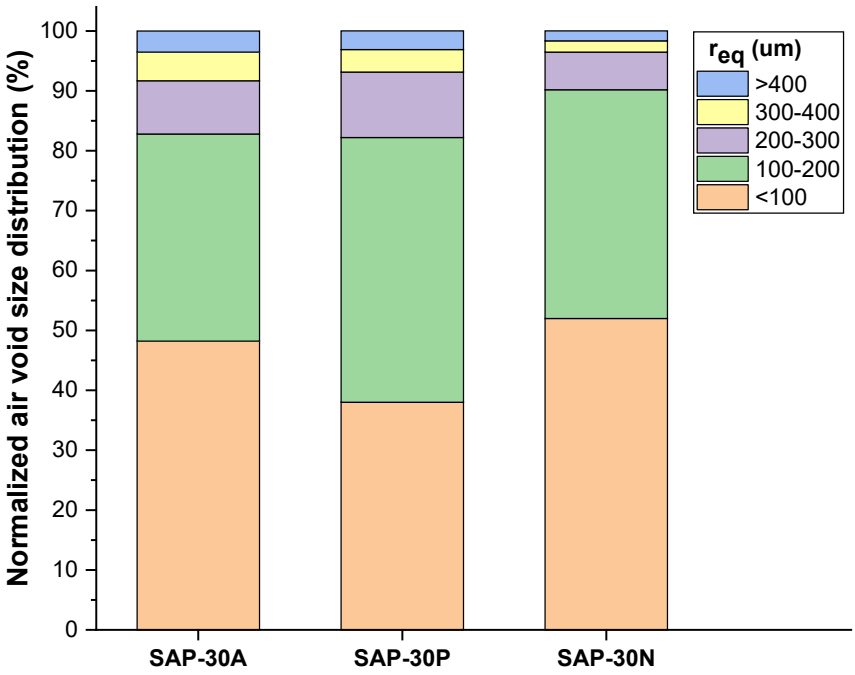

Figure 4.3.10 Air voids size distribution of AASM samples with different SAP absorption compensation methods, normalized by the total amount of air voids

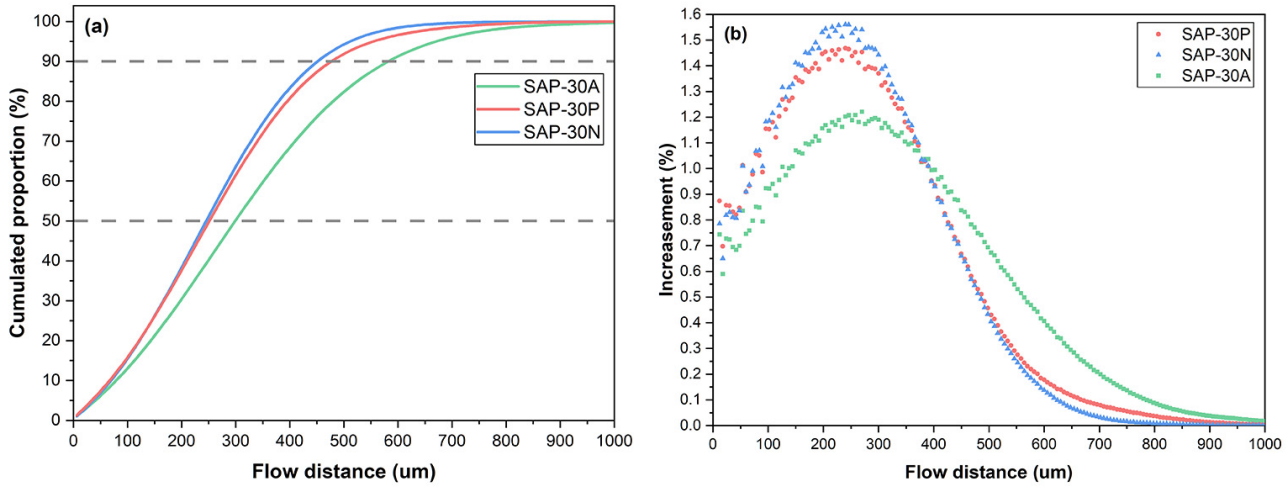

Figure 4.3.11 (a) Cumulated portion and (b) increment of the portion of AASM matrix with different SAP absorption compensation methods in relation to the flow distance

The comparison between the air voids spacing of SAP-30A, SAP-30P, and SAP-30N is shown in Figure 4.3.11. Compared to SAP-30A, the matrix flow distance of SAP-30P and SAP-30N were moderately reduced. For these two mixtures, the d_{50} was around 250 um, and the d_{90} was around 465 um. The reduction found in SAP-30P is attributed to the higher air content and larger air voids, while the reduction in SAP-30N is attributed to the lower paste content and higher amount of tiny air voids.

4.3.2.3 AASM with different SAP particle size distributions

SAP particles with different size distributions are gained by sieving. SAP-30A-C was prepared with the coarse SAP particles remaining on the 250 – 500 um screen, while SAP-30A-F was prepared with fine SAP particles remaining on the 125 – 250 um screen. Figure 4.3.12 shows the visualization

of the air-void system of AASM samples with different SAP particle size distributions. Figure 4.3.13 shows the curve of cumulated air content and the number of air voids at a certain air void equivalent radius r_{eq}.

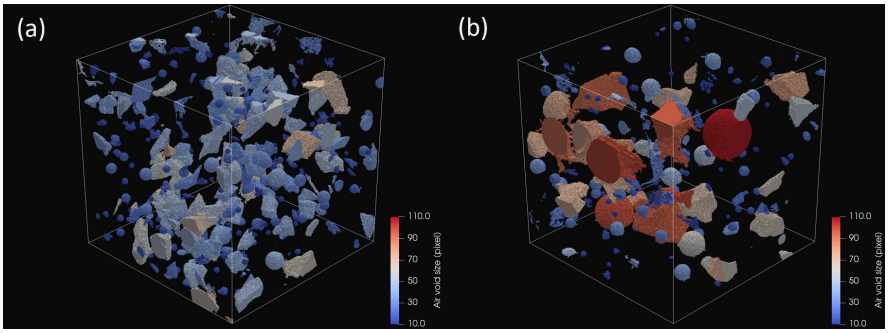

Figure 4.3.12 Visualization of the air-void systems of AASM samples with different SAP particle size distributions: (a) SAP-30A-F; (b) SAP-30A-C. Plotted with mapping the air void equivalent radius with color, noticed that 1 pixel =6 um

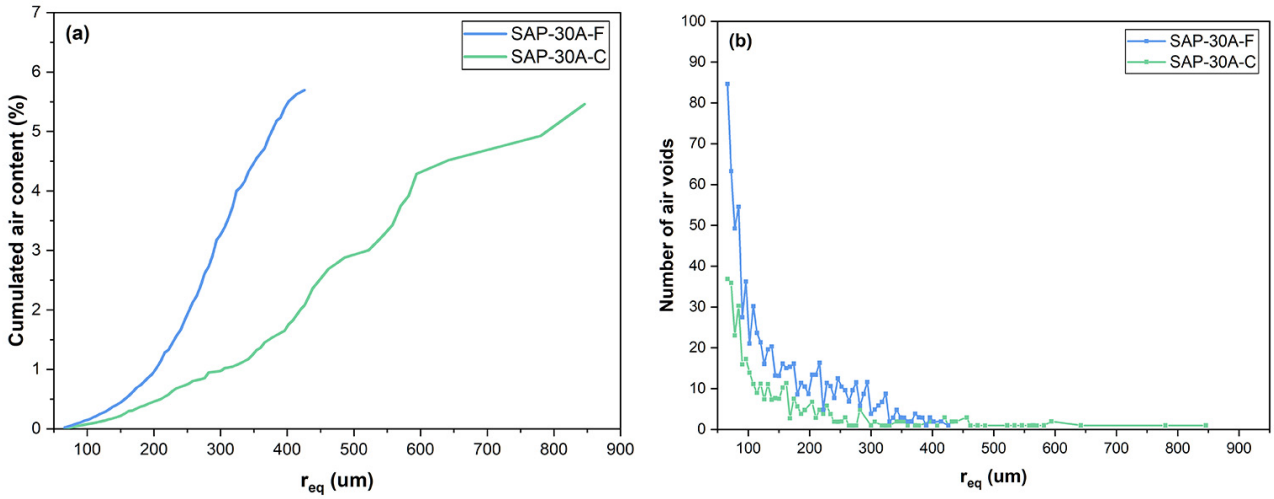

Figure 4.3.13 (a) Cumulated air content and (b) number of air voids at certain air void equivalent radius for AASM samples with addition of SAP of different particle size distributions

Similar air content was found in the SAP-30A-F and SAP-30A-C, indicating that SAP particle size has a minor influence on the amount of absorption. On the other hand, a considerable difference can be found in the air voids size distribution. As shown in Figure 4.3.12, most of the air voids in SAP-30A-F were in blue, i.e., tiny air voids smaller than ~ 360 um. In contrast, for SAP-30A-C, a considerable amount of large air voids in red was found. According to Figure 4.3.13 (a), the upper range of the air void in the SAP-30A-F equivalent radius is around 400 um, while for the SAP-30A-C, the upper range is twice. This magnification is found to be the same as that of the sieved dry SAP particles. In addition, SAP-30A-F also showed a much higher amount of air voids than SAP-30A-C. This is because the dosage of SAP was controlled by weight. Therefore, when the weight of SAP is the same, with a smaller particle size, the number of SAP particles added to the AASM is higher.

Figure 4.3.14 shows the air voids spacing of the mixture SAP-30A-F and SAP-30A-C. A considerably smaller flow distance was observed in the SAP-30A-F mixture. This is attributed to the larger amount of SAP particles in the AASM. According to Figure 4.3.14, the d_{50} and d_{90} of SAP-30A-C is 346 and 684 um, respectively. On the other hand, for SAP-30A-F, the d_{50} and d_{90} reduced to 246 and 486 um.

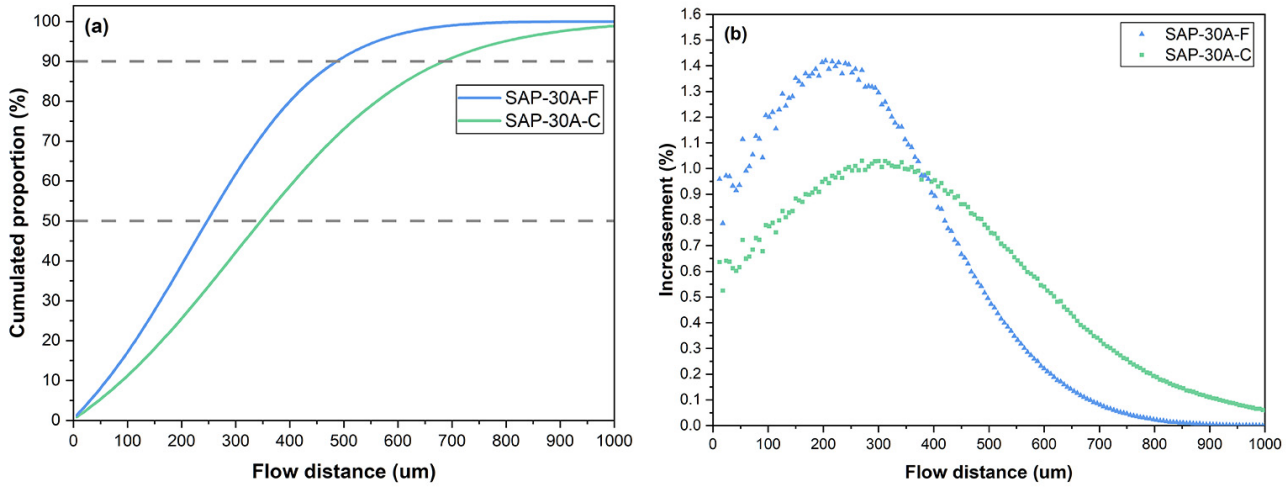

Figure 4.3.14 (a) Cumulated matrix portion and (b) increment of AASM samples with different SAP particle size distributions versus the flow distance

4.3.2.4 AASM with different AEA dosages

Figure 4.3.15 shows the visualization of the air-void systems created by different dosages of AEA, the air content is also noted in the picture. With higher AEA dosage, there was a higher air content and a denser air voids distribution.

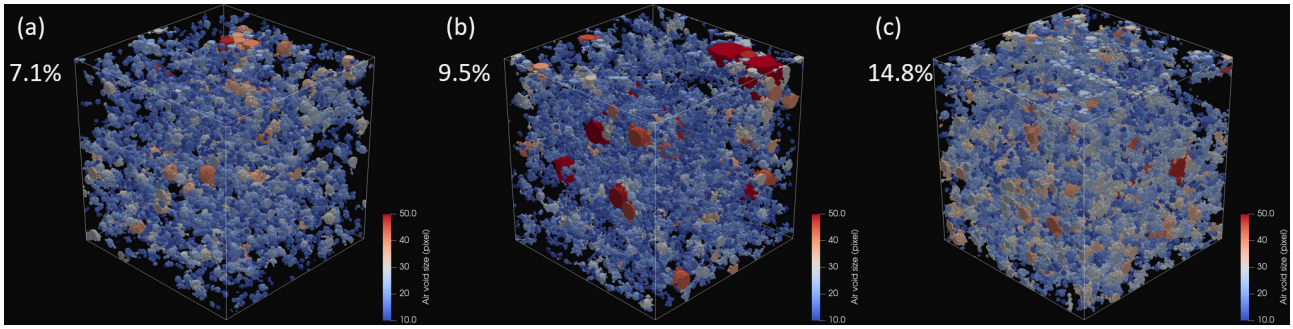

Figure 4.3.15 Visualization of the air-void system of air-entrained AASM with different AEA dosages: (a) AEA-010; (b) AEA-020; (c) AEA-030. The air content is also noted.

The air voids size distribution is shown in Figure 4.3.16. It can be clearly observed that the radius of the entrained air bubbles increased with the increasing AEA dosage. One of the causes behind this is surface tension. AEA absorbs at the interface of liquid and air and lowers the surface tension at the interface [84, 87]. With the higher AEA dosage (below CMC), the surface tension is lower, and the lower the pressure difference across the curved interface. According to the Laplace equation, with a lower pressure difference, the larger the curvature of the interface, i.e., the air bubbles radius. Another cause behind this might be the higher possibility of coalescence and diffusion of the air bubbles when it comes to a matrix that has a larger amount of air bubbles, i.e., when a higher AEA dosage is used [120, 129].

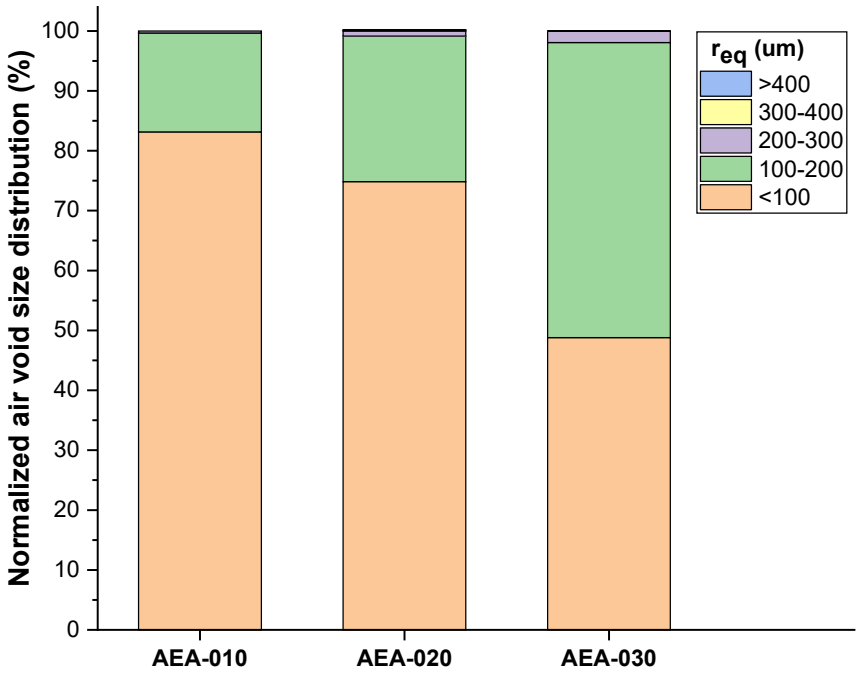

Figure 4.3.16 Air voids size distribution of AASM with different AEA dosages, normalized by the total amount of air voids

Figure 4.3.17 shows the air voids spacing of the AASM with different AEA dosages, noticing that the range of the x-axis is halved from that of the SAP mixtures. With higher AEA dosage, the flow distance curve shifted to the left. The d_{50} ranged from 69 to 114 um, while the d_{90} ranged from 183 to 240 um.

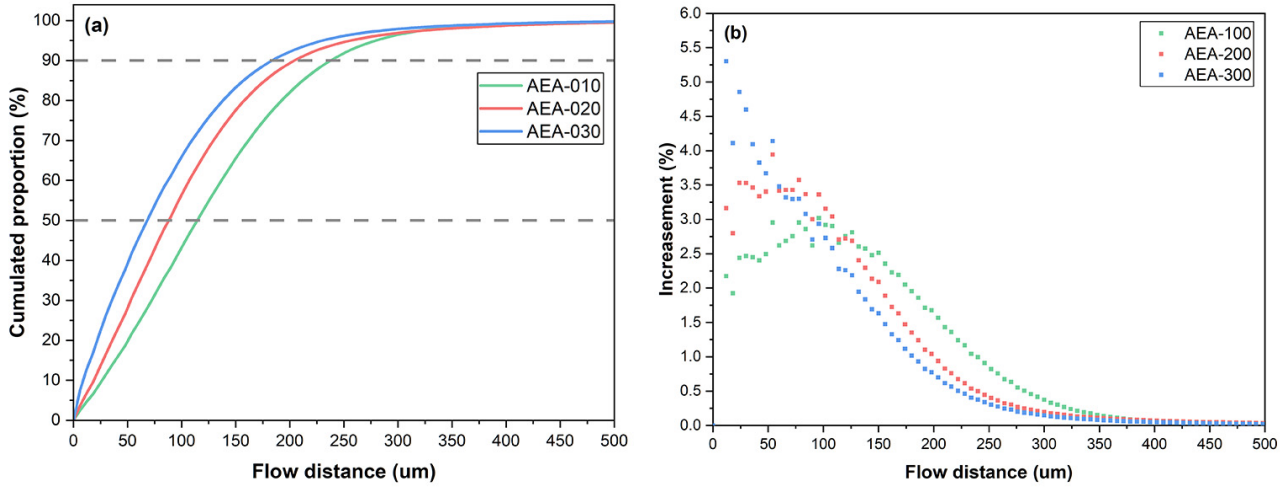

Figure 4.3.17 (a) Cumulated matrix portion and (b) increment of the portion of AASM matrix with different AEA dosages versus the flow distance

4.3.3 Effect of adding SAP / AEA

In this section, a comparison of the air-void system of mixtures with or without SAP/AEA is made. Because of the similar air content, SAP-45A and AEA-010 are chosen as representatives. The visualization in Figure 4.3.18 shows that both admixtures successfully entrained air voids into AASM.

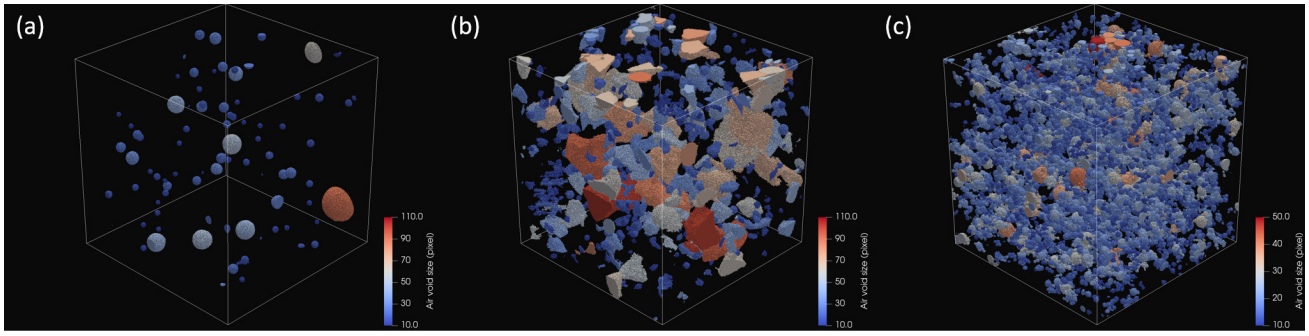

Figure 4.3.18 Visualization of air-void systems in the sample (a) REF; (b) SAP-45A; (c) AEA-010, with mapping of the equivalent radius r_{eq} of the air voids. Noticed that the scale range of the AEA- 010 is different from the other two

Figure 4.3.19 shows the relationship between the cumulated air content and the air-void equivalent radius. Though similar air content was found in SAP-45A and AEA-010, a considerable difference can be found in the size distribution of air voids. The size of the air voids created by AEA is considerably finer than that of SAP. The air voids in the SAP-45A have a similar upper range with REF, while the maximum air voids radius in the AEA-010 was less than 300 um.

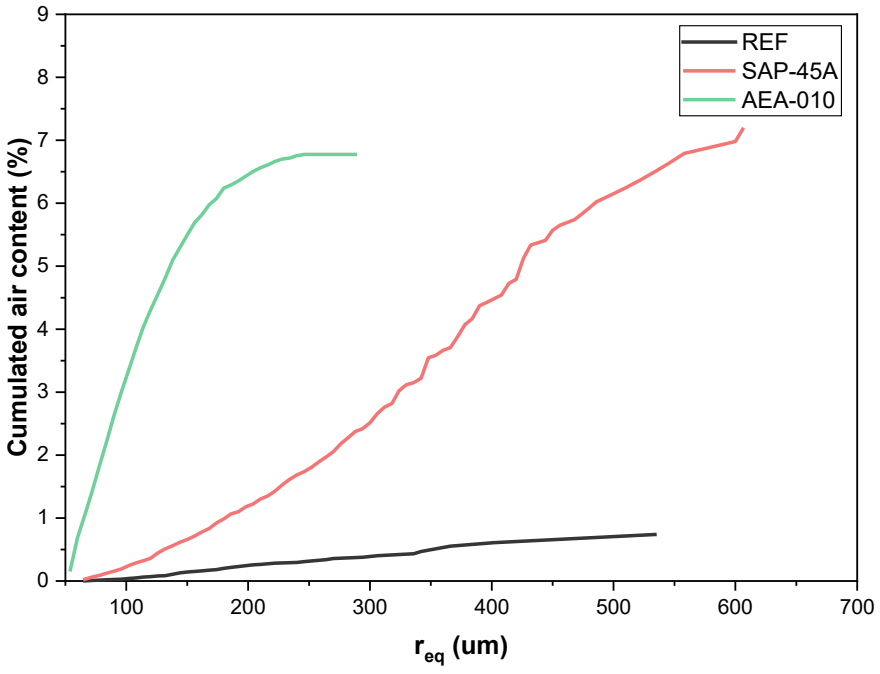

Figure 4.3.19 Relation between the cumulated air content and the air void equivalent radius of mixture REF, SAP-45A, and AEA-010

The curves of the number of air voids at a certain equivalent radius are shown in Figure 4.3.20. For the number of air voids in the hardened AASM, AEA-010 had air voids around 10 times more than SAP-45A, which had around 10 times more than REF.

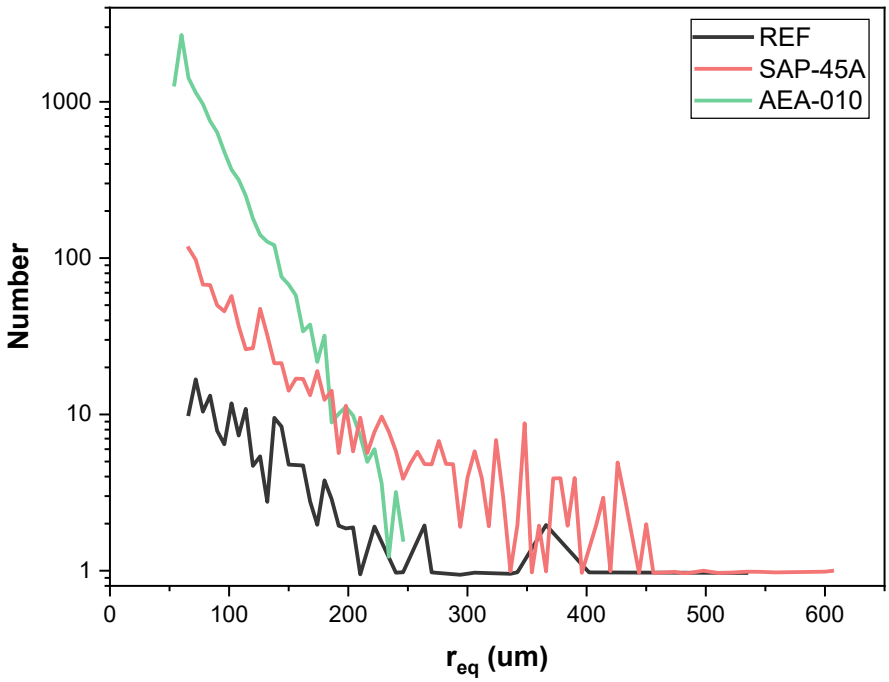

Figure 4.3.20 Number of air voids at certain air void equivalent radius of mixture REF, SAP-45A, and AEA-010

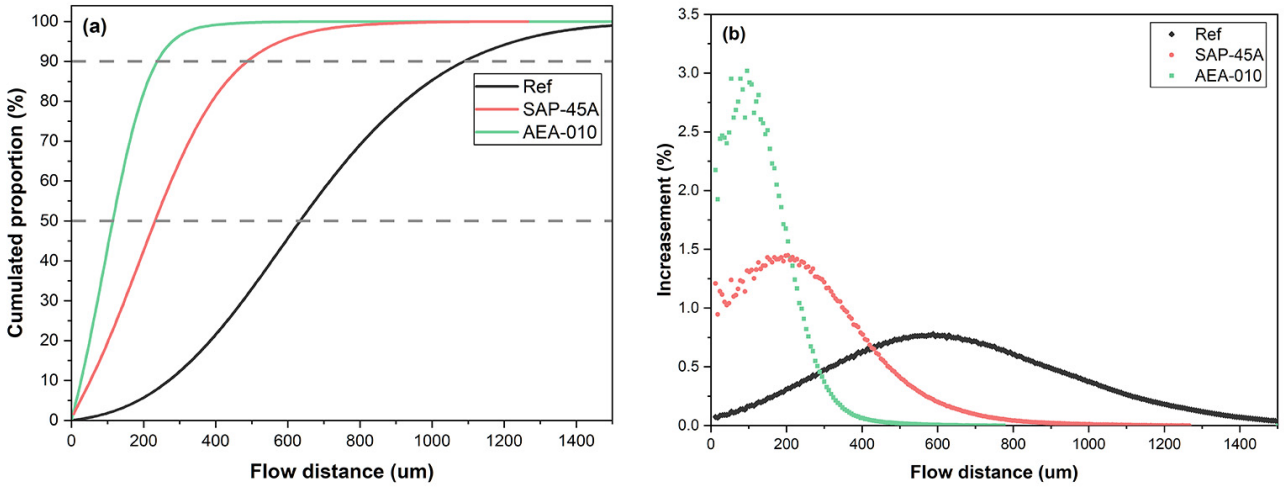

Figure 4.3.21 (a) Cumulated matrix portion and (b) increment of the portion of REF, SAP-45A, and AEA-010 versus the flow distance.

Figure 4.3.21 shows the air voids spacing of the mixture REF, SAP-45A, and AEA-010. Results showed that the addition of SAP and AEA significantly reduced the flow distance of the water in the AASM. The d_{50} and d_{90} of the reference mixture REF is 636 and 1092 um, representatively. With the addition of SAP at a dosage of 0.45% BWOS, these values were approximately trisected. Comparing the SAP-45A and AEA-010, the flow distance of the latter mixture is approximately halved due to the higher amount of air voids. In addition, due to the higher amount of air voids and the closer distribution, the deviation found in Figure 4.3.22 (b) was also considerably lower.

4.3.4 Limitations

Although the micro-CT scan successfully characterizes the air-void system of AASM, there are still some limitations and possible sources of error, which might be addressed in future research:

- The grey level of the AAS binder and aggregate are too close to be differentiated. Therefore, the calculation of the flow distance also includes the voxels that belong to aggregates. This leads to an overestimation of the flow distance.
- The flow distance is calculated by the straight-line distance from the solid phase voxel to the closest air void. The obstructs on the way, such as aggregates, are neglected. This leads to an underestimation of the actual flow distance.
- The effect of the remaining SAP particles in the air void during the freeze-thaw cycles is unclear, but they were accounted as part of the air void due to a similar grey level.
- The incline of the sample is neglected during the characterization, but it might have a minor influence on the volume calculation.
- The sample size might be a bit too small, considering the size of the aggregates. However, due to the limitation of the resolution, it cannot be bigger. Otherwise, the resolution is unacceptable.

4.4 Observations and conclusions

In this chapter, the air-void systems of AASM with or without SAP/AEA were characterized by the micro-CT scan. Air-void system parameters consisting of air content, air voids size distribution, number of air voids, and flow distance were calculated. The main observations and conclusions in this chapter are:

- The addition of SAP and AEA successfully created evenly distributed but quite different air voids in the AASM. The air voids created by AEA are in a sphere shape and have dense spacing. The air voids created by SAP are irregular and considerably bigger, and the spacing is more loosened.
- With similar entrained air content, the amount of air voids created by AEA-010 is approximately ten times higher than by SAP-45A. At the same time, the amount of air voids in SAP-45A is approximately ten times higher than that in REF reference. With the high amount of entrained air voids, the flow distance of the AASM significantly decreased by adding SAP/AEA.
- With increasing SAP/AEA dosage, there was higher air content, slightly increased air voids size, and a denser air voids distribution.
- The SAP absorption compensation method determines the environments for SAP absorption. Prewetting in the activator and mixing with the additional activator create a more freely absorbing environment, leading to higher air content and larger air voids. On the other hand, prewetting and mixing without the additional activator led to a denser air void distribution.
- When the SAP dosage was controlled by mass, finer SAP particles resulted in finer air voids, higher air voids amount, and denser air voids distribution. On the other hand, the air content seemed to be less influenced by the SAP particle size distribution.

The air-void systems of AASM mixtures characterized in this chapter are crucial for freeze-thaw resistance. This chapter provides valuable information for explaining the freeze-thaw performance of different AASM mixtures in chapter 6.

5 The surface microstructure of AASM and the influence of drying, SAP, and AEA

5.1 Introduction

Surface scaling damage is the loss of materials at the surface layer of concrete during freeze-thaw cycles [8, 19]. The microstructure near the test surface can significantly influence the surface scaling resistance [14, 28]. If the concrete microstructure near the test surface is porous, cracky, and weak, its surface scaling resistance is likely to be poor. Compared to OPC concrete, some types of AAMs concretes have a surface layer more susceptible to external factors such as drying and carbon dioxide [10]. AAS is one of these susceptible AAMs. When exposed to an unfavorable external environment, the microstructure of the AAS surface layer can be totally different from that of the main internal body, and high porosity as well as surface cracking can be expected [29].

Drying is one of these unfavorable circumstances for AAS concrete, but drying is inevitable in most applications and one of the necessary preconditioning in most surface scaling test protocols. In the CDF test, the drying procedure begins on day 7 and lasts for 21 days; in the ASTM C672 test, the drying procedure begins on day 14 and lasts for 14 days. The currently available surface scaling tests are initially designed based on OPC concrete. Such a drying procedure might only have a minor influence on the 7-day OPC concrete, but it might be unfavorable to AAS concrete because of the high cracking potential under drying. And it might unnecessarily underestimate the surface scaling resistance of AAS concrete for the curing time can be specifically adjusted for AAS according to its characteristic instead of setting as 7 days.

Therefore, it is interesting to see the microstructure of the surface layer of AASM underwent different conditions. In addition, it is well known that SAP can provide internal curing and reduce shrinkage. For this reason, the influence of SAP/AEA on the surface microstructure of AASM is also interesting to reveal.

The microstructure of the AASM surface can be investigated by the optical microscope. Cracking and porosity of different mixtures can be easily qualitatively compared when fluorescence is applied and the sample is impregnated by the epoxy containing dye.

Accordingly, the objective of this chapter is defined as investigating the surface microstructure of AASM with or without SAP/AEA after specific curing and drying procedure.

5.2 Materials and methods

5.2.1 Materials and mix proportions

The raw materials that have been characterized in chapter 3 will still be used in the study of this chapter. Mix proportions of REF, SAP-45A, and AEA-010 will be included. For simplification, the mix proportion SAP-45A and AEA-010 will be referred to as SAP and AEA, respectively. The sample preconditioning consists of curing and subsequent drying. The drying procedure starts after 7-day curing (The CDF test) or 14-day curing (ASTM C672 test), while the drying is fixed to 14 days. This is to investigate the influence of age of AASM when exposed to drying. Samples cured for 28 days without drying are also included to see the effect of drying. This preconditioning creates a relatively similar microstructure to the inner part of the sample that is believed to be “representative”

to the specimen. And it is also the surface condition at the beginning of many tests, such as mechanical properties, carbonation resistance, and chloride migration. The preconditioning information of the mixtures is shown in Table 5.2.1.

After mixing, the fresh mortar is casted into cylinder bottle molds with an inside diameter of ~ 30 mm. The bottles containing fresh mortar are then sealed with the incidental lid. After curing at 20℃ for 1 day, the hardened mortar is demolded and sealed. Then the curing in the preconditioning is continued. The selected curing condition of AASM is different from the curing conditions addressed in the CDF method (underwater) and ASTM C672 (moisture). This is to avoid possible leaching issues when AASM is in contact with water at an early age.

Table 5.2.1 Mixtures for investigating the surface microstructure

Mixtures	Preconditions		Ref
	Sealed curing	Drying	
REF/SAP/AEA-**S7D14**	7 days	14 days	CDF test
REF/SAP/AEA-**S14D14**	14 days	14 days	ASTM C672
REF/SAP/AEA-**S28D0**	28 days	0 day	-

5.2.2 Characterization of surface microstructure

Characterization is conducted on the molded surface of the hardened AASM. After preconditioning, the bottom surface is vacuum impregnated with low-viscosity epoxy containing a special yellow color dye. In this way, the contrast among the cracks, aggregates, and binder is enhanced, and they can be easily differentiated due to different amounts of absorbed epoxy. After the impregnation, the sample is placed for 24 hours to let the epoxy harden. Afterwards, several micrometers of epoxy on the characterized surface of the samples are carefully removed by grinding. The thickness of samples during grinding is carefully monitored, and all the samples have similar ground thickness.

Afterwards, optical microscopy is used to characterize the surface condition of the AASM samples. With the application of fluorescence and filter, the dye in the epoxy that remained in the cracks and pores is green, while the solids phase is black. In this way, the microcracking on the surface can be easily recognized, for they are in green and show the highest brightness. The images are acquired by an image collector and computer. The configuration is identical for all the samples. In this way, the difference between the paste's porosity or pore size distribution can be qualitatively compared by the intensity of the dye color.

5.3 Results and discussions

5.3.1 General information

The surface microstructure of AASM was investigated by optical microscopy. Mixtures with different preconditioning were investigated to see the influence of drying on day 7 and day 14 on AASM, which is involved in the CDF test and ASTM C672 test. Mixtures with or without SAP/AEA were investigated to see how SAP and AEA influence the surface microstructure.

For illustration, Figure 5.3.1 shows the full surface of the reference mixture after 28 days of sealed curing, and Figure 5.3.2 shows a typical surface microcracking. With the application of fluorescence light and filter, only the color green and black can be seen in the micrographs. The green color is referred to the voids, cracks, and pores that are filled with epoxy containing dye. The black color is referred to the solid phase, i.e., aggregates and solid skeleton in the paste. The round green circle in the middle is due to the shape of the mold.

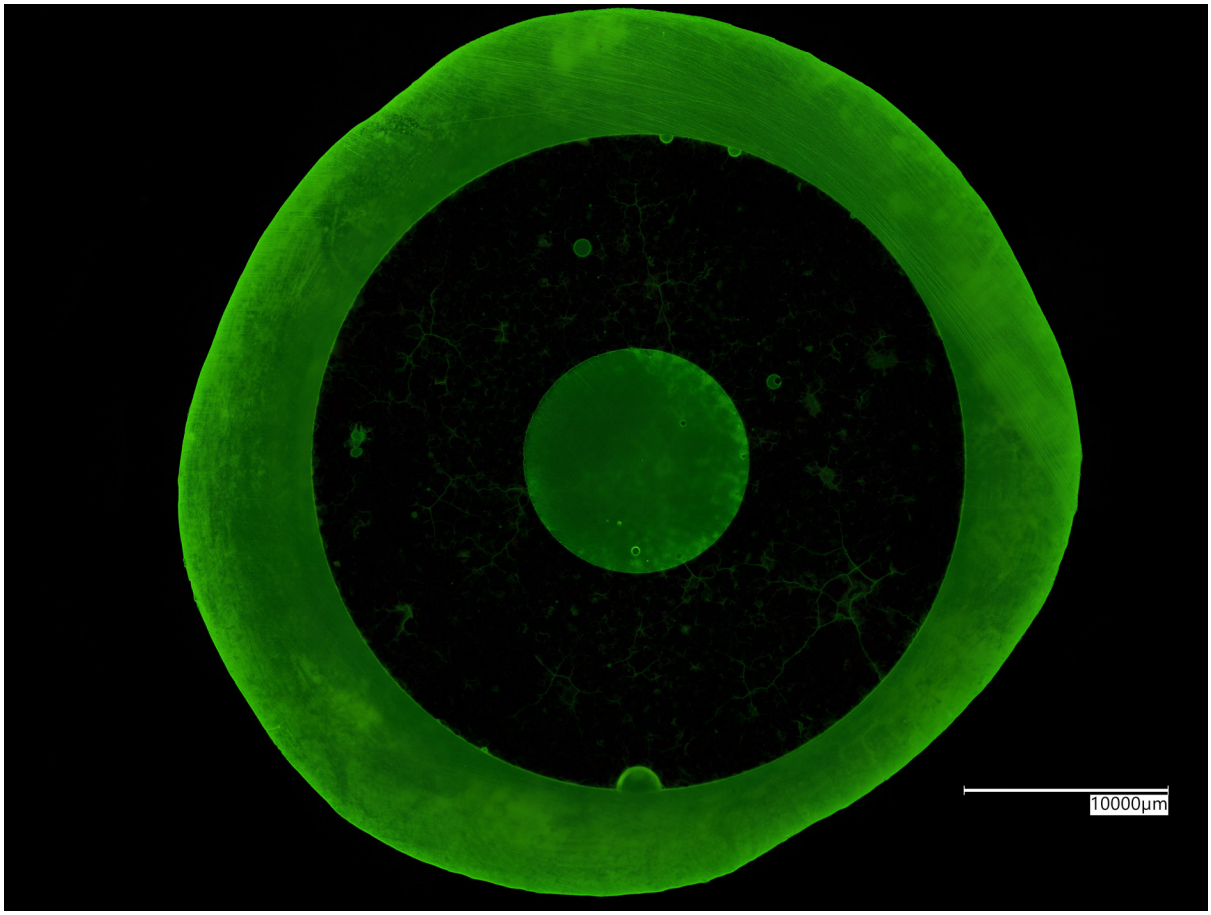

Figure 5.3.1 Full surface of the REF specimen after sealed curing for 28 days (REF-S28D0) and impregnated with epoxy. Acquired by optical microscope under fluorescence light

5.3.2 Surface microstructure of sealed AASM with or without SAP / AEA

Figure 5.3.2 shows the representative surfaces of REF/SAP/AEA-S28D0 specimens that were sealed for 28 days before the epoxy impregnation. This is the condition of AASM in many tests or characterizations, such as mechanical properties, carbonation resistance, and chloride migration. Compared to the other two preconditioning conditions in the following section, it also provides the most similar microstructure to the internal bulk body of AASM.

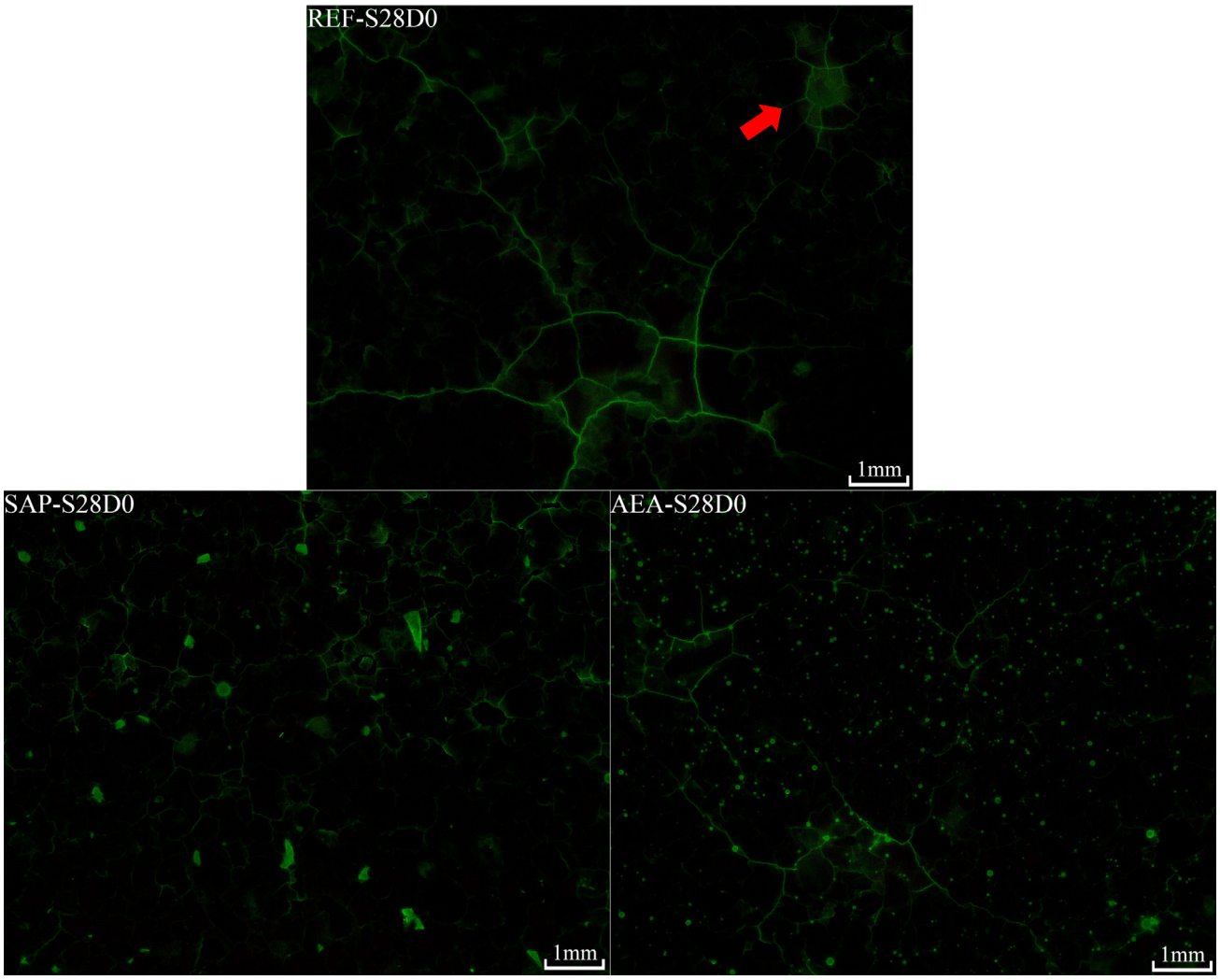

Figure 5.3.2 Surface detail of REF/SAP/AEA-S28D0 obtained by optical microscope with fluorescence and filter

As shown in Figure 5.3.2, for all the mixtures, most of the area was in black, and the paste and aggregates in AASM cannot be differentiated. This is attributed to the low porosity as well as the fine pore size distribution of sodium silicate-activated slag paste, as reported in previous literature [2, 130]. A large portion of the pores in AAS paste are gel pores with a radius smaller than 10 nm. These tiny gel pores are very difficult for the low-viscosity epoxy to ingress [130-132]. With such a dense microstructure, the amount of impregnated epoxy in the paste is limited. Therefore the intensity of the dye color is low (i.e., in black) for the paste under the fluorescence light.

Microcracking and voids are in green and can be easily recognized in the images. Obvious developed microcracking was locally found in the REF-S28D0. With the application of AEA, the extent of cracking seemed to be slightly reduced by showing a narrower crack width. When SAP was added, only a minor extent of tiny microcracking was found.

Since the sample was not dried before the impregnation, the cracking found on the REF/SAP/AEA-S28D0 surface is attributed to the autogenous shrinkage. Autogenous shrinkage is the shrinkage occurring in isothermal conditions and the absence of moisture exchange between the specimen and the surrounding environment [133]. Although the underlying driving forces behind the autogenous shrinkage of AAMs are not as clear as that of OPC [134], the dominating driving force behind the autogenous shrinkage is still widely attributed to be the pore pressure caused by self-desiccation and chemical shrinkage. With the decreasing internal humidity over time, capillary force is created as a result of the formation of the meniscus at the vapor/liquid interface. The liquid is subjected to tension and creates compression in the matrix. This results in the shrinkage of the solid skeleton [135, 136]. The autogenous shrinkage and resultant cracking potential of AAS are found to be significantly high [10, 134, 136-139]. Most of the studies attributed these to the finer pore structure of AAS and its resultant higher pore pressure [130, 134, 136, 138, 139]. Besides, the higher surface tension of the pore solution [136], higher viscoelasticity [134, 140], and other extra driving forces [134, 140] might also contribute. If free deformation is allowed, high autogenous shrinkage of the AAS paste itself will not initiate cracks. However, if the deformation is restrained, internal tensile stress will be generated, and cracking will occur when the tensile capacity is exceeded. In AASM, the aggregates do not shrink like the paste due to a decrease in RH. Because of this mismatch in deformation, aggregates restrain the shrinkage of AAS paste, and tensile stress is created. As a result, cracks will be generated when the tensile capacity of the paste is exceeded [141, 142].

Therefore, the observed microcracking on the surface of S28D0 samples is attributed to the autogenous shrinkage and the restraint of the aggregates. A piece of evidence can be found in the mixture REF-S28D0 in Figure 5.3.2. As indicated by the red arrow, map cracking was found centered on a bright spot. This bright spot might be attributed to the porous ITZ around a big aggregate, which is impregnated by the high amount of epoxy, and surrounding cracking was generated due to the restraint of this aggregate.

With the addition of AEA, the surface integrity of AASM seems to be slightly reduced. This might be due to the energy dissipation function of the air voids. Drilling a circular hole at the end of a crack is a common temporary measure in steel structures to stop or delay crack development. It might be a similar case here. When a crack propagates into an air void, its energy will dissipate all over the air void, and the propagation might be stopped or delayed [103]. However, if the driving force provides high enough energy, the crack will still go through the voids and continue to develop. In the case studied here, it seems that the entrained air voids do dissipate a certain effect in dissipating energy, but the effect is limited.

With the addition of SAP, the surface integrity of AASM is significantly improved. As shown in Figure 5.3.3, for SAP-S28D0, the long, wide, developed crack noticed in REF-S28D0 and AEA-S28D0 was not observed. Only a few tiny microcracks existed on the sample surface, and their extent of development was quite limited. The considerable improvement is attributed to the lower autogenous shrinkage as a result of the internal curing by SAP [91, 93, 143]. A dominating driving force behind the autogenous shrinkage is the pore pressure caused by the reducing internal RH. SAP, as an internal curing agent, homogenous distributes in the AASM and absorbs liquid during mixing. As the AASM dries, the SAP particles serve as internal water reservoirs and gradually release the absorbed liquid. In such a way, the internal RH of AASM is maintained at a high level for up to a few weeks [91, 144]. As a result, at the early stage that the AASM has a low degree of reaction and low tensile capacity, the extent of autogenous shrinkage is considerably limited by SAP, and so does the generated tensile stress and cracking potential. When it comes to the later stage, AASM has already gained a high degree of reaction, and the cracking potential is limited by the developed mechanical properties. Thus, a much more intact surface was found in the SAP-S28D0 surface.

In addition, voids created by SAP might also be capable of dissipating the energy of cracks. However, considering the loose air voids spacing found in chapter 4 and the limited effect of energy dissipation found in AEA-S28D0, the benefit of cracking energy dissipation provided by SAP voids is probably neglectable compared to internal curing.

5.3.3 Surface microstructure of reference AASM with or without drying

Figure 5.3.3 compares the surfaces of REF AASM with different preconditioning (S28D0/S7D14/S14D14). Two obvious differences can be identified: one is the extent of map cracking, and the other is the color of the paste. The significant surface microcracking potential of AASM, when exposed to dry ambient air, was found, even though the drying was started at a not very early age (7 days and 14 days). As shown in Figure 5.3.3, the extent of cracking was significantly greater in the two dried samples. Besides, the paste of REF-S28D0 was in black and cannot be differentiated from the aggregates. On the other hand, for the dried surface, the paste was in green and could be quite easily identified from the aggregates, which remained black.

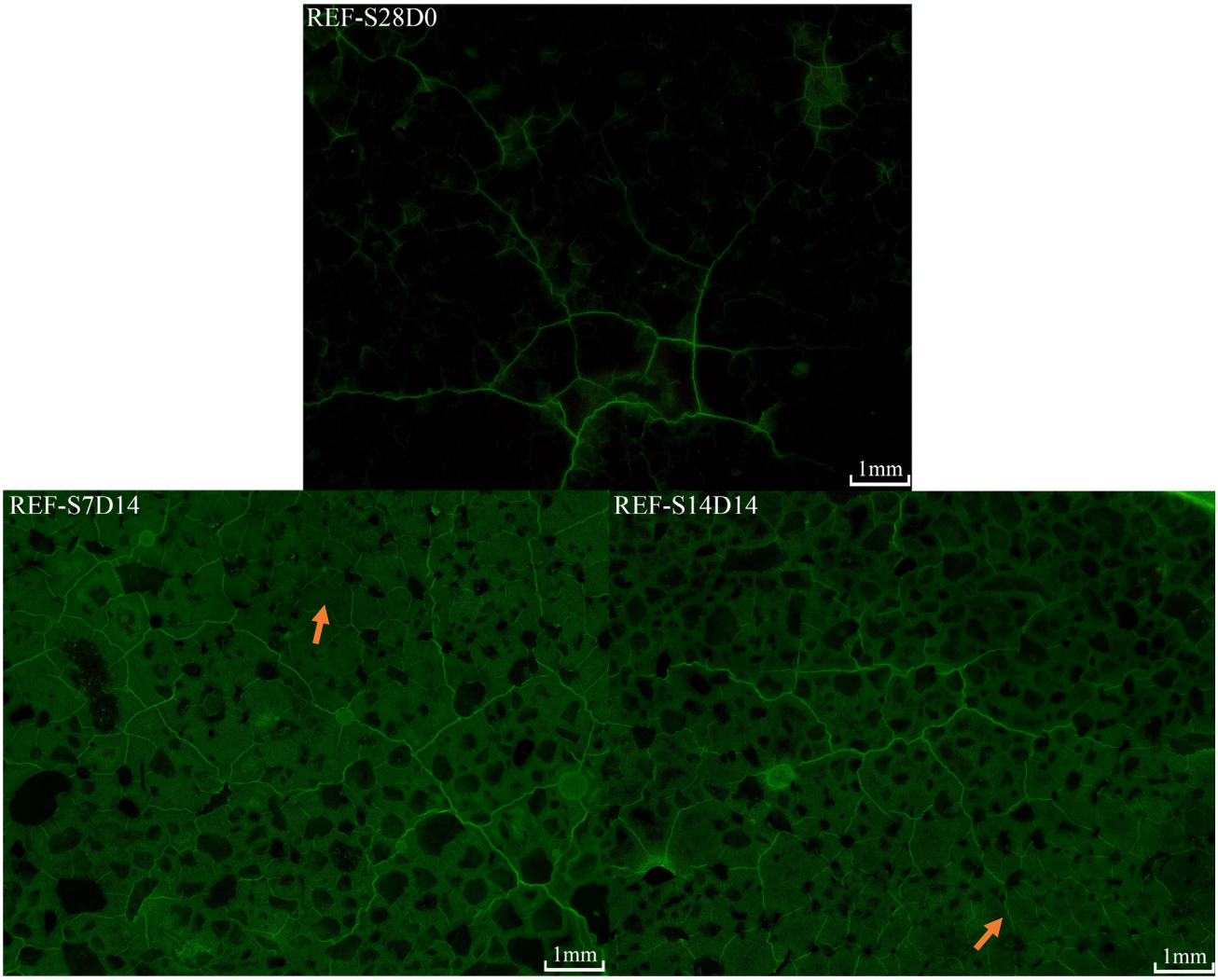

Figure 5.3.3 Surface detail of REF-S28D0/S7D14/S14D14 obtained by optical microscope with fluorescence and filter

The green color is due to the dye in the epoxy. Such a considerable variation in the dye color intensity indicated the difference in the paste pore structure. In terms of epoxy impregnation, the microstructure in REF-S28D0 is so dense that difficult for the low-viscosity epoxy to penetrate, as discussed above. However, the larger the pore radius, the more easily the epoxy can ingress, and the

higher amount of epoxy remains in the paste [131]. As a result, the green dye color intensity in the paste increases. Additionally, if the porosity of the paste is higher, undoubtedly that the dye color intensity will also increase due to the higher amount of impregnated epoxy. Therefore, the higher dye color intensity in REF-S7D14 and REF-S14D14 indicates a considerably larger pore size distribution as well as a possible higher pore volume than REF-S28D0. A similar effect can be found in the literature studying the effect of curing regimes [29, 66, 68]. When the AAS is cured at dry ambient air, the porosity and pore size distribution are found to increase with decreasing distance to the surface as a result of the humid distribution. And the porosity and pore size distribution are considerably higher than samples cured under sealed or humid conditions [29, 66]. Compared to REF-S28D0, the preconditioning of REF-S14D14 can be understood as changing the curing regime from sealed to exposed in the latter 14 days. As a result, a coarser microstructure at the surface can be found due to drying, i.e., inadequate curing. The mechanisms behind this might be attributed to the interruption of reaction due to the evaporation of water and lower RH. Also, due to the difference in the degree of reaction, compared to REF-S7D14, REF-S14D14 had an additional 7-day reaction prior to drying, and the microstructure was slightly denser. Therefore, it showed a lower intensity of dye color.

Another significant difference observed on the surface of dried specimens was the higher-developed map cracking. On the surface of REF-S28D0, though map cracking can also be found, it was relatively locally distributed in parts of the cross-section. The map cracking was not highly developed, and the origin of the cracking can be roughly identified. On the surface of REF-S7D14 and REF-S14D14, the map cracking is more universally distributed. No obvious origin of cracking can be found because the cracks are so developed that they are all connected. In addition to the large cracks, very dense tiny microcracking can also be found, as indicated by the red arrows in Figure 5.3.3.

This considerably higher extent of map cracking of the dried samples is attributed to the drying shrinkage after the exposure. In terms of drying shrinkage, its mechanism is very similar to autogenous shrinkage. They are both created by pore pressure due to the reduction of internal RH. When the AASM is exposed to dry ambient air, water evaporates from the pores in the porous AASM surface layer. Pore pressure is then created and results in drying shrinkage of the paste [135]. When the shrinkage is restrained, tensile stress is generated and might create cracks. Similar to the case of autogenous shrinkage, aggregates will restrain the drying shrinkage of the paste. In addition, because the drying occurs gradually from the surface to the internal, a humidity gradient exists along the thickness of AASM, so as the resultant pressure and strain. The drying shrinkage at the internal part is smaller than at the surface. Therefore, the drying shrinkage of the outer AASM layer is also restrained by the inner layer due to the mismatch in deformation. Such action is analogous to thermal gradient and might also result in cracking at the outer layer with higher shrinkage. Nevertheless, it can be concluded that, due to the restraint, the drying shrinkage and autogenous shrinkage create considerable map cracking on the surface of REF-S7D14 and REF-S14D14.

It is also noticed that, although the REF-S14D14 had a higher degree of reaction when exposed to drying, the extent of map cracking was similar to REF-S7D14. The reason behind this might be the smaller pore radius due to the additional reaction. The magnitude of the capillary force that can be induced in the matrix is inversely proportional to the pore radius. With finer pore size distribution, a higher capillary force during drying can be created [135]. Therefore, although the REF-S14D14 had a higher resistance to cracking, it might also have a stronger cracking force. In addition, longer curing time also means a greater extent of autogenous shrinkage. As a result, no difference in cracking potential was observed between the REF-S7D14 and REF-S14D14.

The significant surface microcracking might also contribute to the greener AAS paste observed in REF-S7D14 and REF-S14D14. With the greater extent of microcracking, the porosity and the

interconnectivity of the AAS paste are higher. As a result, the epoxy could more easily penetrate into the paste, and a higher amount of epoxy was incorporated into the paste. This way, the paste showed a higher intensity of the dye under fluorescence.

The observation in this section is alarming. AAS binders are believed to have the characteristic of dense microstructure with high portions of mesopores [2, 130], which is generally believed to be beneficial to durability. However, this might be a misperception. For the characterization of pore structure, usually, the samples are taken from the "representative" internal bulk body of AAS, while the microstructure near the surface of AAS was usually regarded as "not representative". However, for durability issues such as surface scaling, chloride penetration, and carbonation, the microstructure near the surface is more important than that of the bulk body. In the OPC system, the difference in microstructure along the thickness might be small. However, the AAS system showed high sensitivity to the external environment, and the difference in the microstructure along the thickness can be quite different [29]. A much more porous microstructure was found in the REF-S7D14/S14D14 than in REF-S28D0. Therefore, when it comes to the durability issue concerning the surface, whether the microstructure characterized with samples taken from the internal body or from another preconditioning history (such as 28-day seal curing) is still representative of real microstructure in the durability test is questionable. Such ignorance might lead to many misunderstandings.

5.3.4 Effect of SAP/AEA on the surface microstructure when subjected to drying

Figure 5.3.4 shows the surface of AASM dried for 14 days after 7-day or 14-day seal curing. A considerable extent of map cracking and high dye color intensity of the paste can be found on the surfaces of all the mixtures, regardless of the application of the admixtures. Nevertheless, it seems that the surface condition was still improved by the admixtures, especially by the SAP.

In order to clearly reveal the effect of SAP/AEA, the conditioning of the samples is divided into two stages. The first stage is when the AASM samples are under sealed curing. During the first stage, there was no moisture exchange between samples and the external environment, i.e., there was only autogenous shrinkage and no drying shrinkage. The second period is when samples were unsealed and exposed to 55% RH ambient air. During the second stage, both autogenous shrinkage and drying shrinkage existed.

Therefore, the observed surface condition was the result of the effect of autogenous shrinkage in the first stage and coupling with the effect of drying shrinkage and autogenous shrinkage in the second stage. To reduce the complexity, considering the fact that most of the autogenous shrinkage and its resultant cracking occurs in the first few days, as well as that humidity reduction caused by drying is much more significant than self-desiccation at the sample surface during the second stage, it is assumed that the first stage is dominating by autogenous shrinkage while the second stage is dominating by the drying shrinkage. With this assumption, for the second stage, the effect of drying will be analyzed based on the resultant surface from the first period, and the contribution of autogenous shrinkage is neglected. In other words, the microcracking on the surface will be analyzed by divining the preconditioning into two steps: in the first stage, cracking caused by only the autogenous shrinkage on an intact surface after casting, and cracking in the subsequent second stage after brought to drying where only the effect of drying shrinkage on the unperfect surface (due to the autogenous shrinkage in the first period) is considered.

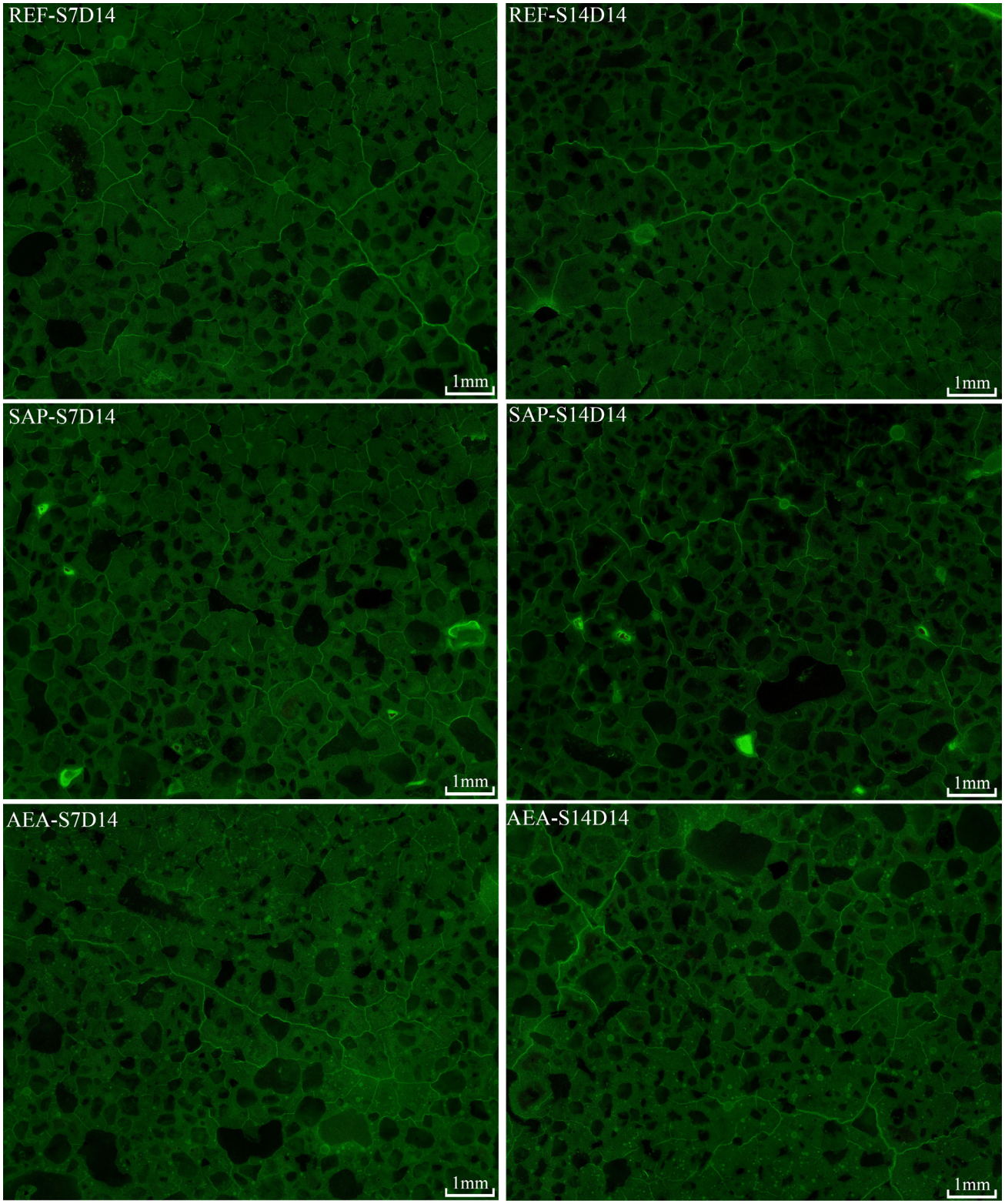

Figure 5.3.4 Surface detail of dried AASM, with or without adding SAP/AEA

In the first stage, the samples were sealed, and only autogenous shrinkage was involved. At this stage, a considerable extent of cracking caused by autogenous shrinkage can be found on the surface of the REF sample sealed for 28 days, as shown in section 5.3.2. For the dried samples, the length of the first stage was shorter (7 days or 14 days), and no surface condition before the sample was brought to drying was documented. However, for AAS without internal curing agents to preserve the

internal RH, most of the surface microcracking caused by autogenous shrinkage is likely to happen at quite early age [136, 138, 141, 145]. Therefore, it can be expected that a comparable extent of surface microcracking had already existed before the REF/AEA-S7D14 and REF/AEA-S14D14 were brought to drying, i.e., at the end of sealed curing. In addition, without internal curing, there was already a considerable reduction in the RH [91, 143, 144, 146]. On the other hand, with the addition of SAP, the surface of SAP-S7D14/S14D14 was much more intact after the first stage due to the internal curing. Also, considering the relatively high SAP dosage of 0.45% BWOS, the internal RH was maintained at a high level [91, 143, 144, 146].

Therefore, after the first stage, the surfaces of AASM without the addition of SAP (REF/AEA-S7D14 and REF/AEA-S14D14) were very likely to have a comparable extent of microcracking to REF/AEA-S28D0, as well as a considerable reduction in the internal RH. On the other hand, due to the benefit of internal curing by SAP, the SAP-S7D14 and SAP-S14D14 had a more intact surface as well as a high internal RH.

In the second stage (i.e., exposed to dry ambient air), near the surface, evaporation is much more significant than self-desiccation in the perspective of generating pore pressure and shrinkage. With the Kelvin-Laplace equation, Mackenzie's equation, and Pickett's aggregate restraint model, the shrinkage caused by pore pressure under the restraint effect of aggregate can be written as [144]:

$$\varepsilon = \left(\frac{S}{3}\frac{RT}{V_{\mathrm{m}}}\right)\left(\frac{1}{K}-\frac{1}{K_{\mathrm{S}}}\right)\left(1-V_{\mathrm{a}}\right)^{n}\ln\left(RH\right)$$

where S is the saturation fraction, R is the universal gas constant, T is the absolute temperature, V_{m} is the molar volume of the pore solution, K and K_{S} is the bulk modulus of the porous materials and solid backbone, V_{a} is the total aggregate content by volume, n is the constant relating to the restraint of aggregate, and RH is the relative humidity.

It can be observed that the resultant strain is considerably influenced by the variation of RH. With the evaporation of water, the RH of AASM decreases, and the shrinkage caused by pore pressure increases. Due to the restraint of aggregate, the tensile stress in the paste increases, and cracking occurs if the tensile capacity is exceeded.

The surface conditions of different mixtures are then discussed:

REF-S7D14 and REF-S14D14

For dried REF mixtures, a certain extent of tensile stress had already been developed in the paste due to the reduction in RH during the first stage. During the drying, the tensile stress continuously increased and generated cracks with the evaporation of water. In addition, due to the pre-existing microcracks initiated in the first stage, the interconnectivity of the paste was higher, which further led to a higher decrease rate of RH. As a result, dense map cracking was created, as observed in Figure 5.3.4.

SAP-S7D14 and SAP-S14D14

For dried SAP mixtures, the pre-existing tensile stress was limited due to the high RH in the paste. When exposed to the dry condition, the remaining absorbed liquid in the SAP particles continuously compensated for the effect of evaporation. In addition, the permeability of the paste was also lower than cracked REF mixtures. Therefore, the AASM with SAP has a lower pre-existing tensile stress in the paste before drying, as well as a lower rate of stress development during drying. As a result, the surface integrity of SAP-S7D14 and SAP-S14D14 was better than the REF counterparts. However, compared to the significant effect of reducing autogenous shrinkage microcracking by SAP, the reduction in microcracking caused by drying shrinkage is much less effective. This conforms to the

observation in reference [147]. And it might be attributed to the fact that not much liquid had left in SAP after the first stage, and the drying caused by evaporation is much faster.

AEA-S7D14 and AEA-S14D14

For dried AEA mixtures, large map cracking was found on the surface, which was likely to be created by the autogenous shrinkage in the first stage. Interestingly, the extent of tiny map cracking seemed to be lower than REF and SAP counterparts. Information in the literature regarding the effect of air-entraining on the drying shrinkage of paste is scarce. If it is not caused by the grounding, this reduction might be attributed to the interruption of the pore connectivity by the dense entrained air voids [103]. In this way, the rate of evaporation was reduced. On the other hand, the dense air voids might also dissipate the cracking energy of the tiny cracks and limit their development, as discussed above [103].

From the perspective of the dye color intensity of the paste, a slight difference can be observed among these six samples. The intensity of the samples dried on day 14 was slightly lower than that of the samples dried on day 7. This is because of the denser microstructure in REF/SAP/AEA-S14D14 due to the additional 7-day geopolymerization reaction. Comparing the SAP mixtures and REF/AEA mixtures that underwent the same preconditioning, no obvious difference in dye color intensity can be found in SAP-S7D14, while a slightly lower dye color intensity can be found in SAP-S14D14. This difference is attributed to the more obvious densification by later stage internal curing. At the first 7 days of curing, the AASM samples had a relatively low degree of reaction, and the effect of internal curing provided by SAP was unobvious. When the curing was prolonged to 14 days, the reaction speed of REF/AEA-S14D14 continuously slowed down due to the consumption of reactants. On the other hand, with the addition of SAP, the remaining absorbed activator continuously released and compensated for the consumption of reactants. This internal curing resulted in an obvious higher later age degree of reaction in SAP-S14D14. In this way, the higher amount of reaction products in the SAP-S14D14 creates a denser microstructure than REF/AEA-S14D14 and therefore a lower dye color intensity. This difference in microstructure also supports the finding and explanation in section 3.5.1.1 that SAP mixtures had a higher compressive strength increment from 7 days to 28 days due to the internal curing.

These observations in dye again indicate that a considerable difference might exist in microstructure between the surface layer and inner bulk body of AAS that is exposed to drying, even if the drying starts after 14 days of curing. For this reason, the microstructure characterized by the sample taken from the core of the AAS might not be representative of the actual microstructure at the surface. Concerning the fact that many durability issues are largely determined by the microstructure at the surface layer, sampling position might lead to a misjudgment of the resistance. In future studies, caution might need to be taken for this characteristic of AAS.

5.3.5 Summary of results

In this section, the full surfaces and zoomed-in details of all nine mixtures are summarized. The full cross-sections of the nine investigated mixtures are shown in Figure 5.3.5. The images are arranged in 3 columns and 3 rows, which are grouped by their mix proportions (REF, SAP, AEA) and preconditioning conditions (S28D0, S7D14, S14D14), respectively. The information on the mixtures is related to their location in Figure. The mixtures in the same columns have the same mix proportion, and the mixtures in the same row have the same preconditioning condition. The representative details of the nine mixtures in higher magnification are shown in Figure 5.3.6. The rule of arrangement of the mixtures is identical to that of Figure 5.3.5.

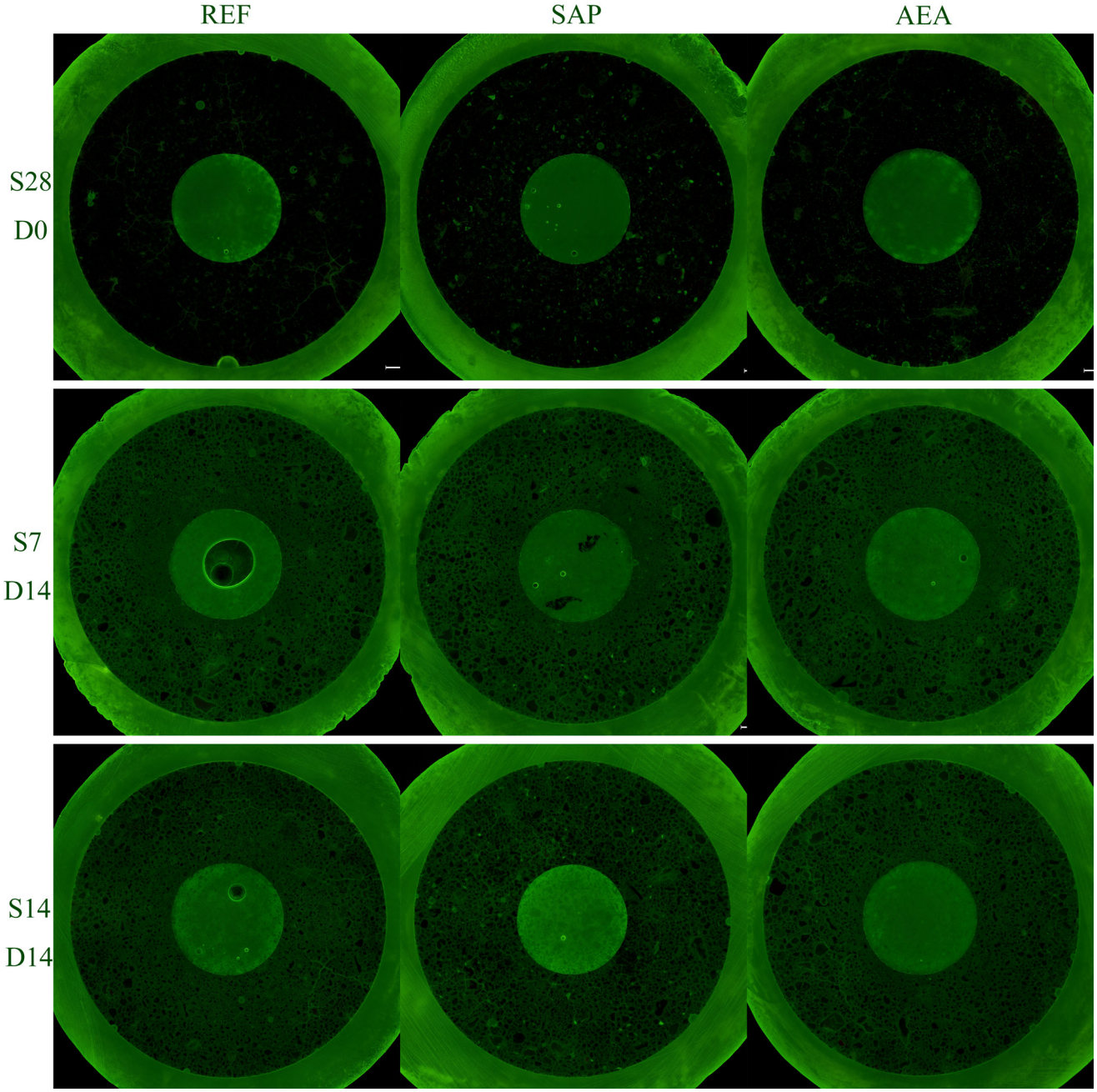

Figure 5.3.5 Overview of the test surfaces of all mixtures. Mixtures are arranged in 3 columns and 3 rows. The mixture information is indicated by its position in Figure. The samples in the same column have the same mix proportion (REF, SAP, AEA), while samples in the same row have the same preconditioning (S28D0, S7D14, S14D14). The size of each individual image is 35 mm × 35 mm

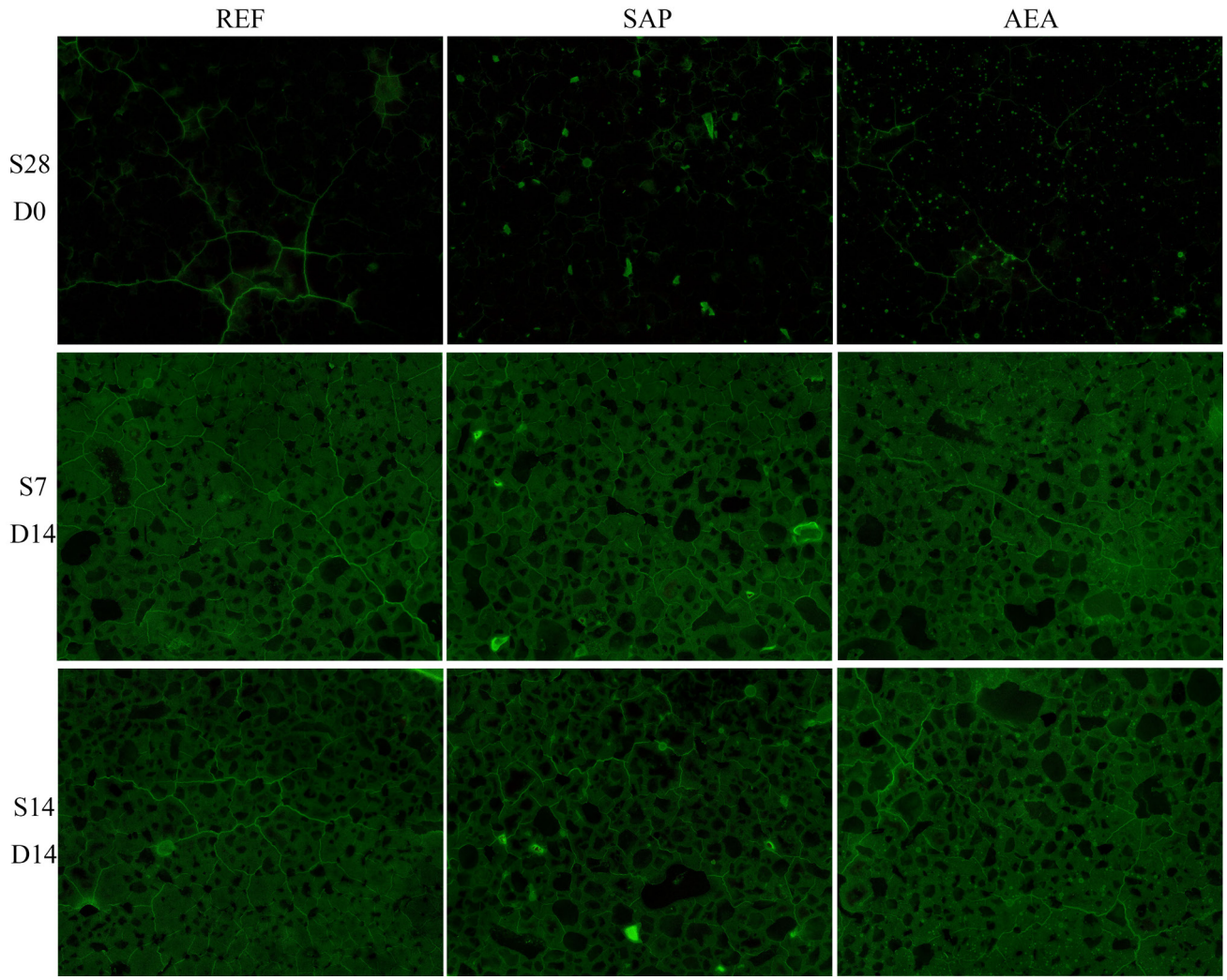

Figure 5.3.6 Representative high magnification details of all the mixtures. Samples are arranged in 3 columns and 3 rows. The mixture information is indicated by its position in Figure. The samples in the same column have the same mix proportion (REF, SAP, AEA), while samples in the same row have the same preconditioning (S28D0, S7D14, S14D14). The size of each image is 10 mm × 8 mm

5.3.6 Limitations

Three limitations need to be addressed for the discussion above.

- The effect of the mold used for molding. It is well known that the surface microstructure is influenced by the type of mold used in casting. In the study of this chapter, the influence was neglected. This is with the consideration of 1) all the mixtures were cast with the same type of mold; 2) the surface of a certain thickness was removed by grinding, which is most significantly influenced by the mold; 3) the objective of this chapter qualitatively evaluates the general trend, which is unlikely to be considerably influenced by the type of mold. Still, this should be addressed in the discussion: the extent of microcracking may be different when the casting is done by another type of mold.
- The creep and relaxation behavior of AASM. The discussion above is based on the assumption that all mixtures had the same creep and relaxation behavior. This is with the consideration of 1) the mix proportions are relatively similar; 2) the influence of SAP and AEA on the creep and relaxation behavior of AASM is unclear, and this is beyond the scope of this study; 3) to limit the complexity. However, it should be pointed out that SAP and

AEA are likely to have a certain influence on the creep and relaxation behavior of AASM, especially the SAP which had a considerable influence on the internal RH. Further study might be conducted on this topic.

- The microcracking caused by autogenous shrinkage. In the discussion above, it was stated in terms of surface microcracking caused by autogenous shrinkage. However, it should be noticed that the microcracking caused by the autogenous shrinkage might also exist inside the bulk body because autogenous shrinkage, unlike drying shrinkage, is an overall behavior of the samples. However, the characterization in this study was only conducted on the surface. Therefore, the discussion was limited to observation at the surface. But, it does not mean that the internal microcracking is only at the surface.

5.4 Observations and conclusions

In this chapter, the surface microstructure of AASM was studied by optical microscopy. Different preconditioning procedures (S28D0, S7D14, S14D14) were conducted on the samples in order to reproduce the surface condition in different tests. Vacuum impregnation with epoxy containing dye was conducted to enhance the difference among the cracks, aggregates, pores, and binder. The main observations in this chapter are:

- Very high surface microcracking potential was found in the AASM. The driving force behind this is attributed to the high autogenous shrinkage and drying shrinkage of AAS paste. Due to the restraining effect of the aggregates and shrinkage gradient, the restrained high shrinkage results in tensile stress in the paste, which generates microcracks.
- With the addition of SAP, the surface microcracking caused by autogenous shrinkage during sealed curing was significantly limited by internal curing. The extent of cracking caused by drying was also reduced by SAP, but the effect was much more limited.
- With the addition of AEA, only a slight improvement in surface integrity was found.
- A significant difference was found in the dye color intensity of AAS paste between the sealed mixtures and dried mixtures, indicating the much more porous microstructure on the surface of the dried sample compared to the samples sealed for 28 days. This observation raises concerns regarding the sample representativity and the sampling position.
- A denser AAS paste was found due to the benefit of internal curing provided by SAP. This also supports the finding and explanation regarding the higher compressive strength increment observed in SAP mixtures in chapter 3.
- Following the current surface scaling test protocol might induce a significant extent of surface microcracking on the AAS specimen due to the surface drying procedure.

The surface microstructure of AASM mixtures characterized in this chapter is crucial for the freeze-thaw resistance, especially the surface scaling resistance. This chapter provides valuable information for explaining the freeze-thaw performance of different AASM mixtures in chapter 6 as well as provided a strong rationale for further research on related subjects.

6 The freeze-thaw resistance of AAS and the influence of SAP / AEA

6.1 Introduction

The most traditional and commonly used method to improve freeze-thaw resistance is air voids entraining. The generated pressure during freeze-thaw cycles can be released and limited with the homogenously distributed entrained air voids, as discussed in chapter 2 [40, 84, 103]. In chapters 3 and 4, it was revealed that SAP and AEA are capable of entraining air voids in the AASM. Additionally, in chapter 5, it was found that a certain improvement in the surface condition of AASM was found with the addition of SAP or AEA. Therefore, an improvement in the freeze-thaw resistance of AASM by adding SAP or AEA is promising.

For the OPC binder system, the effect of AEA on freeze-thaw resistance has been quite thoroughly studied for many decades. In terms of SAP, there are also a number of available studies. However, when it comes to the AAS system, the relative study is scarce and unsystematic, especially in terms of surface scaling damage. Whether the observations and conclusions from the OPC binder system are still valid on the AAS binder system is remained to be answered. In addition, the effect of some controlling factors during SAP applications on freeze-thaw resistance is not thoroughly studied, such as the effect of SAP particle size distribution.

Accordingly, the objective of this chapter is to investigate the effects of SAP/AEA addition as well as the related designing factors on the surface scaling resistance of AAS by experiments. The investigation is first conducted on the mortar scale, then upscaled to the concrete scale for examination with the promising mix designs found in the mortar scale.

6.2 Materials and methods

6.2.1 Materials and mix proportions

6.2.1.1 Mortar scale

The raw materials characterized in Section 3.2.1 will still be used in this chapter. All the mixtures studied in chapter 4 will be involved:

- Reference:
  - REF
- SAP with different dosages:
  - SAP-15A, SAP-30A, SAP-45A
- SAP with different absorption compensations:
  - SAP-30A, SAP-30P, SAP-30N
- SAP with different sieved size distributions:
  - SAP-30A-F, SAP-30A-C

- AEA with different dosages:
  - AEA-010, AEA-020, AEA-030

6.2.1.2 Concrete scale

Based on the findings in the mortar scale test, the promising mixtures in the mortar scale will be upscaled to two normal strength alkali-activated slag concretes (AASCs). Factors such as dosage will remain unchanged. The two AASCs are referred to as concrete mix-1 (C1-REF) and concrete mix-2 (C2-REF). The C1-REF is a self-compacting concrete, while the C2-REF has a 50% substitution of coarse aggregates by recycled aggregate. The strength class of the C1-REF and C2-REF are C45/55. Due to the intellectual property issue, the detailed mix design cannot be shown.

The surface scaling resistance of C1-REF and C2-REF have already been tested before. Considering the availability of the freeze-thaw machine, and in order to investigate as many mixtures as possible, the previous data of the reference mixtures (i.e., C1/C2-REF) will be used.

6.2.2 Surface scaling test

6.2.2.1 Mortar scale

The freeze-thaw resistance of AASM will be studied in terms of surface scaling resistance. The test is conducted on the 160×40×40 mm^3 AASM specimens, and the bottom surface is used as the test surface. The test is conducted according to the CDF test (**C**apillary suction of **D**e-icing solution and **F**reeze-thaw test) [19, 20] with some adjustments for the characteristics of AAS.

The preparation of raw materials and mixing procedure are identical to that in the previous chapters. The preparation and preconditioning of specimens can be divided into curing and surface drying. After demolding, the AASM samples are sealed with multiple layers of plastic films and curd in a temperature control room at 20℃. After curing, the surface drying procedure is conducted in a climate-controlled room at 20℃ with a RH of 55%. The curing time for the specimens is 14 days, and the subsequent surface drying procedure also lasts for 14 days. On the day before the end of the surface drying procedure, the lateral surfaces of the specimens are sealed with bitumen adhesive aluminum tape, while the test surface and upper surface are kept free. This is to avoid the influence of lateral surfaces [148].

There are some modifications in the sample preparation compared to the standard CDF test. The conducted sealed curing is different from the underwater curing and moist curing described in the CDF test and ASTM C672 test. This is to avoid the potential adverse effects of water on early age AASM, such as leaching or increased porosity. This length for curing and surface drying is referred to ASTM C672 test instead of the CDF test, with the consideration of the sensitivity of AASM to the dry environment. The purpose of surface drying is to achieve hydric equilibrium between the specimen surface and the environment. With much smaller mortar specimens in this study, it is expected that 14-day surface drying can have a comparable extent of hydric equilibrium and less adverse effect due to drying. One might argue that a curing length of 14 days is a bit long and not a common case in reality. However, 14 days is not too long to be unrealistic.

The test procedure starts after the preparation and preconditioning procedures. Following the surface drying, the specimens are placed in a closed container on two stainless-steel bars with the test surface downwards. The test surface is submerged in the 3% sodium chloride test solution with a liquid level 5 mm above the test surface. The capillary suction period is seven days. Afterwards, the test surface is cleaned by the ultrasonic bath.

After the capillary suction, freeze-thaw cycles are applied. The setup in the capillary suction procedure is used. The temperature is automatically controlled by the test machine, and the temperature curve is shown in Figure 6.2.1. After 4, 6, 14, and 28 freeze-thaw cycles, the test container is bought to an ultrasonic bath for three minutes to remove the loosened scaled materials on the test surface. The test solution containing the scaled materials is then poured out and filtered. The containers are then put back into the machine with new test solutions for the subsequent freeze-thaw cycles. The filter papers containing the scaled materials are then brought to drying at 110 ℃ for 24 hours. After cooling down, the mass of the dried scaled materials and filter paper is weighted to 0.01 g. And the net weight of scaled materials is calculated by subtracting the mass of dry filter paper. Then, the scaling is the cumulative mass of scaled materials per unit area after specific cycles.

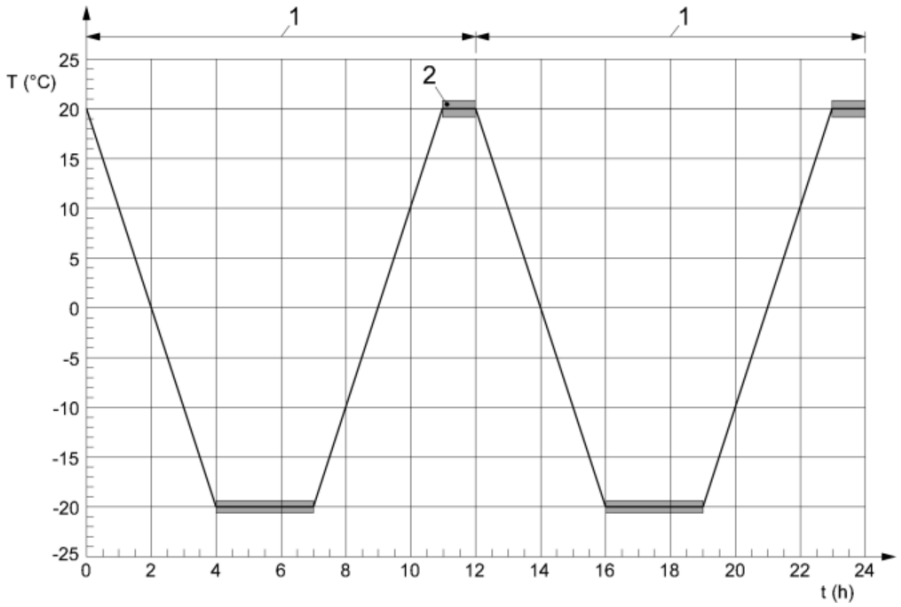

Figure 6.2.1 Temperature curve of freeze-thaw cycles, where: 1- one freeze-thaw cycles; 2- test window for collecting scaled materials

For each mixture, the surface scaling resistance is tested with four 160×40×40 mm^3 prism specimens. Two containers are used, and each container contains two prism specimens. The surface scaling of a mixture is the average of the scaling from two containers (e.g., two duplicates). The scaling for each container is calculated by the total scaled materials from two specimens and the total test area (e.g., 2×160×40×40 mm^3).

6.2.2.2 Concrete scale

For the surface scaling test in concrete scale, in order to make use of previous data, the test procedure followed identically with the previous test. After demolding, the specimens are bought to a moist room with a RH at 100%. The specimens are covered by a layer of plastic film to prevent the specimens from direct contact with spraying moist.

After curing, the concrete specimens are bought to surface drying until 28 days at 55% RH. For C1-REF, the curing time is 14 days, while for C2-REF, the curing time is 7 days.

After surface drying, the surface scaling test is conducted according to the CDF test described in the standard [19]. In contrast to the mortar scale, five duplicates are tested due to the relatively high deviation.

6.3 Surface scaling resistance of AASM without admixture

Figure 6.3.1 shows the performance of the reference mixture during the surface scaling test. The cumulative scaling of REF quickly developed to around 2.95 kg/m^2 within the first 6 freeze-thaw cycles. And a cumulative scaling of 5.89 kg/m^2 was found at the end of the test.

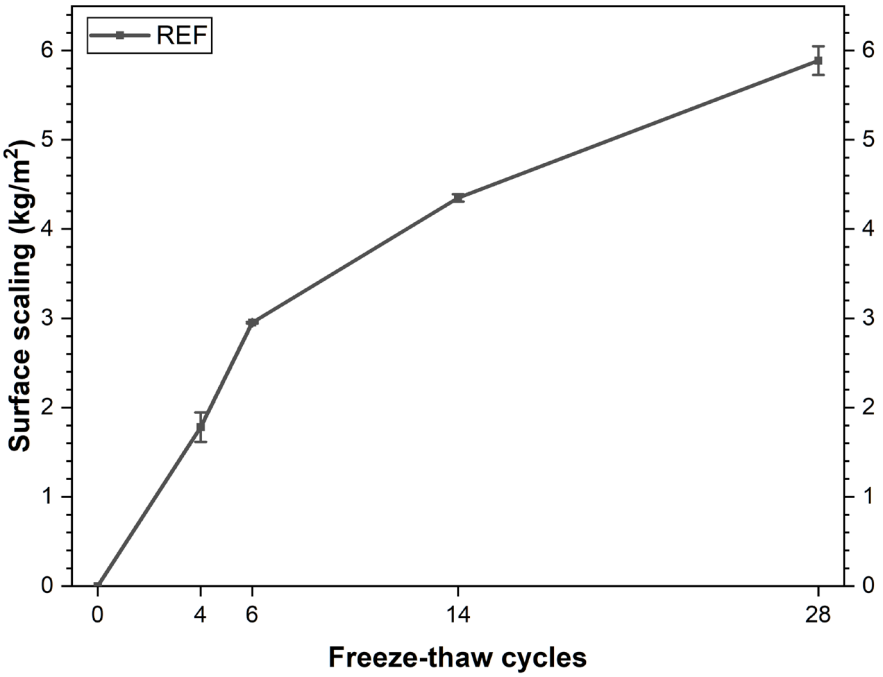

Figure 6.3.1 Surface scaling of REF AASM

Figure 6.3.2 Surface condition of an AASM during the CDF test, from left to right: 4 cycles, 14 cycles, 28 cycles. Adapted from [66].

The surface condition during the freeze-thaw cycles is indicated in Figure 3.6.2 [66]. With the current test protocol, it seems that the history of surface scaling can be roughly divided into two periods by the timing at 6 cycles. The first period consists of the initiation of defects at the surface, scaling of the paste at the surface, with gradual exposure of coarse aggregates. The speed of scaling during this period is relatively fast. In the later stage, the scaling of paste develops, and exposure of coarse aggregates continuously increases. As shown in Figure 3.6.1, the speed of scaling is slowed down in the later stage. The lower speed is attributed to two reasons. One is the decreasing fraction of paste on the test surface due to the increasing extent of coarse aggregates exposure. Most of the scaled materials are AAS paste, and the loss of aggregates is limited unless the surface scaling goes extremely serious, as shown in Figure 6.3.3, where a scaling around 13 kg/m^2 was found at the end of the test. Another cause behind the lower speed is that the internal AAS matrix is stronger than the AAS matrix at the surface due to the effect of drying [29].

Figure 6.3.3 An AASM with an extreme extent of scaling of around 13 kg/m^2 at the end of the CDF test due to the exposure to 55% RH ambient air after demolding. Adapted from [66].

As shown in Figure 6.3.1, a considerable extent of surface scaling was found in the reference AASM. A cumulative scaling of 5.89 kg/m^2 at the end of the test, which is considerably higher than the suggested limit of 1.5 kg/m^2. Even though this recommended limit is defined for concrete scale, the considerable excess still implies that the AAS system has poor surface scaling resistance. The poor surface scaling conforms to the literature [12, 13]. Although this point is not systematically investigated in this study, some discussion and susception can be made.

The high microcracking potential at the surface, as shown in chapter 5, undoubtedly holds major responsibility for the poor surface scaling. On the sample sealed and cured for 28 days, obvious microcracking can be recognized because of autogenous shrinkage. For the samples that underwent preconditioning described in the surface scaling test protocol, a significant extent of map microcracking was found due to the autogenous shrinkage as well as drying shrinkage. From the perspective of hydraulic pressure theory, crystallization theory, and critical degree of saturation theory, such an extent of microcracking promotes the ingress of water, and the amount of freezable water during the freeze-thaw cycles is considerably higher. From the perspective of glue-spall theory and fracture mechanics, for an intact surface, the criterion of damage initiation is the exerted pressure exceeds the tensile capacity of the matrix. With the pre-existing surface microcracking, the flaws are already pre-initiated, and this criterion is significantly lowered or even automatically satisfied. From the perspective of fracture mechanics, the energy needed for flaw propagation is much lower than the energy to damage the intact compound due to the stress concentration. In other words, the damage is more significant.

With the pre-existing microcracks, additional impelling force is also created by the liquid in the microcracks as a result of the volume expansion during freezing, as well as the mismatch in CTE between ice and matrix after freezing. A schematic is shown in Figure 6.3.4,

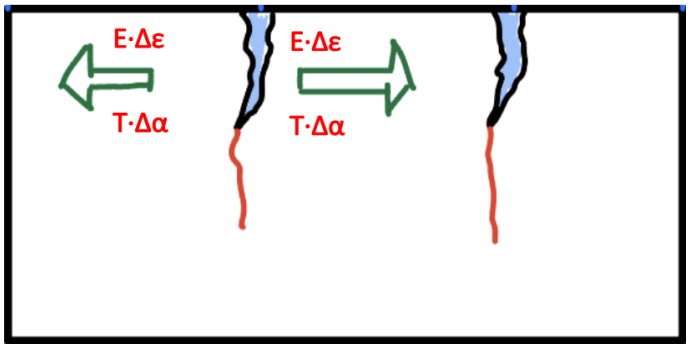

Figure 6.3.4 Schematic of the additional impelling force when the preexisting microcracks are present.

In addition to the surface microcracking, the microstructure might also contribute. AAS binder has the characteristic of dense microstructure with high portions of mesopores [2, 130], which is generally believed to be beneficial to surface scaling resistance. However, generated pressure during freeze-thaw cycles is inversely proportional to the pore radius. The influence of pore radius is a competition between the lower water ingression and the higher generated pressure. In terms of surface scaling, the positive aspect seems to be larger in the OPC system. While in the AAS system, with further denser microstructure, it might be the case that the generated pressure is intolerable and cannot be compensated by the lower water ingression.

Another possibility is that the microstructure of AASM at the surface is far more porous than cognition, especially after drying. As discussed in chapter 5, a much more porous microstructure was found in the microstructure of dried AASM than in sealed AASM. However, most of the pore structure characterization used samples taken from the internal bulk body of properly cured specimens. In terms of durability issues concerning the surface, this might lead to a misperception of the actual microstructure. For the surface scaling test, it has been shown that the microstructure at the surface of AASM underwent preconditioning described in test protocols is very different from the 28-day properly cured counterpart. And the poor surface scaling of AASM might be due to the previously ignored porous microstructure at the surface.

To be summarized, poor surface scaling was found in the AASM without admixture. The poor resistance is mainly attributed to the pre-existing surface microstructure, and the pore structure might also contribute.

6.4 Surface scaling resistance of AASM with SAP

6.4.1 Effect of SAP on surface scaling resistance of AASM

Figure 6.4.1 shows the surface scaling of AASM with or without the addition of SAP in relation to the number of underwent freeze-thaw cycles. With the addition of SAP, considerable improvement was found in the surface scaling resistance of AASM. Compared to REF, many mixtures with SAP showed approximately a 50% reduction in cumulative surface scaling at the end of the test. Mixture SAP-30A-F exhibited the best surface scaling resistance, with a cumulative scaling of 0.79 kg/m^2 after 6 freeze-thaw cycles and 2.25 kg/m^2 at the end of the test.

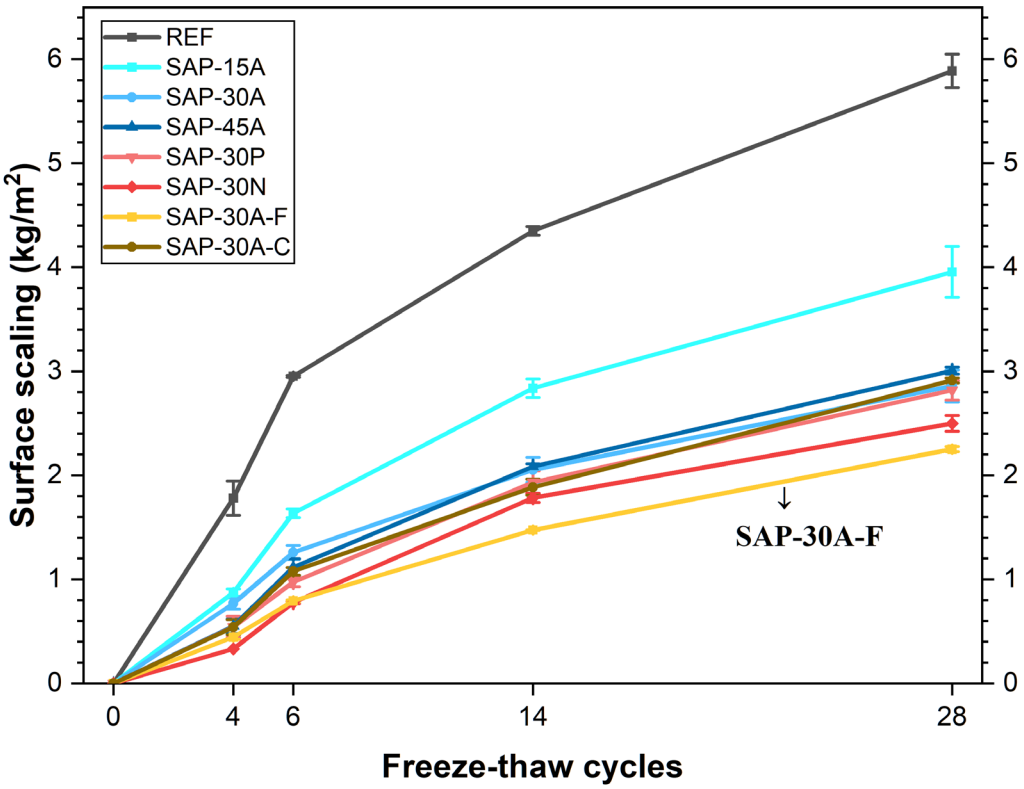

Figure 6.4.1 Surface scaling of AASM with or without the addition of SAP

The observed improvement is attributed to two aspects: the entraining of air voids and the improvement in surface condition.

As investigated in chapter 4, SAP successfully created air voids in the AASM. The effect of the entraining air voids on the freeze-thaw resistance of cementitious materials has been quite thoroughly investigated in literature and discussed in chapter 2 [40, 84]. During freezing, the volume expansion of ice pushes the pore liquid away and generates hydraulic pressure. The presence of entrained empty air voids allows the pore water to move in, and the generated hydraulic pressure is released and limited [38, 40]. The water flowing into the air voids freezes on the wall, sucks water from the pores, and causes contraction of the matrix [81, 84]. Poromechanical analysis showed such a contraction not only compensates caused by the expansion of ice but also results in a net contraction on the matrix [40, 85]. Such a contraction protects the matrix and also compensates for the mismatch in CTE, which generates cracks according to the glue-spall theory [40]. In terms of the critical degree of saturation, the entrained air voids can significantly increase the required time for the degree of saturation to reach the critical level [35].

The discussion above is analyzed based on the OPC system with AEA for the addition of SAP or on the system of AAS. A difference between the air voids created by SAP and AEA is that, after releasing the absorbed liquid, the SAP particles will attach to the wall of air voids, as shown in Figure 6.4.2. From this perspective, when the pore water flows into the air voids, some of the water might be aborded by the remained SAP particles instead of freezing into a sphere crystal. Nevertheless, the consequence is similar. The remained SAP particles can also suck the water from the pores and result in the contraction of the matrix.

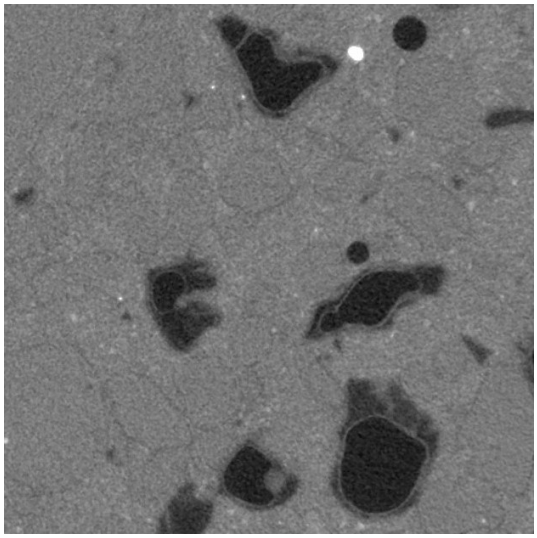

Figure 6.4.2 Air voids created by SAP particles after releasing (part of) the absorbed liquid

More fundamental research is needed for the behavior of SAP during freeze-thaw cycles and the related effect. These are very interesting, but unfortunately, they are not covered by the scope of this study.

6.4.2 Mixtures with different SAP dosages

Figure 6.4.3 shows the surface scaling test results of REF and AASM with varying dosages. The addition of SAP successfully improved the surface scaling resistance. SAP-15A, with the lowest dosage of 0.15% BWOS created an approximately 33% reduction in scaling materials at the end of the test. Increasing the SAP dosage to 0.30% further reduced the total cumulative scaling to 49%. However, no additional improvement was found when further increasing the SAP dosage to 0.45%. SAP-30A and SAP-45A showed very similar performance during the test. It seems that the surface scaling resistance of AASM does not simply increase with increasing SAP dosage.

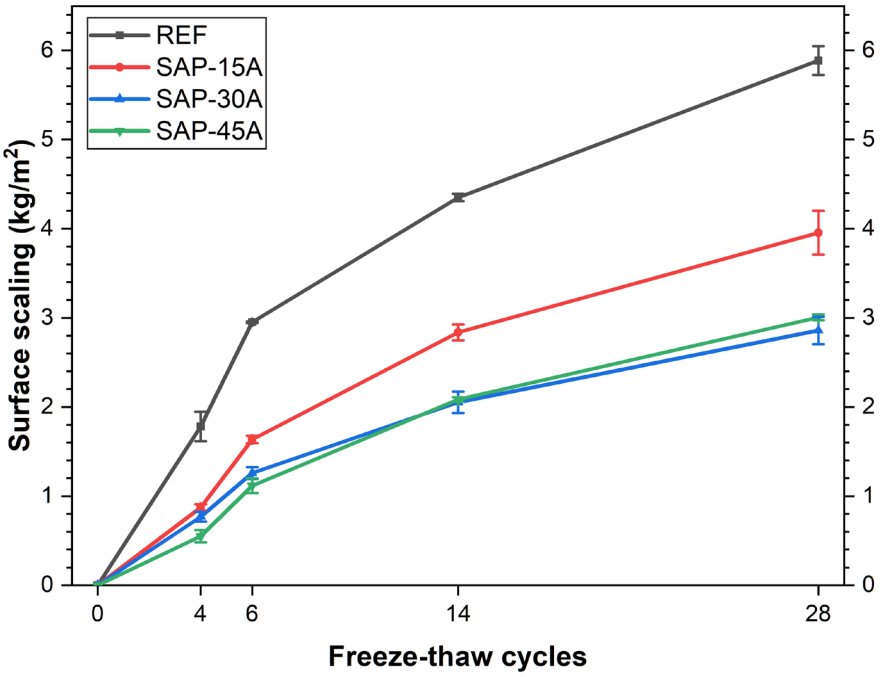

Figure 6.4.3 Surface scaling of REF and AASM with SAP dosage of 0.15%, 0.30%, and 0.45% BWOS

As discussed above, the contribution of the addition of SAP is in two aspects, one is entraining air voids, and the other is reducing surface microcracking, especially the cracking caused by autogenous shrinkage.

From the perspective of surface microcracking, autogenous shrinkage, and drying shrinkage are believed to be the driving forces. In terms of autogenous shrinkage, the autogenous shrinkage of AASM will not be fully eliminated by the addition of SAP, even when the internal RH is very close to 100% by high SAP dosage [91]. In such a case, the extent of autogenous shrinkage will not further decrease with increasing SAP dosage [91]. This is because the pore pressure created by self-desiccation is not the only mechanism behind the autogenous shrinkage of AAS [91, 140]. In terms of drying shrinkage, SAP only has a limited effect. Therefore, in this case, it is likely that increasing the SAP dosage from 0.30% to 0.45% will not further improve the surface condition of AASM.

From the perspective of air void entraining, SAP-30A indeed had a higher entrained air content compared to SAP-45A, as shown in chapter 4. As a result, the spacing factor of SAP-45A was also smaller than SAP-30A. Considering the relatively low entrained air content in SAP-30A and SAP-45A, in terms of air voids entraining, the SAP-45A should have better performance than SAP-30A.

However, reducing the shrinkage and entraining air voids are not the only effects of the addition of SAP. The SAP also influences the capillary pore system. Although the overall capillary porosity is more dependent on the effective water/cement ratio instead of the total water/cement ratio [107], the local porosity of the matrix is likely to change depending on the distance from the SAP [96, 149, 150]. An over-average porosity is found within a distance of around 100 um [149, 150]. This influenced area is more vulnerable to freeze-thaw cycles. And with a higher dosage of SAP, a higher influenced area can be expected. In addition, as shown in chapter 4, the air-void system created by SAP is relatively not closely distributed. Compared to the air-void system created by AEA, the air-void spacing of SAP mixtures is several times higher. It can be imaged that, in the fresh AASM, SAP particles cannot absorb the liquid in the distance but only in the surrounding area. For the matrix that has a high distance to SAP particles, the local water/binder ratio is closer to the total water/binder ratio, i.e., higher than 0.39 and higher with increasing SAP dosage (0.43 vs. 0.45 for SAP-30A vs. SAP-45A). And the resultant local porosity is higher and more vulnerable to the freeze-thaw cycles.

Thus, the effect of increasing the SAP dosage might be a competition between higher entrained air voids content and more local porous microstructure. In this case, SAP-30A has a lower air voids content but a relatively denser local matrix, while SAP-45A had a higher air voids content but a relatively more porous local matrix. And the resultant surface scaling of these two mixtures is similar.

In addition, for the cause behind the observed trend, the possibility of human error is unlikely to happen, but the possibility of random error cannot be excluded. It might be doubted whether some human mistake was made on controlling the SAP dosage during the mixing. However, a clear difference can be found in the air-void system, as shown in chapter 4. Since the samples used in the micro-CT scan were prepared under the same batch as specimens used in the freeze-thaw test, human error is unlikely. However, in terms of random error, the surface scaling test had the characteristic of relatively poor reproducibility and high deviation of the surface scaling test [100]. The SAP-30A and SAP-45A were not in the same test batch, and random errors might lead to a similar performance.

6.4.3 Mixtures with different SAP absorption compensation methods

The surface scaling test results of REF and AASM with different SAP absorption compensation methods are shown in Figure 6.4.4. At the end of the test, all mixtures showed relatively similar cumulative scaling with a reduction of approximately 45%.

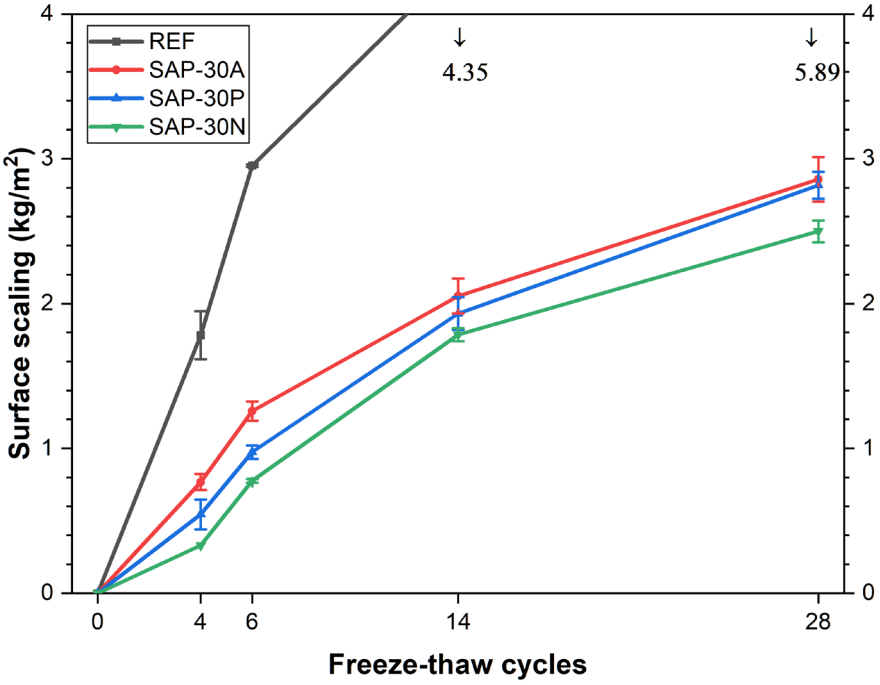

Figure 6.4.4 Surface scaling of REF and AASM with different SAP absorption compensation methods, where A-dry mixing SAP with the additional amount of activator; P-prewetting SAP win the additional amount of activator; N-dry mixing SAP with the original amount of activator

Compared to the SAP-30A, within the first period (i.e., 0 – 6 freeze-thaw cycles), noticeable further improvement can be found in the SAP-30N, which did not have the additional activator. The difference gained in the first periods remained unchanged with the increasing freeze-thaw cycles. The better surface scaling resistance observed in the SAP-30N is attributed to the lower equivalent water/binder ratio. As mentioned above, the capillary pore system depends on the equivalent water/binder ratio [107]. Due to the absorption of SAP particles, the SAP-30N has the lowest equivalent water/binder ratio of 0.35. As a result, the SAP-30N has a denser microstructure compared to REF and SAP-30A/P. With the denser microstructure, there is a lower amount of water ingression and better freeze-thaw resistance.

SAP-30A and SAP-30P had the additional activator, i.e., a similar equivalent water/binder ratio. As a result, the capillary pore structure of SAP-30A and SAP-30P are very similar. At the early stage of the freeze-thaw test, the SAP-30P performed slightly better than SAP-30A. This might be attributed to the greater extent of swelling, which resulted in a slightly better surface condition. At the end of the test, a very similar cumulative surface scaling of approximately 2.8 kg/m^2 was found.

In general, the different SAP absorption compensation methods included in this study only showed limited influence on the surface scaling resistance, especially when the equivalent water/binder ratio is the same.

6.4.4 Mixtures with different SAP particle size distributions

Figure 6.4.5 shows the surface scaling behavior of AASM with the same SAP dosage but different SAP particles size. A considerable difference in the air-void system has been revealed in chapter 4. As a result, an obvious difference was also found in surface scaling resistance. AASM with coarse particle size showed similar performance compared to SAP-30A, which is not sieved. The total cumulative scaling of SAP-30A-C was around 2.9 kg/m^2. On the other hand, with finer SAP particles, the final cumulative scaling of SAP-30A-F was further reduced to approximately 2.2 kg/m^2. And it gave the best surface scaling resistance among all the mixtures.

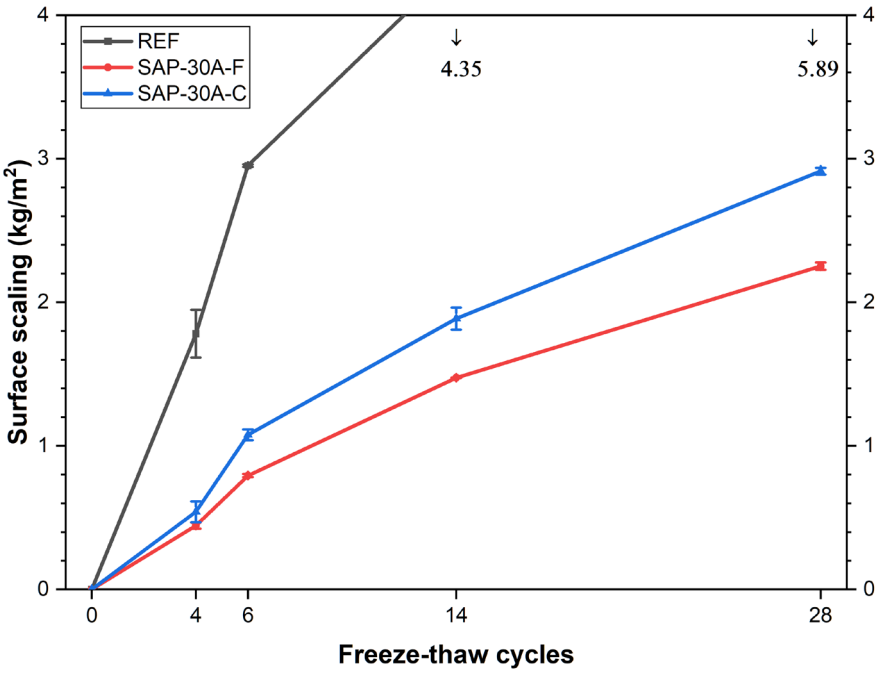

Figure 6.4.5 Surface scaling of REF and AASM with different SAP particle size distribution, where F-sieved fine SAP particles remain on screen 125 – 250 um; C-sieved coarse SAP particles remain on screen 250 – 500 um

This further improvement in SAP-30A-F is attributed to the higher amount of SAP particles. The dosage of the SAP is controlled by the mass. With smaller particle size distribution, a higher amount of SAP particles was added into AASM, and the closer distribution of entrained air voids, i.e., air voids spacing. It is widely observed and agreed that the lower the spacing factor, the higher the freeze-thaw resistance, as shown in Figure 2.5.4 [27]. With the closer distribution, the flow distance of the water during the freeze-thaw cycles is lower. As a result, there is a lower generated hydraulic pressure and a higher freeze-thaw resistance.

From the perspective of internal curing, finer SAP particle size distribution is also more favorable [107]. This is attributed to the higher surface specific area and closer distribution. The difference might be more significant in this case because the curing ended at 14 days. With the higher surface specific area, the release of absorbed liquid is likely to be faster in finer particles, which leads to a higher degree of reaction at the early age. A piece of evidence can be found in section 3.5.1, where the compressive strength increment from 7 days to 28 days of SAP-30A-F is the lowest one among all the mixtures.

Therefore, with the smaller SAP particle size distribution, there is a smaller flow distance for the pore water during freeze-thaw cycles and a better internal curing effect of AASM. As a result, the surface scaling resistance is higher.

6.5 Surface scaling resistance of AASM with AEA

The surface scaling test results of REF and AASM with different dosages are shown in Figure 6.5.1. With the addition of AEA, the surface scaling of AASM was improved to a certain extent. At the end of the test, a 30 – 40% reduction in cumulative scaling of AASM can be observed from the AASM with AEA. Dosages of 0.01% and 0.02% BWOS gave generally similar surface scaling curves during the freeze-thaw test. When further increasing the AEA dosage to 0.03%, a slightly further improvement was found. It seems that the addition of AEA gave a similar extent of improvement until the dosage reached 0.03% BWOS. Beyond which dosage, a further improvement in surface

scaling might be expected. However, a relatively high deviation was found in the results, especially in the mixture of AEA-010 and AEA-020. This unstable performance makes it difficult to make a solid conclusion on the general trend between the dosage of AEA and the AASM surface scaling resistance. On the other hand, the high deviation also implies that some other factors of high randomness were influencing the surface scaling resistance. Based on the available information and discussion above, this might be the surface microcracking.

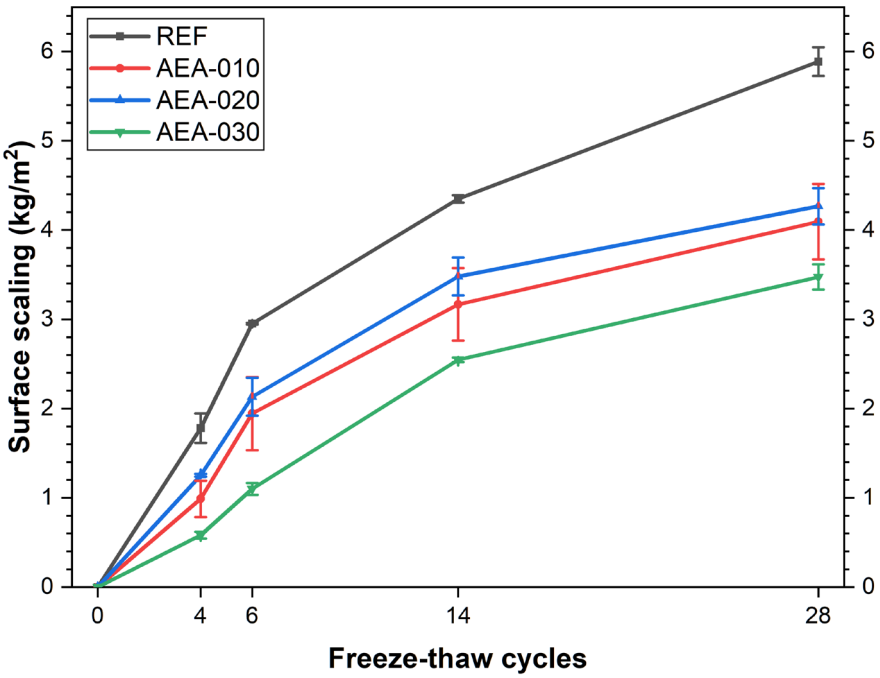

Figure 6.5.1 Surface scaling of REF and AASM with different AEA dosages of 0.01%, 0.02%, and 0.03% BWOS

In the OPC system, the addition of AEA considerably reduced the surface scaling. In this study, only limited improvement was found in the study. Such a different performance and its underlying cause are very interesting and meaningful. The entrained air content of AAS with the addition of AEA was in the range of 7% to 15%. Based on the experience from the OPC system, it is unlikely that the air content is insufficient [35, 38]. In addition, the flow distance characterized in chapter 4 also indicated that the air-void system in the hardened AASM created by AEA is sufficient. As shown in Figure 4.3.17, for the AEA dosage of 0.01 – 0.03 %, the d_{50} ranged from 69 to 114 um while d_{90} ranged from 183 to 240 um. Considering the suggested spacing factor is around 250 um, even the lowest AEA dosage mixture AEA-010 should considerably reduce the surface scaling. Thus, it is concluded that, in this study, air training by AEA is adequate, but it only leads to limited improvement in the surface scaling of AASM. This observation suggests that some other factors that did not be improved by AEA played a significant role in determining the surface scaling resistance.

Based on the available information, this significant factor is still attributed to the surface microcracking. Comparing the addition of SAP and AEA, the air-void system created by SAP has a lower air content and a twice flow distance. However, mixtures with SAP generally showed better surface scaling resistance than AEA mixtures. As discussed above, the contribution of SAP is attributed to two aspects: entraining air voids and improving surface conditions. Considering SAP mixtures had a poorer air-void system but better surface scaling resistance, it can be easily deduced that the improvement in surface condition had considerable significance.

To summarize, adequate air-entraining by AEA only resulted in a limited improvement in the surface scaling resistance of AASM. The extent of improvement by AEA is considerably lower than that found in the OPC system. The surface scaling performance of AASM with AEA is not satisfactory but confirms the significant role of surface microcracking in surface scaling.

6.6 Relation between surface scaling resistance and air-void system

Entrained air content, air void spacing, and specific surface area are the three most commonly used air-void system parameters to characterize the entrained air-void system. And these parameters are reported to have a good correlation to the freeze-thaw resistance, especially the air voids spacing which directly bridges with the generated pressure. In this section, the relationship between the freeze-thaw resistance and air-void system parameter will be discussed. Both the air-void system created by AEA and SAP was characterized in chapter 4. However, based on the surface scaling results discussed above, it is obvious that they cannot be compared together. Considering the relatively large scattering in AEA mixtures, only the air-void system created by SAP will be discussed in this chapter.

Among the entrained air content, air voids spacing, and specific surface area, entrained air content is the easiest to test, but its correlation to freeze-thaw resistance is relatively poorer than the other two because it neglects many influencing factors. Figure 6.6.1 shows the relationship between entrained air content and the cumulative scaling at 28 freeze-thaw cycles. It can be observed that the surface scaling resistance of AASM generally increased with increasing air content but seemed to reach a plateau after 5%. The possible causes have been discussed in section 6.4.1.2.

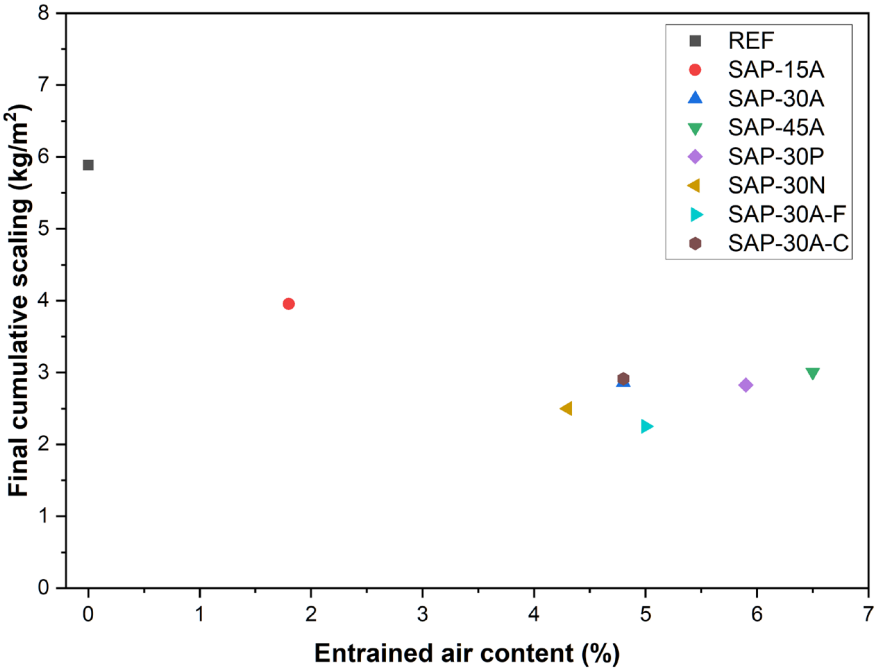

Figure 6.6.1 Relation between the total cumulative scaling at 28 freeze-thaw cycles and the entrained air content of REF and SAP mixtures

The specific surface area is not qualitatively characterized in chapter 4, but is addressed by different particle size distributions' SAP. As shown in section 6.4.4, with finer SAP particles, i.e., higher specific surface area, the surface scaling resistance was higher. This is due to the higher amount of air voids and lower flow distance.

The air voids spacing has a relatively solid theoretical correlation to the resultant freeze-thaw resistance [27, 38], and it is characterized by the parameter flow distance in this study. Figure 6.62 shows the relationship between the flow distance d_{50} and the total cumulative scaling at 28 days. A relatively good correlation was found. The surface scaling is lower with a lower d_{50}.

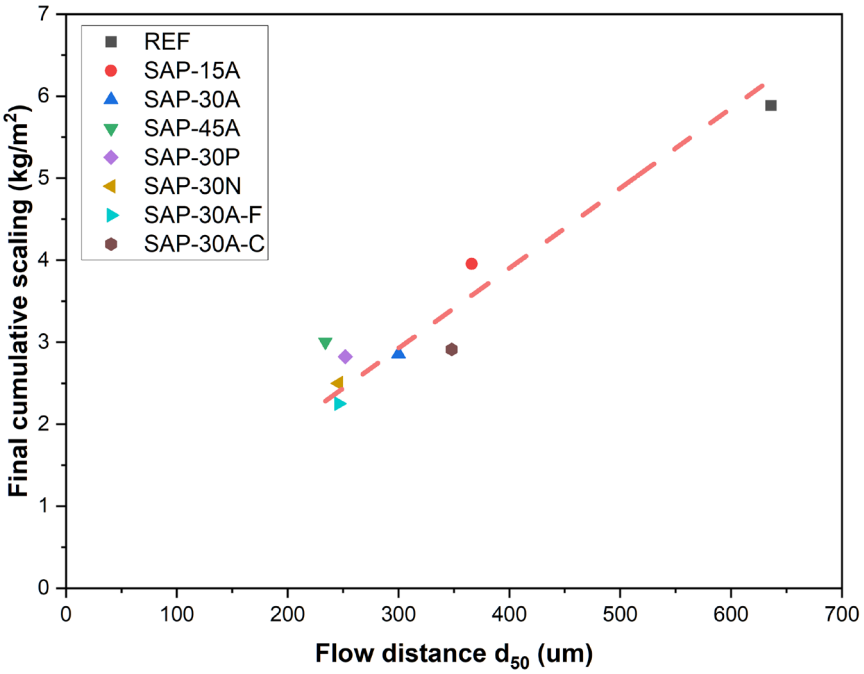

Figure 6.6.2 Relation between the total cumulative scaling at 28 freeze-thaw cycles and the flow distance d_{50} of REF and SAP mixtures

In general, the surface scaling resistance increases with higher entrained air content, specific area, and flow distance. The trends are generally in line with the observation in the OPC system. However, solely predicting the surface scaling resistance by the air voids system will be insufficient because SAP has many other effects in the AASM, such as reducing shrinkage and changing the water/binder ratio. The influence of these aspects is not reflected in the air-void system but does have an influence on the resultant surface. To predict the surface scaling resistance when the SAP is applied, a numerical model might be needed to bridge the surface scaling resistance and the factors influenced by SAP, such as water/binder ratio, air-void system, reaction kinetics, etc. For this purpose, the limited data in this study might not be enough. Nevertheless, a preliminary model is built to give some inspiration for further research.

6.7 Preliminary model for predicting the reduction in surface scaling

In this section, a preliminary model is proposed for predicting the reduction in surface scaling of AASM with the addition of SAP. The model considers the effect of SAP on capillary pore structure, air content, air voids size distribution, and flow distance, and bridges these factors to the resultant total cumulative surface scaling.

To consider the effect of adding the additional amount of activator to compensate for the SAP absorption, the equivalent water/binder ratio w_{eq}/b is involved in the model. The equivalent water/binder ratio w_{eq}/b was reported to determine the capillary pore structure [107]. With higher w_{eq}/b, the matrix has a more porous capillary pore structure and a poorer resultant surface scaling resistance. In other words, the w_{eq}/b is in inverse correlation to surface scaling. The value of w_{eq}/b is shown in section 2.4.2, where the mix design is shown in detail.

The difference in air content and air voids size distribution of different mixtures is evaluated by the factor K_1, which is calculated as the slope of linear regression results of the cumulative air content versus the equivalent radius of air void r_{eq}, as shown in Figure 6.7.1. The calculated factor K_1 and r^2 are summarized in Table 6.7.1.

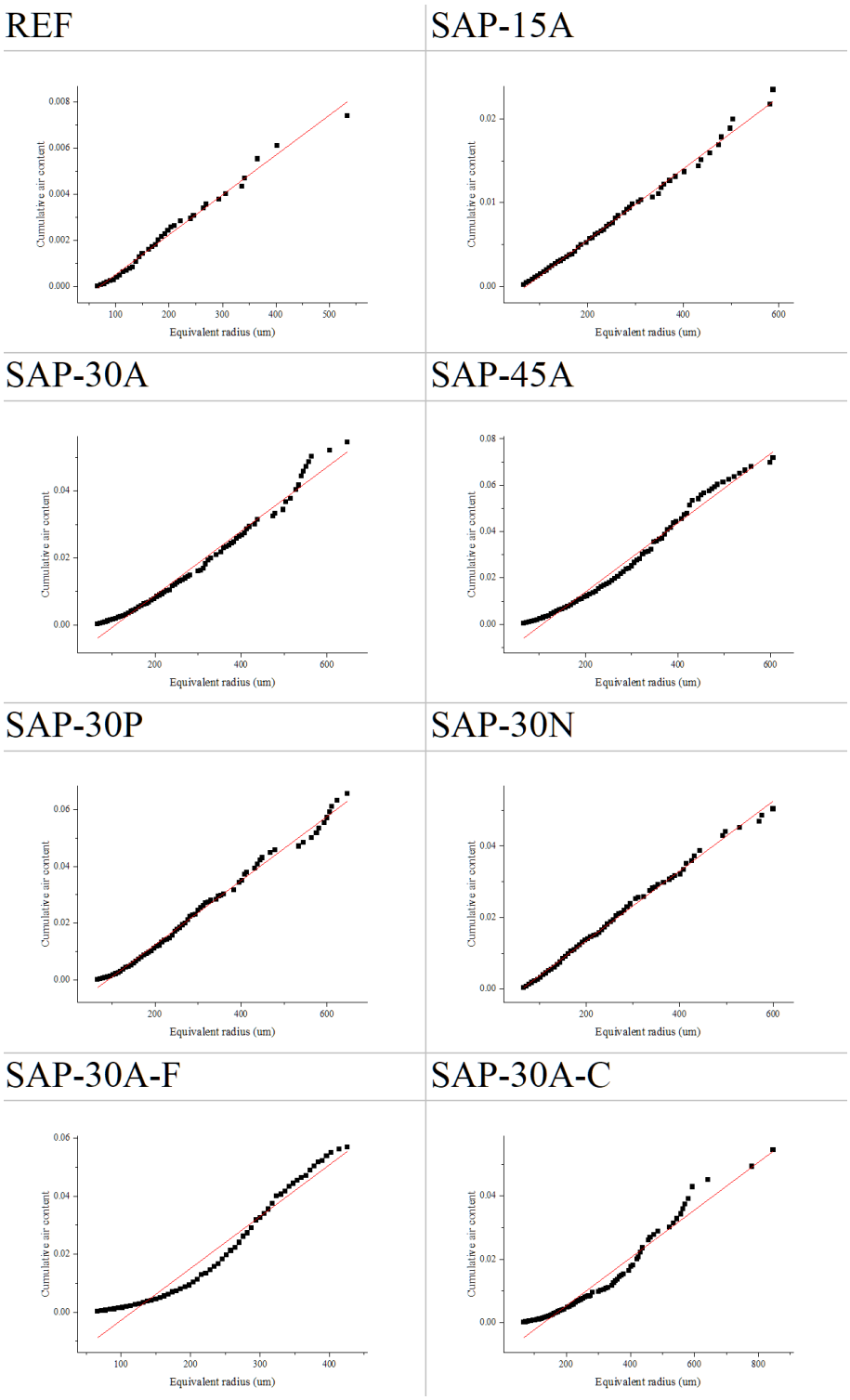

Figure 6.7.1 Linear regression of cumulative air content versus air void equivalent radius

By the slope (i.e., factor K_1), the difference in the air content and pore size is quantified. With higher air content and finer equivalent radius r_{eq}, the slope K_1 is higher. Meanwhile, the surface scaling resistance is higher with higher air content and closer air voids size distribution (i.e., SAP particle

size distribution), as discussed in section 6.5. Therefore, the factor K_1 positively correlates to the surface scaling resistance.

Table 6.7.1 Linear regression result of the relation between cumulative air content and equivalent pore radius.

	K_1	r^2
REF	1.73	0.99
SAP-15A	4.26	0.99
SAP-30A	9.57	0.98
SAP-45A	14.90	0.98
SAP-30P	11.26	0.99
SAP-30N	9.76	0.99
SAP-30A-F	17.87	0.95
SAP-30A-C	7.55	0.96

The difference in air voids spacing (i.e., flow distance) of different mixtures is evaluated by the d_{50} characterized in chapter 4. As discussed in section 6.5, the surface scaling resistance increases with a lower flow distance. In other words, the factor d_{50} is in inverse correlation to the surface scaling resistance.

In this way, the difference in capillary pore structure and the air-void system is roughly quantified. Due to the lack of an available model, the surface scaling resistance R is tentatively estimated by multiplying the factors based on their correlation to surface scaling resistance:

$$R = \frac{1}{(w/b)_{eq}} \cdot K_1 \cdot \frac{1}{d_{50}}$$

The relation between the total cumulative surface scaling and surface scaling resistance is plotted in Figure 6.7.2. A strong correlation is found between the surface scaling reduction and the calculated resistance R. To predict the trend, a logarithmic equation is used to fit the data points:

$$y = a - b \cdot \ln(R + c)$$

The regression curve is shown in Figure 6.7.2. It seems that the logarithmic model can have a good prediction on the trend of the surface scaling resistance provided by SAP, with a r^2 = 0.93. The reduction in surface scaling quickly increases at the beginning, i.e., low SAP dosage. This might be attributed to the effect of internal curing of SAP, which leads to a considerable reduction in autogenous shrinkage and the resultant surface cracking. After a certain R, when the dosage of SAP reaches 0.30%, the increment of reduction is gradually slowing down. This might be because the dosage of SAP is high enough and the effect of reducing autogenous shrinkage reaches the plateau, and no further improvement can be offered [91]. And the improvement in this stage is mainly attributed to the entrained air voids and the limited effect of reducing drying shrinkage [147]. Based on the logarithmic model, it seems to be hard to eliminate most of the surface scaling like OPC. This might be due to the surface microcracking caused by drying, as discussed in chapter 5. From this perspective, it might be improved by prolonging the curing time before the surface drying. Unfortunately, this factor did not fall into the scope of this study.

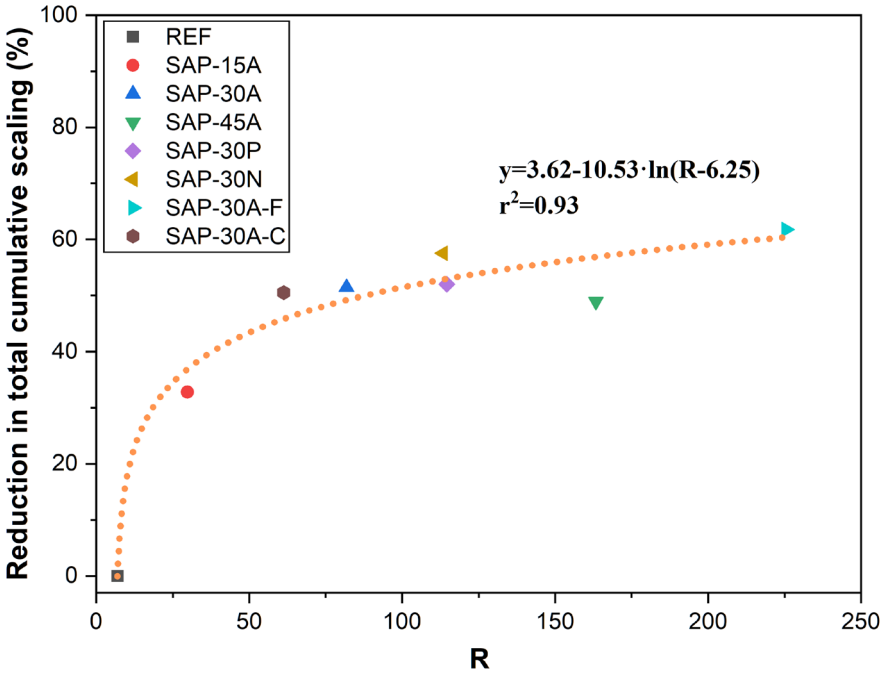

Figure 6.7.2 Relation between the reduction in total surface scaling and the calculated resistance factor *R*. The trend is predicted by a logarithmic model

Because developing a prediction model did not fall into the scope of the study at the beginning, the available data is limited and not very systematic. The range of the variable was relatively small while the interval was relatively high. And factors such as the degree of reaction of slag and the extent of surface cracking were not quantified by experiments, while they probably can improve the developed model. Nevertheless, it seems that the proposed logarithmic model does have a good correlation with the data. This is inspiring and provides a strong rationale and starting point for pursuing the further investigation.

6.8 Improving surface scaling resistance of AASC by SAP

Based on the test results from the mortar scale, the performance of SAP is much better than AEA. Therefore, the surface scaling resistance of AASC with or without the addition of SAP will be investigated. Considering the availability of the freeze-thaw machine, the SAP mixtures are C1-SAP-30A for concrete mix-1 and C2-SAP-30A/45A for concrete mix-2.

Figures 6.8.1 and 6.8.2 show the surface scaling test results for concrete mix-1 and concrete mix-2, with or without adding SAP. Results show that adding SAP increased the surface scaling resistance of both concrete mix-1 and mix-2.

For concrete mix-1, significant scaling was found in the reference mixture, with a total cumulative surface scaling reaching around 6 kg/m^2 at the end of the test. By adding 0.30% SAP BWOS, mixture C1-SAP-30A showed a reduction of more than 50% in the total cumulative scaling. This extent of improvement is similar to that of OPC concrete [90].

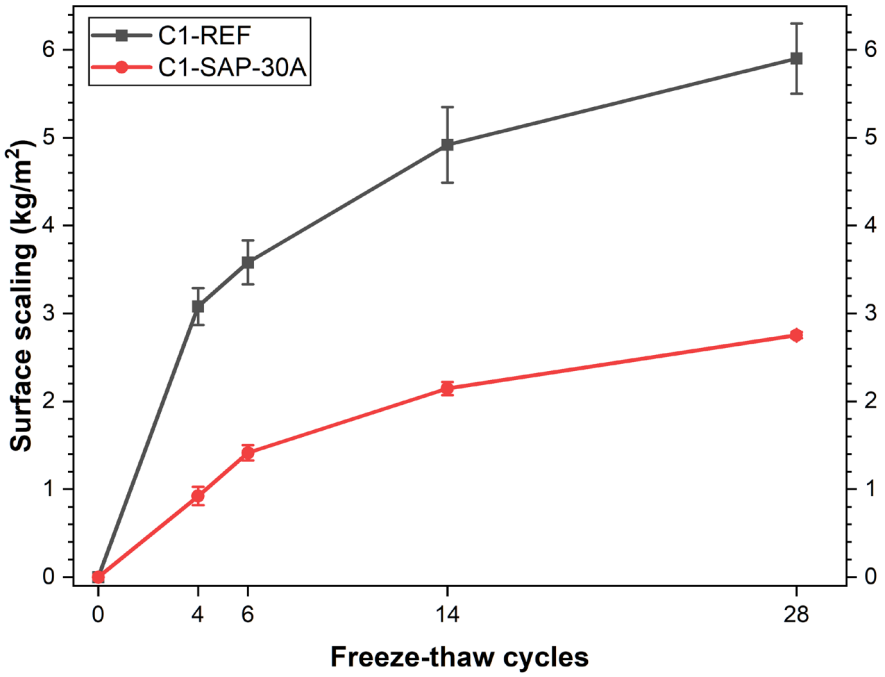

Figure 6.8.1 Surface scaling of C1-REF and C1-SAP-30A

For concrete mix-2, the concrete without adding SAP showed a moderately lower scaling compared to concrete mix-1. The final cumulative surface scaling is around 4 kg/m^2. Considering that concrete mix-1 and concrete mix-2 have the same strength grade, this lower surface scaling might be attributed to the internal curing provided by the recycled aggregates in the mix proportions of concrete mix-1 [151-153]. Improvement in surface scaling resistance was also found when the SAP was added to the concrete mix-2. However, compared to the finding in concrete mix-1, the extent of increment is considerably lower. With the same SAP dosage, C2-SAP-30A only reduced approximately 16% of the final cumulative surface scaling. C2-SAP-45A has a higher SAP dosage of 0.45% BWOS and showed a higher reduction of 31%.

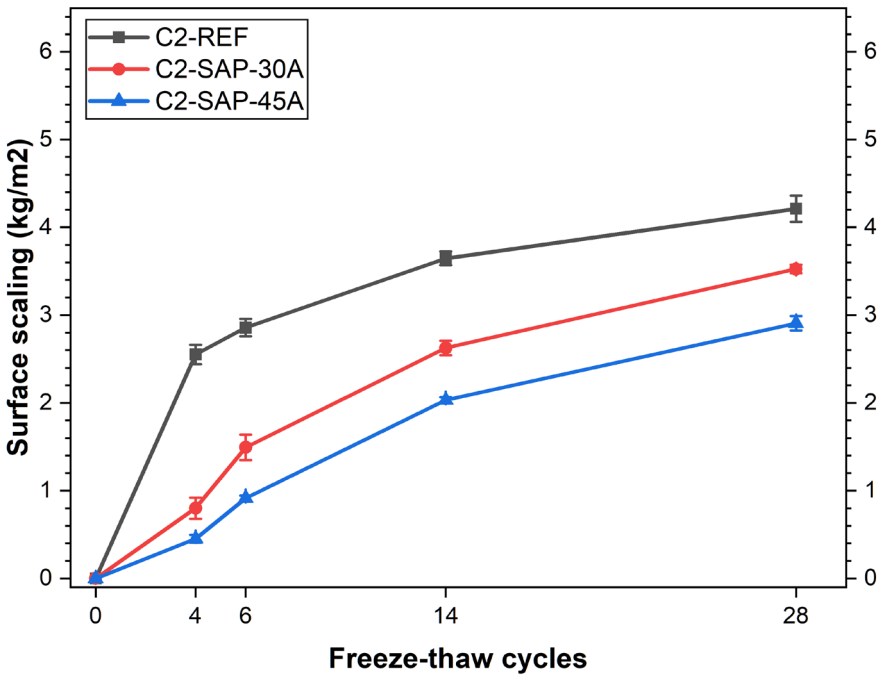

Figure 6.8.2 Surface scaling of C2-REF, C2-SAP-30A and C2-SAP-45A

The lower extent of improvement in concrete mix-2 might be simply caused by the difference in mix proportions. However, there might also be some other causes. These possible causes might be the difference in the preparation and preconditioning of specimens and the recycled aggregates in concrete mix-2. The concrete mix-2 had a shorter curing time (7 days vs. 14 days) and a longer subsequent surface drying (21 days vs. 14 days) than concrete mix-1. Therefore, the influence of drying is more significant in concrete mix-2. However, as discussed in chapter 5 and the literature [96, 147], the effect of SAP on reducing the drying shrinkage and resultant surface cracking is considerably smaller than the effect on reducing autogenous shrinkage. Also, as discussed in chapter 4, the effect of internal curing by SAP is less significant when the drying starts at 7 days. Meanwhile, as mentioned above, recycled aggregates also provide internal curing [151-153]. For these reasons, the effect of internal curing provided by SAP was less significant, and the resultant improvement in concrete mix-2 was limited. Nevertheless, a further improvement was found when the SAP dosage was increased from 0.30% to 0.45%. This observation confirmed the contribution of SAP in reducing surface scaling.

To summarize, the test on the concrete scale showed that SAP improved the surface scaling resistance of AAS concrete and confirmed the finding in the mortar scale. However, when the curing time is shorter, or other internal curing agents are present (e.g., recycle aggregates), the effect of SAP seems to be reduced.

6.9 Observations and conclusions

In this chapter, the freeze-thaw resistance of AASM was studied in the form of surface scaling damage. The effect of applying SAP and AEA on surface scaling resistance and the influence of related factors were studied. The following observations and conclusions can be drawn:

- Plain AASM (i.e., REF) showed poor surface scaling resistance. The total cumulative surface scaling reached around 6 kg/m^2 at the end of the test. This poor performance is mainly attributed to surface microcracking. With the highly developed pre-existing flaws, the

destructive force during freeze-thaw cycles does not need to overcome the matrix tensile strength and can immediately cause surface scaling.

- The addition of SAP considerably improved the surface scaling resistance of AASM by entraining air voids and improving the surface integrity. The extent of improvement was generally more significant with a higher dosage, a lower equivalent water/binder ratio, and finer SAP particles. The saturation status of SAP particles during mixing seemed to have minimal influence.
- The test results of AEA mixtures showed a considerably higher deviation. As a result, it is difficult to draw a solid conclusion on the influence of AEA dosage. Nevertheless, only a moderate extent of improvement was found with the application of AEA, even though the air-void system created by AEA seemed to be good. Compared to SAP mixtures' performance, AEA mixtures' emphasized the significance of surface microcracking in the resultant surface scaling resistance.
- Based on the SAP mixtures, a relatively good correlation was found between the air-void system parameters and the resultant surface scaling resistance. The surface scaling resistance is higher with higher air content, lower flow distance, and a higher specific area.
- Based on the SAP mixtures, a preliminary logarithm model is proposed for bridging the reduction in surface scaling of AASM with the equivalent water/binder ratio, air content, air voids size distribution, and flow distance d_{50}. Although the model is relatively immature and the data points are limited, a good correlation was found between the calculated resistance R and the reduction of final cumulative scaling.
- In the upscaling test, adding SAP also improved the surface scaling resistance of the upscaled AASCs. Depending on the mix design, the extent of improvement ranged from 15% to 50%.

7 Conclusions and recommendations

In this chapter, the main conclusions of this master thesis are summarized. Based on the findings and observations in the study, recommendations are given for future application and further study. The conclusions are related to the following aspects:

- The influence of SAP and AEA on the macro-scale general properties of AASM
- The air-void system created by SAP and AEA
- The influence of SAP and AEA on the surface microstructure of AASM
- The influence of SAP and AEA on the freeze-thaw resistance of AAS, in the form of surface scaling

Subsequently, recommendations are made from the perspective of industrial application and future research.

7.1 Main conclusions

7.1.1 Marco-scale general properties

- In terms of workability, adding SAP with 20g/g additional activator and adding AEA have a minor influence on the workability. On the other hand, adding SAP without the additional activator results in a considerable loss in workability.
- Regarding the air content in the fresh AASM, the sodium α-olefine sulfonate (AOS) based AEA successfully and efficiently entrain extra air in the AASM. The entrained air content increased with increasing AEA dosage until it reached a plateau of around 20% after a certain dosage.
- For the compressive strength, adding AEA resulted in a considerable strength loss in AASM. The reduction increases with increasing dosage. For an air content lower than 10%, the reduction was at a rate of f around 5% reduction in compressive strength for each 1% increment in air content, which is similar to that observed in OPC.
- Depending on the mix design, the reduction in compressive strength caused by adding SAP ranged from 0% to 20%, which is much smaller than adding AEA. Compared to the REF and AEA mixtures, a noticeable higher strength development from 7 days to 28 days is also found in SAP mixtures. These advantages are attributed to the internal curing provided by SAP particles.
- For the flexural strength, the addition of SAP or AEA led to a minor extent of reduction.

7.1.2 Air-void system

- The addition of SAP and AEA successfully created evenly distributed but quite different air voids in the AASM. The air voids created by AEA are tiny, spherical, and densely distributed. The air voids created by SAP are large, irregular, and relatively loosely distributed.

- With similar entrained air content, the amount of air voids created by AEA is approximately ten times higher than by SAP. Due to the high amount of entrained air voids, the flow distance of the AASM significantly decreased by adding SAP/AEA.
- With the same SAP dosage, finer SAP particles lead to finer air voids, more air voids, and smaller flow distance.
- Different SAP absorption compensation methods lead to different SAP absorption environments and slightly influence the resultant air-void system. Compared to dry mixing, prewetting the SAP in the activator leads to slightly higher air content and larger air voids.

7.1.3 Surface microstructure

- Due to the high shrinkage, the AASM exhibited a considerably high surface microcracking potential under internal restraint by aggregates and shrinkage gradient.
- Sealing the AASM for 28 days results in a dense surface microstructure. However, a moderate extent of surface microcracking can be observed due to autogenous shrinkage.
- Following the preconditioning procedure described in the CDF test and the ASTM C672 and exposing the AAS after 7/14 days results in a much more porous microstructure due to drying. And significant surface microcracking is found due to autogenous shrinkage and drying shrinkage.
- Comparison between the sealed samples and dried samples indicates that the microstructure of the outer part of AAS can be considerably different from the internal bulk body because of the sensitivity to the external environment. Samples taken from the inner bulk body might not represent the microstructure at the surface.
- With the addition of SAP, the microcracking caused by the autogenous shrinkage on the sealed specimen's surface was minimized by the effect of internal curing. SAP also shows an effect on reducing the microcracking caused by drying. However, the effect is relatively limited compared to the reduction in autogenous shrinkage microcracking. In terms of the addition of AEA, not much reduction of surface cracking can be found.
- A very similar pore structure is recognized among the samples dried on day 7, while a denser pore structure was found in the SAP mixture among the samples dried on day 14. This observation indicates that: the effect of SAP internal curing is less pronounced if the curing time is relatively short.

7.1.4 Freeze-thaw resistance

- Plain AASM (REF) showed poor surface scaling resistance, which is mainly attributed to the pre-existing surface microcracking due to autogenous shrinkage and drying shrinkage.
- As revealed above, the surface drying procedure in the existing surface scaling test protocols induces significant surface microcracking. However, surface microcracking might be limited and avoided with a more suitable sample preparation and preconditioning procedure. Therefore, following the current sample preparation and preconditioning procedure might unnecessarily underestimate the surface scaling resistance of AAS.
- The addition of SAP considerably improved the surface scaling resistance of AASM by entraining air voids and improving the surface integrity. The extent of improvement was generally more significant with a higher dosage, a lower equivalent water/binder ratio, and

finer SAP particles. The saturation status of SAP particles during mixing seemed to have minimal influence.

- With the minimal effect of improving surface integrity, although adding AEA results in a satisfactory air-void system, only a moderate improvement in surface scaling resistance is found. The comparison of the air-void system and surface scaling resistance between AEA mixtures and SAP mixtures again indicates the significance of surface condition to the surface scaling resistance.
- In the SAP mixtures, a good correlation was found between the air-void system and the resultant surface scaling resistance: the final cumulative surface scaling decreases with higher entrained air content, lower flow distance, and higher specific area.
- Based on the SAP mixtures, a preliminary logarithm model is developed between the reduction in surface scaling of AASM and the factors including equivalent water/binder ratio, air content, air voids size distribution, and flow distance d_{50}. Although the model is quite immature and the data are limited, a good correlation was found between the calculated resistance R and the reduction of final cumulative scaling.
- In the upscaling test, adding SAP also improved the surface scaling resistance of the upscaled AASCs. Depending on the mix design, the extent of improvement ranged from 15% to 50%.

7.2 Recommendations

7.2.1 For industrial application

- Based on the available information, the SAP seems to be a better admixture for improving the freeze-thaw resistance of the AAS or AAMs. Compared to the addition of AEA, the addition of SAP have the advantages of:
    + Much lower strength loss
    + Higher freeze-thaw resistance improvement
    + No compatibility issue with raw materials, e.g., fly ash
    + The air-void system can be easily controlled and tailored by the selection of SAP particles
    + Higher quality consistency and easier quality control. The properties are less sensitive to external factors such as mixing, transportation, compaction, labor proficiency, and human error
    + Incidental benefits such as reducing shrinkage

  Therefore, SAP seems to be a better choice without considering the price and workability.
- A combination of adding SAP and AEA might be a promising solution:
    + With SAP, surface microcracking can be controlled to an extent.
    + With AEA, a favorable air-void system can be generated.
    + With the air voids entraining and internal curing of SAP, the dosage of AEA can be reduced, so as the strength loss.
    + Although no workability improvement was observed in the AASM in this study, it is still widely believed that AEA can improve the workability of concrete by the ball-bearing effect. Such an improvement can partially compensate for the workability loss caused by SAP absorption.

  Therefore, a binary admixture system consisting of SAP and AEA might be the answer for improving the freeze-thaw resistance of AAS products. Further investigation can be conducted from this starting point.
- Considering AAS's significantly high cracking potential when subjected to surface drying and the considerable influence of surface microcracking on the resultant surface scaling resistance, it is suggested to prolong the curing time of AAS products and carefully maintain the humidity at the surface.
- Surface scaling resistance is more dependent on the equivalent water/binder ratio. Therefore, to compensate for the workability loss due to the absorption of SAP, using admixtures such as superplasticizers might be a better choice than simply adding more activators.
- With the exact SAP dosage, finer SAP particles can lead to better freeze-thaw resistance.
- Surface microcracking seems to be an intrinsic issue with AAS products. If the surface scaling problem is a concern, directly using plain AASC as the surface of a road or pavement that is directly exposed to de-icing salt and freeze-thaw cycles is not suggested.

7.2.2 For future research

- Conduct systematic studies on the freeze-thaw resistance of AAMs. Studies on this topic are scarce. The influence of factors such as type of precursor, type of activator, silicate modulus, alkaline content, water/binder ratio, paste content, aggregates, admixtures, curing regime, reaction products, and carbonation on the freeze-thaw resistance of AAMs is unclear. Considering the complexity of AAMs, more importantly, it is to bridge the characteristics found in the microstructure to the resultant freeze-thaw resistance.
- Further investigate and compare the contribution of autogenous shrinkage cracks and drying shrinkage cracks to the surface scaling. The microcrack caused by autogenous shrinkage and drying shrinkage is quite different. Cracks caused by autogenous shrinkage are fewer but go deeper, while cracks caused by drying shrinkage are more densely distributed but remain at the very surface. It can be imagined that their contribution to surface scaling is different. This is quite interesting, and it gives valuable information on the priority of limiting which type of cracks. Such a study can be easily done with the Delft Lattice Model with the ready model developed by Çopuroğlu and Schlangen [51].
- Concerning the high surface microcracking potential, it is suggested to further investigate the evolution of surface microstructure and morphology of AAS when exposed to different environments. Afterwards, an investigation into how the microstructure influences durability issues that concern the surface condition, such as surface scaling, carbonation, chloride penetration, etc., can be conducted.
- Proposed an alternative sample curing procedure than following the one in the current surface scaling test protocol. A temporary solution might be following the alternative precondition procedure described in the CDF test protocol. That is, first conduct a proper curing (for instance, seal curing for 28 days), then conduct a 21-day surface drying. The test might be too lengthy, but the surface conditions might be better.
- Considering the sensitivity of AAS to the external environment, it should also be kept in mind that the sample preparation and preconditioning during the lab work should be in line with, or at least similar to, the real construction.
- Recognize the possible considerable difference in microstructure between the surface layer and the bulk body of AAS products, especially after being exposed to drying. Depending on the research purposes, extra attention might also be taken to the sampling position.
- Further investigate the influence of SAP and AEA on the chemical reaction of AAMs, in terms of reaction products, reaction kinetic, compatibility, etc. For example, in this study, it seems that the particle size distribution has an influence on the reaction kinetics of AASM.
- Considering the micro-CT scan machine's price and limited sample size, it is suggested to develop new techniques or methods or numerical models for characterizing the air-void system created by SAP.
- Further develop the surface scaling reduction model. Since SAP is a tailorable industrial product, unlike the air-void system created by AEA, its air-void system is much more controllable and of good reproducibility. Also, the other influence of SAP is not tricky to be quantified, such as the degree of reaction, capillary pore structure, etc. Therefore, a model bridging the improvement in freeze-thaw resistance and the influenced factors, including air-void system, internal curing, and capillary pore structure, might be quite reliable and universal in prediction.

8 References

[1] Duxson, P., et al., *Geopolymer technology: the current state of the art.* Journal of Materials Science, 2007. **42**(9): p. 2917-2933.

[2] Shi, C., D. Roy, and P. Krivenko, *Alkali-Activated Cements and Concretes*. 2006: Taylor & Francis.

[3] Benhelal, E., et al., *Global strategies and potentials to curb CO2 emissions in cement industry.* Journal of cleaner production, 2013. **51**: p. 142-161.

[4] Favier, A., et al., *A sustainable future for the European Cement and Concrete Industry. Technology assessment for full decarbonisation of the industry by 2050*. 2018, ETH Zurich.

[5] Benhelal, E., E. Shamsaei, and M.I. Rashid, *Challenges against CO2 abatement strategies in cement industry: A review.* Journal of Environmental Sciences, 2021. **104**: p. 84-101.

[6] Davidovits, J., *False Values on CO2 Emission for Geopolymer Cement/Concrete published in Scientific Papers.* 2015.

[7] Bijen, J., *Durability of Engineering Structures: Design, Repair and Maintenance*. 2003: Elsevier. 277.

[8] Valenza, J.J. and G.W. Scherer, *A review of salt scaling: I. Phenomenology.* Cement and Concrete Research, 2007. **37**(7): p. 1007-1021.

[9] Wang, R., et al., *Review on the deterioration and approaches to enhance the durability of concrete in the freeze–thaw environment.* Construction and Building Materials, 2022. **321**: p. 126371.

[10] Provis, J.L. and J.S.J.v. Deventer, *Alkali Activated Materials: State-of-the-Art Report, RILEM TC 224-AAM*. 2013: Springer Science & Business Media. 396.

[11] Cyr, M. and R. Pouhet, *The frost resistance of alkali-activated cement-based binders*, in *Handbook of Alkali-Activated Cements, Mortars and Concretes*, F. Pacheco-Torgal, et al., Editors. 2015, Woodhead Publishing: Oxford. p. 293-318.

[12] Matalkah, F. and P. Soroushian, *Freeze thaw and deicer salt scaling resistance of concrete prepared with alkali aluminosilicate cement.* Construction and Building Materials, 2018. **163**: p. 200-213.

[13] Aiken, T.A., et al., *Mechanical and durability properties of alkali-activated fly ash concrete with increasing slag content.* Construction and Building Materials, 2021. **301**: p. 124330.

[14] Copuroglu, O., *The characterisation, improvement and modelling aspects of frost salt scaling of cement-based materials with a high slag content.* 2006.

[15] *NEN Connect - CEN/TR 15177*.

[16] Setzer, M.J., et al., *Test methods of frost resistance of concrete: CIF-Test: Capillary suction, internal damage and freeze thaw test—Reference method and alternative methods A and B.* Materials and Structures, 2004. **37**(10): p. 743-753.

[17] Sun, P., *Fly ash based inorganic polymeric building material*. 2005: Wayne State University.

[18] Sun, P. and H.-C. Wu, *Chemical and freeze–thaw resistance of fly ash-based inorganic mortars.* Fuel, 2013. **111**: p. 740-745.

[19] *NEN Connect - CEN/TS 12390-9*.

[20] Setzer, M.J., G. Fagerlund, and D.J. Janssen, *CDF test — Test method for the freeze-thaw resistance of concrete-tests with sodium chloride solution (CDF): Recommendation.* Materials and Structures, 1996. **29**(9): p. 523-528.

[21] Powers, T.C. and T.L. Brownyard, *Studies of the Physical Properties of Hardened Portland Cement Paste.* ACI Journal Proceedings. **43**(9).

[22] Gruskovnjak, A., et al., *Hydration of alkali-activated slag: comparison with ordinary Portland cement.* Advances in cement research, 2006. **18**(3): p. 119-128.

[23] Taylor, H.F., *Cement chemistry*. Vol. 2. 1997: Thomas Telford London.

[24] Douglas, E., A. Bilodeau, and V.M. Malhotra, *Properties and Durability of Alkali-Activated Slag Concrete.* Materials Journal, 1992. **89**(5): p. 509-516.

[25] Gifford, P.M. and J.E. Gillott, *Freeze-thaw durability of activated blast furnace slag cement concrete.* Materials Journal, 1996. **93**(3): p. 242-245.

[26] Fu, Y., L. Cai, and W. Yonggen, *Freeze–thaw cycle test and damage mechanics models of alkali-activated slag concrete.* Construction and Building Materials, 2011. **25**(7): p. 3144-3148.

[27] Cai, L., H. Wang, and Y. Fu, *Freeze–thaw resistance of alkali–slag concrete based on response surface methodology.* Construction and Building Materials, 2013. **49**: p. 70-76.

[28] Valenza, J.J. and G.W. Scherer, *A review of salt scaling: II. Mechanisms.* Cement and Concrete Research, 2007. **37**(7): p. 1022-1034.

[29] Collins, F. and J. Sanjayan, *Microcracking and strength development of alkali activated slag concrete.* Cement and Concrete Composites, 2001. **23**(4-5): p. 345-352.

[30] J. Marchand, M.P.D.B. and C. Talbot, *Influence of Chloride Solution Concentration on Deicer Salt Scaling Deterioration of Concrete.* ACI Materials Journal, 1999. **96**(4).

[31] Fagerlund, G., *Significance of critical degrees of saturation at freezing of porous and brittle materials*. 1973: Lund Institute of Technology, Division of Building materials.

[32] Fagerlund, G., *The international cooperative test of the critical degree of saturation method of assessing the freeze/thaw resistance of concrete.* Matériaux et Construction, 1977. **10**(4): p. 231-253.

[33] Litvan, G.G. and I.f.R.i. Construction, *The Mechanism of Frost Action in Concrete - Theory and Practical Implications*. 1989: National Research Council Canada, Institute for Research in Construction.

[34] Fagerlund, G., *A service life model for internal frost damage in concrete*. 2004: Univ.

[35] Li, W., et al., *Water Absorption and Critical Degree of Saturation Relating to Freeze-Thaw Damage in Concrete Pavement Joints.* Journal of Materials in Civil Engineering, 2012. **24**(3): p. 299-307.

[36] Smith, S.H., et al., *Service-life of concrete in freeze-thaw environments: Critical degree of saturation and calcium oxychloride formation.* Cement and Concrete Research, 2019. **122**: p. 93-106.

[37] Powers, T.C., *A Working Hypothesis for Further Studies of Frost Resistance of Concrete.* Journal Proceedings, 1945. **41**(1): p. 245-272.

[38] Powers, T.C., *The air requirement of frost-resistant concrete.* 1949.

[39] Powers, T.C., *Structure and Physical Properties of Hardened Portland Cement Paste.* Journal of the American Ceramic Society, 1958. **41**(1): p. 1-6.

[40] Sun, Z. and G.W. Scherer, *Effect of air voids on salt scaling and internal freezing.* Cement and Concrete Research, 2010. **40**(2): p. 260-270.

[41] Penttala, V., *Surface and internal deterioration of concrete due to saline and non-saline freeze–thaw loads.* Cement and Concrete Research, 2006. **36**(5): p. 921-928.

[42] Zeng, Q., *Poromechanical behavior of cement-based materials subjected to freeze-thaw actions with salts: modeling and experiments*. 2011, Université Paris-Est.

[43] Setzer, M.J., *Micro-Ice-Lens Formation in Porous Solid.* Journal of Colloid and Interface Science, 2001. **243**(1): p. 193-201.

[44] Setzer, M.J., *Mechanical Stability Criterion, Triple-Phase Condition, and Pressure Differences of Matter Condensed in a Porous Matrix.* Journal of Colloid and Interface Science, 2001. **235**(1): p. 170-182.

[45] Bouzoubaâ, N., M.H. Zhang, and V.M. Malhotra, *Mechanical properties and durability of concrete made with high-volume fly ash blended cements using a coarse fly ash.* Cement and Concrete Research, 2001. **31**(10): p. 1393-1402.

[46] Snyder, M.J., *Protective Coatings to Prevent Deterioration of Concrete by Deicing Chemicals*. 1965: Highway Research Board of the Division of Engineering and Industrial Research, National Academy of Sciences-National Research Council.

[47] Harnik, A., U. Meier, and A. Rösli, *Combined Influence of Freezing and Deicing Salt on Concrete--Physical Aspects*. 1980: ASTM International.

[48] Rösli, A. and A. Harnik, *Improving the Durability of Concrete to Freezing and Deicing Salts*, in *Durability of Building Materials and Components*. 1980, ASTM International.

[49] Valenza II, J.J. and G.W. Scherer, *Mechanism for Salt Scaling.* Journal of the American Ceramic Society, 2006. **89**(4): p. 1161-1179.

[50] GULATI, S.T. and H.E. HAGY, *Analysis and Measurement of Glue-Spall Stresses in Glass-Epoxy Bonds.* Journal of the American Ceramic Society, 1982. **65**(1): p. 1-5.

[51] Çopuroğlu, O. and E. Schlangen, *Modeling of frost salt scaling.* Cement and Concrete Research, 2008. **38**(1): p. 27-39.

[52] Rose, K., B.B. Hope, and A.K.C. Ip, *Statistical analysis of strength and durability of concrete made with different cements.* Cement and Concrete Research, 1989. **19**(3): p. 476-486.

[53] Skripkiūnas, G., et al., *The Cement Type Effect on Freeze – Thaw and Deicing Salt Resistance of Concrete.* Procedia Engineering, 2013. **57**: p. 1045-1051.

[54] Pigeon, M., et al., *Surface microstructure and scaling resistance of concrete.* Cement and Concrete Research, 1996. **26**(10): p. 1555-1566.

[55] Glukhovsky, V., et al., *Manufacture of concretes and structures from slag alkaline binders.* Budivelnyk Publish, 1988.

[56] Özdal, M., M.B. Karakoç, and A. Özcan, *Investigation of the properties of two different slag-based geopolymer concretes exposed to freeze–thaw cycles.* Structural Concrete, 2021. **22**(S1): p. E332-E340.

[57] Tor Arne, H. and J.S. Erik, *Frost Resistance of High-Strength Concrete.* ACI Symposium Publication, 1990. **121**.

[58] Wang, Z., et al., *Relative humidity and deterioration of concrete under freeze–thaw load.* Construction and Building Materials, 2014. **62**: p. 18-27.

[59] Zhang, K., J. Zhou, and Z. Yin, *Experimental Study on Mechanical Properties and Pore Structure Deterioration of Concrete under Freeze–Thaw Cycles.* Materials, 2021. **14**(21): p. 6568.

[60] Nowak-Michta, A., *Salt Scaling Resistance of Variable w/c Ratio Air-Entrained Concretes Modified with Polycarboxylates as a Proper Consequence of Air Void System.* Materials, 2022. **15**(17): p. 5839.

[61] Lu, Z., et al., *Freeze-thaw resistance of Ultra-High performance concrete: Dependence on concrete composition.* Construction and Building Materials, 2021. **293**: p. 123523.

[62] Delatte, N. and C. Storey, *Effects of Density and Mixture Proportions on Freeze–Thaw Durability of Roller-Compacted Concrete Pavement.* Transportation Research Record, 2005. **1914**(1): p. 45-52.

[63] Li, N., et al., *A mixture proportioning method for the development of performance-based alkali-activated slag-based concrete.* Cement and Concrete Composites, 2018. **93**: p. 163-174.

[64] Shi, C., *Strength, pore structure and permeability of alkali-activated slag mortars.* Cement and Concrete Research, 1996. **26**(12): p. 1789-1799.

[65] Timkovich, V.Y., *Genesis of structure and strength of the slag alkaline cements and concretes*. 1986, PhD Thesis, Kiev Civil Engineering Institute, Kiev, USSR.

[66] Haoming, W., *Effect of different curing regimes on the mechanical property and durability of alkali-activated slag mortar*. 2022.

[67] Talling, B. and P. Krivenko, *5 - Blast furnace slag-the ultimate binder*, in *Waste Materials Used in Concrete Manufacturing*, S. Chandra, Editor. 1996, William Andrew Publishing: Westwood, NJ. p. 235-289.

[68] Byfors, K., et al., *Durability of Concrete Made With Alkali-Activated Slag.* Special Publication, 1989. **114**: p. 1429-1466.

[69] Coppola, L., et al., *The durability of one-part alkali-activated slag-based mortars in different environments.* Sustainability, 2020. **12**(9): p. 3561.

[70] Chen, B. and J. Wang, *Experimental Study on the Durability of Alkali-Activated Slag Concrete after Freeze-Thaw Cycle.* Advances in Materials Science and Engineering, 2021. **2021**: p. 9915639.

[71] Neville, A.M., *Properties of concrete*. Vol. 4. 1995: Longman London.

[72] Collins, F. and J.G. Sanjayan, *Workability and mechanical properties of alkali activated slag concrete.* Cement and concrete research, 1999. **29**(3): p. 455-458.

[73] Chi, M., *Effects of dosage of alkali-activated solution and curing conditions on the properties and durability of alkali-activated slag concrete.* Construction and Building Materials, 2012. **35**: p. 240-245.

[74] El-Hassan, H., E. Shehab, and A. Al-Sallamin, *Influence of different curing regimes on the performance and microstructure of alkali-activated slag concrete.* Journal of Materials in Civil Engineering, 2018. **30**(9): p. 04018230.

[75] Dong, M., M. Elchalakani, and A. Karrech, *Curing conditions of alkali-activated fly ash and slag mortar.* Journal of Materials in Civil Engineering, 2020. **32**(6): p. 04020122.

[76] Çopuro, O., *Effect of curing conditions on freeze-thaw de-icing salt resistance of blast furnace slag cement mortars.* High Performance Structures and Materials II, 2004: p. 9.

[77] Liu, C., et al., *Degradation of alkali-activated slag subjected to water immersion.* Cement and Concrete Composites, (in progress, minor revision).

[78] Palacios, M. and F. Puertas, *Effect of carbonation on alkali‐activated slag paste.* Journal of the American Ceramic Society, 2006. **89**(10): p. 3211-3221.

[79] Puertas, F., M. Palacios, and T. Vázquez, *Carbonation process of alkali-activated slag mortars.* Journal of materials science, 2006. **41**(10): p. 3071-3082.

[80] Shi, Z., et al., *Effect of alkali dosage and silicate modulus on carbonation of alkali-activated slag mortars.* Cement and Concrete Research, 2018. **113**: p. 55-64.

[81] Verbeck, G.J. and P. Klieger, *Studies of'salt'scaling of concrete.* Highway Research Board Bulletin, 1957(150).

[82] Powers, T.C. and R.A. Helmuth, *THEORY OF VOLUME CHANGES IN HARDENED PORTLAND-CEMENT PASTE DURING FREEZING.* Highway Research Board Proceedings, 1953. **32**.

[83] Corr, D.J., et al., *Investigating entrained air voids and Portland cement hydration with low-temperature scanning electron microscopy.* Cement and Concrete Composites, 2004. **26**(8): p. 1007-1012.

[84] Tunstall, L.E., M.T. Ley, and G.W. Scherer, *Air entraining admixtures: Mechanisms, evaluations, and interactions.* Cement and Concrete Research, 2021. **150**: p. 106557.

[85] Coussy, O., *Mechanics and physics of porous solids*. 2011: John Wiley & Sons.

[86] Scherer, G.W., *Freezing gels.* Journal of Non-Crystalline Solids, 1993. **155**(1): p. 1-25.

[87] Rosen, M.J. and J.T. Kunjappu, *Surfactants and interfacial phenomena*. 2012: John Wiley & Sons.

[88] ZOHOURIAN, M.M. and K. Kabiri, *Superabsorbent polymer materials: a review.* 2008.

[89] Kang, S.-H., S.-G. Hong, and J. Moon, *Absorption kinetics of superabsorbent polymers (SAP) in various cement-based solutions.* Cement and Concrete Research, 2017. **97**: p. 73-83.

[90] Mechtcherine, V., et al., *Recommendations of RILEM TC 260-RSC for using superabsorbent polymers (SAP) for improving freeze–thaw resistance of cement-based materials.* Materials and Structures, 2019. **52**(4): p. 75.

[91] Li, Z., et al., *Internal curing by superabsorbent polymers in alkali-activated slag.* Cement and Concrete Research, 2020. **135**: p. 106123.

[92] Mechtcherine, V., E. Secrieru, and C. Schröfl, *Effect of superabsorbent polymers (SAPs) on rheological properties of fresh cement-based mortars — Development of yield stress and plastic viscosity over time.* Cement and Concrete Research, 2015. **67**: p. 52-65.

[93] Wyrzykowski, M., et al., *Recommendation of RILEM TC 260-RSC: using superabsorbent polymers (SAP) to mitigate autogenous shrinkage.* Materials and Structures, 2018. **51**(5): p. 135.

[94] Snoeck, D. and N.D. Belie, *Repeated Autogenous Healing in Strain-Hardening Cementitious Composites by Using Superabsorbent Polymers.* Journal of Materials in Civil Engineering, 2016. **28**(1): p. 04015086.

[95] Riyazi, S., J.T. Kevern, and M. Mulheron, *Super absorbent polymers (SAPs) as physical air entrainment in cement mortars.* Construction and Building Materials, 2017. **147**: p. 669-676.

[96] Mechtcherine, V., et al., *Application of super absorbent polymers (SAP) in concrete construction—update of RILEM state-of-the-art report.* Materials and Structures, 2021. **54**(2): p. 80.

[97] Hasholt, M.T., O.M. Jensen, and S. Laustsen, *Superabsorbent polymers as a means of improving frost resistance of concrete.* Adv. Civ. Eng. Mat, 2015. **1**: p. 237-256.

[98] Kusayama, S., H. Kuwabara, and S.-i. Igarashi, *COMPARISON OF SALT SCALING RESISTANCE OF CONCRETES WITH DIFFERENT TYPES OF SUPERABSORBENT POLYMERS.* 2014: p. 11.

[99] Laustsen, S., M.T. Hasholt, and O.M. Jensen, *Void structure of concrete with superabsorbent polymers and its relation to frost resistance of concrete.* Materials and Structures, 2015. **48**(1): p. 357-368.

[100] Mechtcherine, V., et al., *Effect of superabsorbent polymers (SAP) on the freeze–thaw resistance of concrete: results of a RILEM interlaboratory study.* Materials and Structures, 2016. **50**(1): p. 14.

[101] Yang, Z., et al., *Effect of superabsorbent polymer introduction on properties of alkali-activated slag mortar.* Construction and Building Materials, 2022. **340**: p. 127541.

[102] Shah, H.A., Q. Yuan, and S. Zuo, *Air entrainment in fresh concrete and its effects on hardened concrete-a review.* Construction and Building Materials, 2021. **274**: p. 121835.

[103] Aïtcin, P.C., *6 - Entrained air in concrete: Rheology and freezing resistance*, in *Science and Technology of Concrete Admixtures*, P.-C. Aïtcin and R.J. Flatt, Editors. 2016, Woodhead Publishing. p. 87-95.

[104] Gifford, P.M.P.M., *Alkali-aggregate reaction and freeze-thaw durability of activated blast furnace slag cement concrete*. 1995: University of Calgary.

[105] Bakharev, T., J.G. Sanjayan, and Y.B. Cheng, *Effect of admixtures on properties of alkali-activated slag concrete.* Cement and Concrete Research, 2000. **30**(9): p. 1367-1374.

[106] Sikora, K.S. and A.J. Klemm, *Effect of superabsorbent polymers on workability and hydration process in fly ash cementitious composites.* Journal of Materials in Civil Engineering, 2015. **27**(5): p. 04014170.

[107] Snoeck, D., et al., *Effect of high amounts of superabsorbent polymers and additional water on the workability, microstructure and strength of mortars with a water-to-cement ratio of 0.50.* Construction and Building Materials, 2014. **72**: p. 148-157.

[108] Filho, R.D.T., et al., *Effect of Superabsorbent Polymers on the Workability of Concrete and Mortar*, in *Application of Super Absorbent Polymers (SAP) in Concrete Construction: State-of-the-Art Report Prepared by Technical Committee 225-SAP*, V. Mechtcherine and H.-W. Reinhardt, Editors. 2012, Springer Netherlands: Dordrecht. p. 39-50.

[109] ACI Committee 212, C.A., *Report on Chemical Admixtures for Concrete: ACI 212.3R-10*. 2011: American Concrete Institute.

[110] Rodriguez, C.R., et al. *X-ray micro tomography of water absorption by superabsorbent polymers in mortar*. in *International Conference on Application of Superabsorbent Polymers & Other New Admixtures Towards Smart Concrete*. 2019. Springer.

[111] Snoeck, D., C. Schröfl, and V. Mechtcherine, *Recommendation of RILEM TC 260-RSC: testing sorption by superabsorbent polymers (SAP) prior to implementation in cement-based materials.* Materials and Structures, 2018. **51**(5): p. 116.

[112] Bílek Jr, V., et al. *Influence of Chemical Admixtures on Properties of Alkali-Activated Slag-Based Mortars*. in *Advanced Materials Research*. 2015. Trans Tech Publ.

[113] Łaźniewska-Piekarczyk, B., *The influence of chemical admixtures on cement hydration and mixture properties of very high performance self-compacting concrete.* Construction and Building Materials, 2013. **49**: p. 643-662.

[114] Silva, B., et al., *Effect of Air-entraining and Water-repellent Admixtures and of Their Dosage on the Performance of Lime Mortars.* International Journal of Architectural Heritage, 2022. **16**(4): p. 630-644.

[115] Mendes, J.C., et al., *Mechanical, rheological and morphological analysis of cement-based composites with a new LAS-based air entraining agent.* Construction and Building Materials, 2017. **145**: p. 648-661.

[116] Topcu, I.B., *Effect of high dosage air-entraining admixture usage on micro concrete properties.* European Journal of Engineering and Natural Sciences, 2017. **2**(1): p. 1-11.

[117] Struble, L.J. and Q. Jiang, *Effects of air entrainment on rheology.* Materials Journal, 2004. **101**(6): p. 448-456.

[118] Ouyang, X., Y. Guo, and X. Qiu, *The feasibility of synthetic surfactant as an air entraining agent for the cement matrix.* Construction and Building Materials, 2008. **22**(8): p. 1774-1779.

[119] Anderson, J.L., et al., *Surfactant solvation effects and micelle formation in ionic liquids.* Chemical Communications, 2003(19): p. 2444-2445.

[120] Du, L. and K.J. Folliard, *Mechanisms of air entrainment in concrete.* Cement and Concrete Research, 2005. **35**(8): p. 1463-1471.

[121] Flatt, R. and I. Schober, *7 - Superplasticizers and the rheology of concrete*, in *Understanding the Rheology of Concrete*, N. Roussel, Editor. 2012, Woodhead Publishing. p. 144-208.

[122] Assmann, A., *Physical properties of concrete modified with superabsorbent polymers.* 2013.

[123] Hounsfield, G.N., *Computerized transverse axial scanning (tomography): Part 1. Description of system.* The British journal of radiology, 1973. **46**(552): p. 1016-1022.

[124] Ritman, E.L., *Current status of developments and applications of micro-CT.* Annual review of biomedical engineering, 2011. **13**: p. 531-552.

[125] Yuan, J., Y. Wu, and J. Zhang, *Characterization of air voids and frost resistance of concrete based on industrial computerized tomographical technology.* Construction and Building Materials, 2018. **168**: p. 975-983.

[126] Vásárhelyi, L., et al., *Microcomputed tomography–based characterization of advanced materials: a review.* Materials Today Advances, 2020. **8**: p. 100084.

[127] Flannery, B.P., et al., *Three-dimensional X-ray microtomography.* Science, 1987. **237**(4821): p. 1439-1444.

[128] *What is Micro-CT? An Introduction*. [cited 2023 1/12]; Available from: https://www.microphotonics.com/what-is-micro-ct-an-introduction/.

[129] Myers, D., *Surfaces, interfaces, and colloids*. Vol. 415. 1999: Wiley New York.

[130] Collins, F. and J.G. Sanjayan, *Effect of pore size distribution on drying shrinking of alkali-activated slag concrete.* Cement and Concrete Research, 2000. **30**(9): p. 1401-1406.

[131] Tatar, J., et al., *Characterization of adhesive interphase between epoxy and cement paste via Raman spectroscopy and mercury intrusion porosimetry.* Cement and Concrete Composites, 2018. **88**: p. 187-199.

[132] Whiting, D. and D.E. Kline, *Pore size distribution in epoxy impregnated hardened cement pastes.* Cement and Concrete Research, 1977. **7**(1): p. 53-60.

[133] *NEN Connect - CEN/TS 12390-16*.

[134] Li, Z., et al., *Mechanisms of autogenous shrinkage of alkali-activated slag and fly ash pastes.* Cement and Concrete Research, 2020. **135**: p. 106107.

[135] Scherer, G.W., *Theory of drying.* Journal of the American Ceramic Society, 1990. **73**(1): p. 3-14.

[136] Ballekere Kumarappa, D., S. Peethamparan, and M. Ngami, *Autogenous shrinkage of alkali activated slag mortars: Basic mechanisms and mitigation methods.* Cement and Concrete Research, 2018. **109**: p. 1-9.

[137] Chen, W., et al., *Effects of alkali dosage and silicate modulus on autogenous shrinkage of alkali-activated slag cement paste.* Cement and Concrete Research, 2021. **141**: p. 106322.

[138] Cartwright, C., F. Rajabipour, and A. Radlińska, *Shrinkage characteristics of alkali-activated slag cements.* Journal of materials in civil engineering, 2015. **27**(7): p. B4014007.

[139] Lee, N.K., J.G. Jang, and H.K. Lee, *Shrinkage characteristics of alkali-activated fly ash/slag paste and mortar at early ages.* Cement and Concrete Composites, 2014. **53**: p. 239-248.

[140] Ye, H. and A. Radlińska, *Shrinkage mechanisms of alkali-activated slag.* Cement and Concrete Research, 2016. **88**: p. 126-135.

[141] Li, Z., et al., *Prediction of the autogenous shrinkage and microcracking of alkali-activated slag and fly ash concrete.* Cement and Concrete Composites, 2021. **117**: p. 103913.

[142] Pickett, G. *Effect of aggregate on shrinkage of concrete and a hypothesis concerning shrinkage*. in *Journal Proceedings*. 1956.

[143] Li, Z., et al., *Internal curing of alkali-activated slag-fly ash paste with superabsorbent polymers.* Construction and Building Materials, 2020. **263**: p. 120985.

[144] Shen, D., et al., *Effect of internal curing with super absorbent polymers on the relative humidity of early-age concrete.* Construction and Building Materials, 2015. **99**: p. 246-253.

[145] Nedeljković, M., Z. Li, and G. Ye, *Setting, Strength, and Autogenous Shrinkage of Alkali-Activated Fly Ash and Slag Pastes: Effect of Slag Content.* Materials, 2018. **11**(11): p. 2121.

[146] Yang, J., et al., *Research on drying shrinkage deformation and cracking risk of pavement concrete internally cured by SAPs.* Construction and Building Materials, 2019. **227**: p. 116705.

[147] Assmann, A. and H. Reinhardt, *Tensile creep and shrinkage of SAP modified concrete.* Cement and Concrete Research, 2014. **58**: p. 179-185.

[148] Setzer, M.J. and R. Auberg, *Freeze-thaw and deicing salt resistance of concrete testing by the CDF method CDF resistance limit and evaluation of precision.* Materials and Structures, 1995. **28**(1): p. 16-31.

[149] Wehbe, Y. and A. Ghahremaninezhad, *Combined effect of shrinkage reducing admixtures (SRA) and superabsorbent polymers (SAP) on the autogenous shrinkage, hydration and properties of cementitious materials.* Construction and Building Materials, 2017. **138**: p. 151-162.

[150] Krafcik, M.J., N.D. Macke, and K.A. Erk, *Improved concrete materials with hydrogel-based internal curing agents.* Gels, 2017. **3**(4): p. 46.

[151] El-Hawary, M. and A. Al-Sulily, *Internal curing of recycled aggregates concrete.* Journal of Cleaner Production, 2020. **275**: p. 122911.

[152] Lee, N.K., S.Y. Abate, and H.-K. Kim, *Use of recycled aggregates as internal curing agent for alkali-activated slag system.* Construction and Building Materials, 2018. **159**: p. 286-296.

[153] Li, Z., et al., *Internal curing effect of saturated recycled fine aggregates in early-age mortar.* Cement and Concrete Composites, 2020. **108**: p. 103444.